Dissertation
submitted to the
Combined Faculties for the Natural Sciences and for Mathematics
of the Ruperto-Carola University of Heidelberg, Germany

for the degree of
Doctor of Natural Sciences

presented by
Dipl.-Phys. **Udo Eisenbarth**
born in Koblenz

Oral examination: 21th November 2001

# Laser cooling of fast stored ion beams to extreme phase-space densities

Referees:
Priv.-Doz. Dr. Matthias Weidemüller
Priv.-Doz. Dr. Wolfgang Quint

**Zusammenfassung:**
Die vorliegende Dissertation präsentiert Experimente zur effizienten Laserkühlung hochenergetischer $^{9}Be^{+}$-Ionenstrahlen hin zu extremen Phasenraumdichten. Anhand systematischer Messungen und realistischen Computermodellen wurde die Dynamik des gebunchten Kühlschemas in verschiedenen Potentialformen untersucht sowie bedeutende Rolle strahlinterner Coulombstöße erkannt. Bei extrem hohen Phasenraumdichten beobachtet man ein plötzliches Verschwinden strahlinterne Stöße, die auf das Einsetzen von Ordnungsprozessen hindeuten könnten. Desweiteren wird Laserkühlung ungebunchter Ionenstrahlen in einer optischen Melasse demonstriert. In diesem Zusammenhang wurde erstmalig die dreidimensionale Kühlung kontinuierlicher Ionenstrahlen realisiert.

**Abstract:**
This doctoral thesis presents experiments on efficient laser cooling of fast stored $^{9}Be^{+}$ ions to extreme phase-space densities. The dynamics of bunched cooling in different potentials and the important role of intra beam Coulomb scattering have been investigated on the basis of systematic measurements and realistic computer models. At extreme phase-space densities an abrupt disappearance of intra beam scattering is observed which could possibly indicate the onset of Coulomb ordering in the ion beam. Laser cooling of a coasting beam in an optical molasses is demonstrated. For the first time, true 3D laser cooling of a coasting beam has been realized.

# Contents

# Chapter 1

# Introduction

Over the years, the physics with fast stored ion beams has evolved into a large research field with many dedicated accelerator and storage facilities around the world. With the advance of cooling techniques [Møller, 1994] such as electron cooling and stochastic cooling a new class of high-precision experiments became possible. Cold ion beams in a storage ring can be used to perform high-precision mass measurements (Schottky mass spectrometry) [Radon et al., 1997], investigations of short-living isotopes cooled and stored in traps [Bollen et al., 1996] and precise tests of special relativity [Grieser et al., 1994]. By recombination experiments, atomic structures [Wolf et al., 2000] and QED effects[Brandau et al., 1999] are investigated. Cold ion beams could also become an important tool in inertial fusion reactions [Bock, 1997]. The study of the dynamics of stored cold ion beams itself delivers important results on the physics of non-neutral cold plasmas at high center of mass energies [Miesner, 1995, Lauer, 1999, Madsen et al., 1999].

All cooling methods used at storage rings have to fight against extremely strong heating processes. This heating essentially stems from *envelope oscillations* due to the alternating focusing of the beam along the ring in connection to *intra beam Coulomb scattering* (IBS) [Sørensen, 1987]. Figure 1.1 shows the coupling of the degrees of freedom for ions in a storage ring. The energy for IBS heating comes from the kinetic beam energy which represents a huge heat bath. Since the collision rate depends on the phase-space density, this heating mechanism becomes even stronger during the cooling process finally limiting the achievable temperatures.

Laser cooling is a technique to achieve much higher cooling rates It is particularly suited for low-charged ions where electron cooling becomes rather inefficient. Laser cooling relies on the radiation-pressure force exerted by resonance laser light on the ions. The light force arises from repeated momentum transfer in a series of many absorption-spontaneous emission cycles

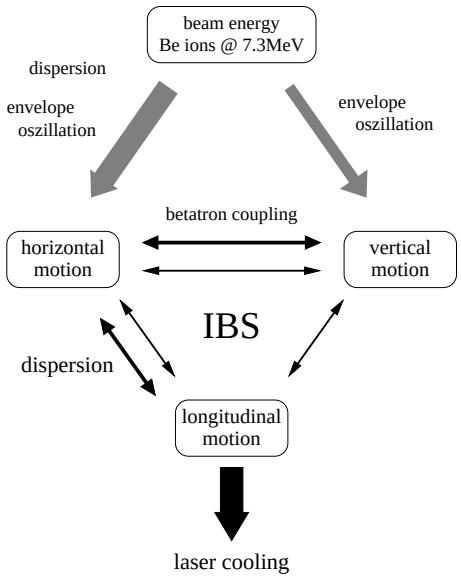


**Figure 1.1:** *Couplings between the degrees of freedom for an ion beam at a high center of mass energy.*

[Metcalf and van der Straten, 1999]. For moving ions the Doppler effect translates this frequency dependency force into velocity-dependent friction force. At a storage ring laser cooling can be realized by merging a laser beam with the ion beam along a straight section of the storage ring (figure 1.2). One the one hand

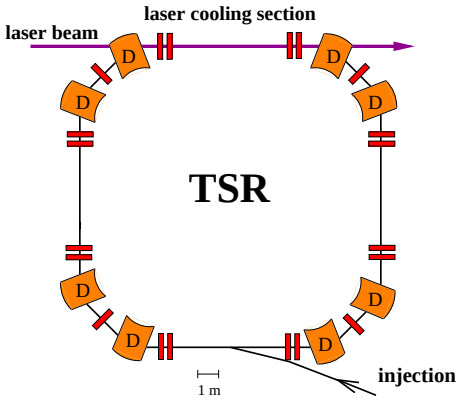


**Figure 1.2:** *Implementation of laser cooling at the Heidelberg Test Storage Ring (TSR). For laser cooling the ion beam is merged with a laser beam whose frequency is nearly resonant with a Doppler-shifted transition line of the ions.*

laser cooling is restricted to some light ions such as $Li^+$, $Be^+$ or $Mg^+$ having

an optical transition with a wavelength accessible to a laser system. However it turned out that laser cooling is an extremely efficient cooling process leading to phase-space densities that cannot be achieved with other cooling techniques at a storage ring. Laser cooling experiments have been performed with Lithium and Beryllium ions at TSR [Schröder et al., 1990] at beam energies of MeV and with Magnesium ions at 100 keV in the ASTRID storage ring [Hangst et al., 1991].

Since the laser force only either accelerates or decelerates the ions, beam cooling can only be realized by providing an additional counterforce. In early laser cooling experiments this counterforce was either realized using a second counterpropagating laser [Schröder et al., 1990] or an induction accelerator (INDAC) [Ellert et al., 1992, Petrich et al., 1993]. These experiments revealed the important role of hard Coulomb collisions leading to ion velocity changes of about 1000 m/s. The collisions lead to losses for the cooling process due the small capture range of the laser force ($\approx 150$ m/s). These losses could be suppressed by the use of a capture range extension realized through a rapid adiabatic passage [Wanner et al., 1998]. With the introduction of beam bunching to realize the counterforce by the application of a pseudopotential confining the ions in the longitudinal direction it was possible to overcome the time limitation of the INDAC method [Hangst et al., 1995b, Miesner et al., 1996a]. Bunched cooling also leads to a "recycling" of ions that have undergone a Coulomb collision out of the capture range.

Laser cooling can directly cool only the longitudinal degree of freedom. Direct transverse laser cooling by shining in light perpendicular to the direction of motion is practically not possible. The reasons are the short interaction times and the sensitivity to tiny angle deviations between laser and ion beam leading to large Doppler shifts. However, methods have been developed to also cool the beam transversally: since the degrees of freedom are coupled through collisions, the directly cooled longitudinal direction acts as a heat sink which also leads to a temperature reduction of the transverse directions (*indirect cooling*) [Miesner et al., 1996b]. In addition the *ring dispersion* leads to a coupling between the horizontal position of the closed orbit and the longitudinal ion momentum (figure 1.1. Combining dispersive coupling with linear betatron coupling [Bryant, 1994] we realized full 3D laser cooling which does not depend on the phase-space density [Lauer et al., 1998].

In the framework of this thesis, systematic measurements on laser cooling of bunched beams in various potential shapes have been performed. These experiments give a very clear picture of the short- and the long-term dynamics of the cooling process. Realistic computer simulations have been developed to identify kinetic effects of the ion ensemble experiencing non-linear cooling forces and the influence of different bunching potentials on the cooling dynamics. Furthermore the implementation of collisions into the model gives a detailed insight on the

crucial role of intra beam scattering for the laser cooling dynamics.

With these experiments the cooling parameters have been optimized to achieve efficient 3D cooling to unprecendented phase-space densities in storage rings. In this extreme regime we observed a sudden anomalous beam behavior which shows the signature of *Coulomb ordering*: at very high phase-space densities the mutual Coulomb repulsion of the ions significantly influences the behavior of the beam. In particular, if the thermal energy becomes comparable to the Coulomb energy which is expressed by the *plasma parameter* $\Gamma = E_{\mathrm{Coulomb}}/E_{\mathrm{therm}} \simeq 1$, ions can no longer overtake each other. For $\Gamma > 127$ the formation of these *Wigner crystals* has already been observed and studied in various ion traps for ensembles at rest [Walther, 1993]. For low kinetic energies of about 1 eV recent experiments demonstrated the formation of a laser-cooled crystallized ion beam revolving in a small circular quadrupole trap (PALLAS) [Schätz et al., 2001]. The question of a possible Coulomb ordering in an ion beam revolving with some percent of the speed of light is one motivation for our cooling experiments [Habs and Grimm, 1995]. A crystalline ion beam represents the ultimate phase-space density reachable at a storage ring. Ordering phenomena at beam energies of several hundred MeV have been observed for electron-cooled beams of highly charged ions [Steck et al., 1996]. In this case the experiments have been performed with an extremely small number of ions. Typical ion distances are on the order of several centimeters up to meters. Coulomb ordering takes place in the sense that two revolving ions do not overtake each other, but they are reflected due to the electrostatic repulsion [Hasse, 1999]. However, due to the large distances one does not achieve crystalline structures with a long-range order.

Theoretical calculations [Hasse and Schiffer, 1990] show that the structure of a crystallized ion beam strongly depends on the ion number. The lowest crystalline structure is the one-dimensional linear chain where ion are moving along the closed orbit with well-defined distances from each other. For higher beam densities the ions start evading from each other forming a two-dimensional zig-zag arrangement or higher 3D structures. Molecular dynamics simulations done for our experimental conditions ($^9Be^+$ ions at 7.3 MeV in the Heidelberg test storage ring TSR) predict that only the linear chain and possibly the vertical zig-zag are stably storagable [Wei et al., 1995]. Higher order 3D structures would be destroyed due to shear force occurring in the bending magnets of the storage ring. The maximum total ion number for the formation of a linear ion chain at the TSR according to the simulation would be $10^6$.

Our experiments indeed show a sudden disappearance of intra beam scattering during the cooling process at the predicted particle number. This would be the signature for the formation of ordered structures: for a crystallized beam, collisions are completely suppressed due to the fixed relative ion positions in the beam. However, other interpretations of this phenomenon assuming ad-

ditional heating processes or effects of the bunched cooling mechanism itself cannot be excluded. Anomalous beam behavior during laser cooling has also been observed at ASTRID leading to density limitations [Madsen et al., 1999] and sudden transverse beam blowups monitored with real-time imaging methods [Kjærgaard et al., 2000]. However, these effects have not been observed with dispersively cooled beams.

In order to rule out effects related to the bunched cooling method, experiments on coasting beam cooling in a one-dimensional optical molasses have been carried out. Cooling of a coasting beam is achieved using a second counterpropagating laser to apply a decelerating force thus forming a one-dimensional optical molasses. We present the technical aspects of this cooling scheme such as the laser system as well as a detailed investigation of the cooling dynamics. In addition we demonstrate the first realization of full 3D laser cooling of a coasting ion beam in a storage ring.

This thesis is organized as follows: Chapter 2 gives an introduction to the basic principles as well as the experimental techniques needed for efficient laser cooling of fast stored ions. The dynamics of bunched laser cooling on the basis of systematic measurements and computer simulations is presented in chapter 3. Here we also describe the sudden anomalous behavior of the laser-cooled ion beam at extreme phase-space densities. Chapter 4 covers the description and the results of coasting beam cooling experiments in a one-dimensional optical molasses. An outlook to future experiments is given in chapter 5.

# Chapter 2

# Basics of ion beam cooling

## 2.1 Fast stored ion beams

Fast ion beams moving with velocities in the order of the speed of light can be stored in an ultra-high vacuum pipe employing the Lorentzian force $\vec{F} = q(\vec{v} \times \vec{B})$ via magnetic fields [Wille, 1996]. Magnetic dipole fields perpendicular to the direction of motion are used to deflect the beam in order to form a *closed orbit* (figure 2.1).

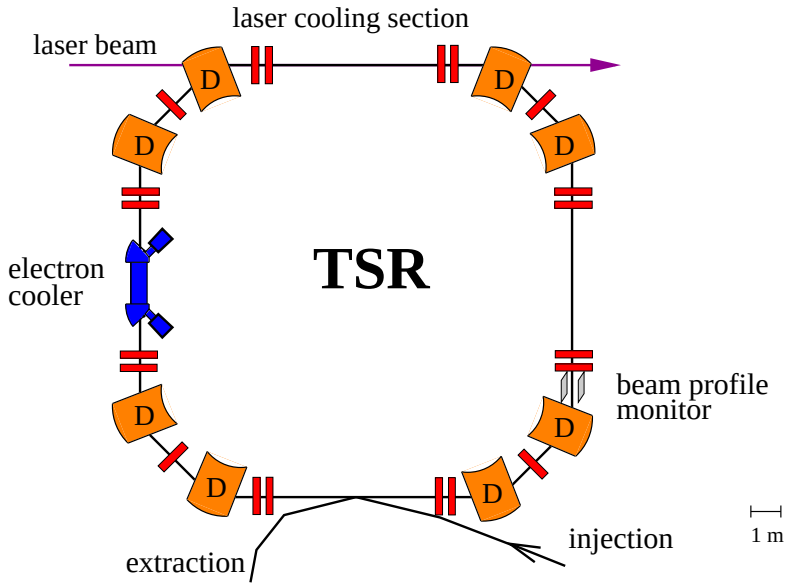


**Figure 2.1:** *Schematic picture of the Heidelberg Test Storage Ring (TSR).*

Due to the mutual repulsive Coulomb interaction and the unavoidable angle spread in the direction of motion, the beam has also to be confined in the transverse

degree of freedom in order to produce stable particle trajectories. A magnetic quadrupole field provides a focusing force in one direction and a defocusing one in the other. It has been shown that the use of quadrupole pairs can be used to confine the motion of the revolving ions in both directions (alternate gradient focusing) [Courant and Snyder, 1958]. In this magnetic structure (*lattice*), ions perform an oscillatory motion around the closed orbit (*betatron oscillation*). This motion in the transverse degree of freedom $x$ for a longitudinal position $s$ in the storage ring is described by

$$x(s) = \sqrt{\epsilon\beta(s)}\cos\Psi(s) \quad . \tag{2.1}$$

The amplitude consists of the emittance $\epsilon$ which is a constant of motion corresponding to the occupied phase-space volume and the storage ring function $\beta(s)$ which relates to the focusing strength of the quadrupole magnets. The phase $\Psi(s)$ is calculated as $\Psi(s) = \int_0^s ds'/\beta(s')$. The number of oscillation per round-trip (*tune* $Q = \Psi(C)/2\pi$, $C$: ring circumference) must not be an integer number which would drive the betatron oscillation leading to an immediate particle loss (*storage ring resonance*).

The velocity dependence of the Lorentzian force leads to a different bending radius for ions moving with different velocities. Hence, the closed orbit grows or shrinks with respect to the longitudinal momentum (*storage ring dispersion*). The orbital displacement $\Delta x$ in the horizontal degree of freedom with respect to the relative change of longitudinal momentum is described by

$$\Delta x(s) = D(s)\frac{\Delta p}{p} \quad . \tag{2.2}$$

As we will see, this important coupling mechanism between the longitudinal ion motion and its transverse position will be exploited for efficient transverse beam cooling.

## 2.2 Cold ion beams

### 2.2.1 Beam temperatures

Strictly speaking, the term *temperature* is only defined for particle ensembles being in thermal equilibrium. As we will see in the following sections, this is not the case for beam cooling at a storage ring. The correct thermodynamic description would require a Fokker-Planck approach [Risken, 1989]. This equation delivers correct results for electron-cooled beams. However in case of laser cooling the assumption of a constant diffusion coefficient is no longer valid due to the significant influence of intra beam scattering on the cooling process (section 2.2.2).

All known techniques used for beam cooling at storage rings show a strongly different cooling dynamics for the transverse and the longitudinal degrees of freedom. This leads to a strong anisotropy of the 3D ensemble. Since the number density of the ion beam is low enough to neglect all thermal couplings in first order approximation, one can treat the three degrees of freedom as distinct thermodynamic ensembles interacting with each other (figure 2.2). In case of laser cooling, even the longitudinal phase-space itself does not reach an equilibrium in a thermodynamic sense but a steady state only. The reason for that is the strong non-linearity of the cooling force (section 2.3).

For the longitudinal degree of freedom it is convenient for the description to use a frame moving with the main velocity of the circulating ions. In this picture the description only includes the position $\Delta s$ and the velocity $\Delta v$ of the ions with respect to the moving frame. The longitudinal energy is the sum of potential an kinetic energy $E(\Delta s, \Delta v) = E_{\mathrm{pot}}(\Delta s) + E_{\mathrm{kin}}(\Delta v)$. Since there are no additional mechanisms leading to an energy term which depends on both velocity and position, the phase-space can be separated in a spatial and a velocity distribution.

Although the longitudinal ion ensemble is not in thermal equilibrium, one can ascribe a measure for the velocity spread of the distribution which has the dimension of a temperature

$$T_{\parallel} = \frac{\langle E_{\mathrm{kin}}(\Delta v)\rangle}{k_{\mathrm{b}}} \quad , \tag{2.3}$$

where $\langle E_{\mathrm{kin}}(\Delta v)\rangle$ is the mean kinetic energy of the ion beam in the comoving frame. It can be calculated from the variance $\sigma_v^2$ of the velocity distribution ($\langle E_{\mathrm{kin}}\rangle = m\sigma_v^2$). Therefore one gets

$$T_{\parallel} = \frac{m}{k_{\mathrm{b}}}\sigma_v^2 \quad , \tag{2.4}$$

($m$: ion mass). One has to bear in mind that the velocity spread $\sigma_v$ is *not* bound to a certain shape of the velocity distribution but follows the general relation $\sigma_v = \sqrt{\langle \Delta v\rangle - \langle (\Delta v)^2\rangle}$. For a thermally equilibrated ensemble one would expect a Gaussian shape according Boltzmann's distribution . In this case the above relation corresponds exactly to the thermodynamic definition of a temperature.

In order to get a temperature of the transverse degree of freedom we can express the energy $E(x, x')$ by the particle momentum and the lattice functions $\alpha, \beta$ [Wille, 1996]. Again, the transverse beam energy is the sum of potential and kinetic energy. Without any cooling mechanisms, the transverse beam energy is a constant of motion. The potential energy results from the focusing structure (quadrupole magnets) of the storage ring. Since the focusing strength is not constant along the ring position, also the transverse kinetic energy depends on the

storage ring position. In conclusion one would end up with a position-dependent transverse beam temperature using the above temperature definition which does not make much sense. Therefore in storage ring physics one calculates the mean *beam emittance* $\epsilon_{\mathrm{rms}}$ which corresponds to the transverse phase-space volume enclosed by the ion beam ensemble.

$$\beta\epsilon_{\mathrm{rms}} = \langle x^2 \rangle \quad . \tag{2.5}$$

where $\langle x^2 \rangle = \int_{-\infty}^{+\infty} x^2 \cdot n(x)dx$ denotes the second statistical moment of the ion distribution [Mudrich, 1999]. The emittance is also a constant of motion and does not depend on the ring position.

A solution for the temperature definition is the calculation of a mean temperature by averaging the position-dependent temperature along one round-trip

$$T_\perp = \frac{1}{C}\oint_C T(s)ds = \frac{p_0^2\epsilon_{\mathrm{rms}}}{k_{\mathrm{B}}mC}2\pi Q \quad . \tag{2.6}$$

($C$: ring circumference, $Q$: betatron tune).

It is worth noting that the temperature definitions are still valid for ion beams experiencing additional forces that only depend either on the velocity or the position. In particular for very dense beams one has to take into account the mutual Coulomb interaction of the ions and space-charge effects [Ellison et al., 1993, Nagaitsev et al., 1994]. These effects could be described using a Debye-Hückel approach [Eisenbarth, 1998].

### 2.2.2 Intra beam scattering

For a stored ion beam, one observes a heat-up if no cooling mechanisms are present. The reason for this behavior is the so called *envelope heating* [Hochadel, 1994b]. This effect relies on the changing focusing of the horizontal and vertical degree of freedom (alternate gradient focusing, see 2.1). Since the transverse beam temperature at a certain ring position depends on the focusing strength of the quadrupole field, a focusing in one direction and a defocusing in the other one leads to a strong temperature anisotropy. Without any coupling of both degrees of freedom this effect would be completely reversible. Intra beam Coulomb scattering (IBS) however leads to a heat transfer which reduces this anisotropy [Sørensen, 1987]. The result is an increase of the entropy and thus the mean beam temperature. The energy for this heat-up comes from the kinetic beam energy acting as a huge heat bath.

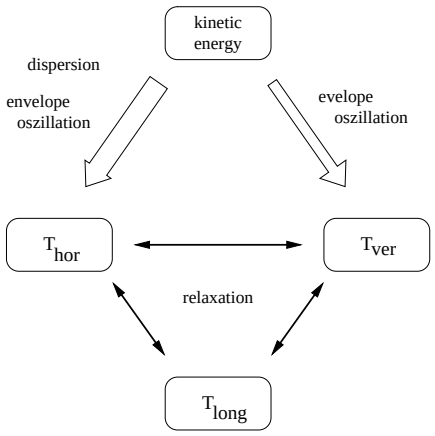


**Figure 2.2:** *Energy transfer in a stored ion beam. Thermal energy from the longitudinal beam motion is transfered through envelope oscillations in connection to intra beam Coulomb scattering to the three degrees of freedom.*

### 2.2.3 Cooling rate

As a result of the introduced temperature definitions, cooling of stored ion beams means the reduction of the longitudinal momentum spread and the the damping of the transverse betatron oscillation respectively. In order to characterize the efficiency of a particular cooling mechanism one defines the *cooling rate* $\Lambda$ as

$$\Lambda \cdot \overline{E} = -\frac{\partial \overline{E}}{\partial t} \quad . \tag{2.7}$$

$\overline{E}$ denotes the total energy spread of the stored ions moving around the mean energy $E$. Hence, the cooling rate corresponds to the time constant of the decreasing relative energy spread during the cooling process. The total energy consists of a potential and a kinetic part $\overline{E} = \overline{E_{\mathrm{kin}}(\Delta v)} + \overline{E_{\mathrm{pot}}(\Delta s)}$, whereby velocity-dependent cooling forces only reduce the kinetic energy spread:

$$\frac{\partial \overline{E_{\mathrm{kin}}}}{\partial t} = m\Delta v\dot{\Delta v} = F_{\mathrm{C}}(\Delta v)\Delta v \simeq \frac{\partial F_{\mathrm{C}}}{\partial \Delta v}\Delta v^2 \quad , \tag{2.8}$$

assuming $F_{\mathrm{C}}(\Delta v)$ to be linear near $\Delta v = 0$. For the longitudinal degree of freedom of a coasting beam the particles have no potential energy leading to $\overline{E_{\mathrm{kin}}} = \overline{E}$ and thus

$$\Lambda = -\frac{2}{m}\left.\frac{\partial F_{\mathrm{C}}(v)}{\partial v}\right|_{v=0} = -\frac{2}{m}\alpha \quad . \tag{2.9}$$

In the last expression $\alpha$ is the so-called *friction coefficient*. In case of ions in a harmonic potential (as it is approximately the case for the transverse degree of

freedom) the viral theorem requires that $\langle\overline{E_{\mathrm{kin}}}\rangle = \langle\overline{E_{\mathrm{pot}}}\rangle$. Hence, the cooling rate would be half the value of Equation. 2.9.

### 2.2.4 Beam crystallization

During beam cooling the phase-space density of the ensemble becomes steadily higher and higher. In this case the mutual Coulomb interaction of the ions can no longer be neglected. The whole dynamics of such a cold beam becomes more and more dominated the the intra-beam interactions.

A fast stored ion beam of high phases-space density can be treated as a one-component, non-neutral and space-charge dominated plasma. Such a plasma is characterized by the *plasma parameter*

$$\Gamma = \frac{E_{\mathrm{Coulomb}}}{E_{\mathrm{therm}}} = \frac{1}{4\pi\epsilon_0} \cdot \frac{q^2}{a k_{\mathrm{B}} T} \tag{2.10}$$

which represents the ratio of the Coulomb energy due to the repulsive electrostatic forces between neighboring ions and the temperature of the ensemble. For an isotropic plasma, the characteristic distance $a$ becomes the Wigner-Seitz radius $a = \sqrt[3]{3/(4\pi n)}$ where $n$ is the spatial number density [Habs and Grimm, 1995]. With this definition a thermal weakly coupled plasma is expressed by $\Gamma \ll 1$. A short-range one dimensional liquid-like state would be expected for $\Gamma \approx 1$. In this case the thermal energy is in the same order of the Coulomb energy. This means that two stored ion moving with slightly different velocities cannot overtake each other due to their Coulomb repulsion. In this case, the ion beam should show up ordering effects. A long-range order is expected for $\Gamma > 170$ [Hasse, 1999]. The shape of this ordered structure depends on the ion density. At large ion distances the lowest order structure would be a linear chain. With decreasing distances the ions start evading from each other forming a zig-zag line or helix-like structures [Hasse and Schiffer, 1990]. For an ion beam stored in the TSR it is expected that only the linear chain and possibly the vertical zig-zag structure to be stably storagable. Higher order 3D structures would experience strong shear forces during beam deflection at the bending magnets.

For the treatment of laser-cooled ion beams one has to take into account that the 3D ensemble of the cooled beam is far away from thermal equilibrium. Due to the extreme temperature anisotropy ($T_{\parallel} \simeq 1\,\mathrm{K}$, $T_{\perp} \geq 200\,\mathrm{K}$) a more realistic picture of an ordered beam is shown in figure 2.3. While a laser-cooled ion beam has a very small velocity spread, the transverse degree of freedom is comparably weakly cooled. An ordered beam would therefore lead to a spatial distribution, where ions have a well-defined longitudinal intermediate distance from each other but their betatron amplitudes are still large. The ion beam can therefore be seen as

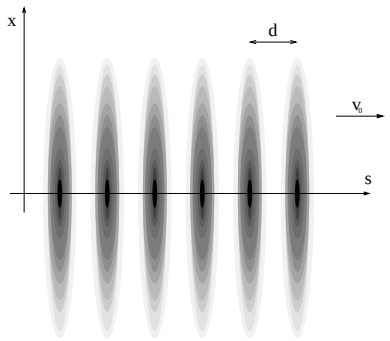


**Figure 2.3:** *Disk model of a crystallized ion beam. While ions have well-defined longitudinal distances they still oscillate with large betatron amplitudes.*

a set of charge disks with a distance $d$ and a transverse size of $\sigma$ assuming a radial Gaussian charge distribution. Obviously, in this case the above definition of the plasma parameter does not make sense any longer. However, a *one-dimensional plasma parameter* can be defined representing the ratio of the Coulomb energy of two charge disks and the thermal energy of the longitudinal degree of freedom ($\Gamma_{\|} = E_{\mathrm{long}}(d,\sigma)/E_{\mathrm{therm}}(T_{\|})$). The Coulomb energy of two charge disks with the radial charge distributions $\rho_1(\vec{x})$ $\rho_2(\vec{x}')$ is calculated as

$$E_{\mathrm{long}}(d,\sigma) = \int_{-\infty}^{d} F_{\mathrm{s}}(l,\sigma)dl \quad , \tag{2.11}$$

with

$$F_{\mathrm{s}}(l,\sigma) = \frac{1}{4\pi\epsilon_0}\int d^3x \int d^3x' \frac{\rho_1(\vec{x})\rho_2(\vec{x}')}{|\vec{x}-\vec{x}'|}(s-s') \quad . \tag{2.12}$$

Through the intermediate distance $d$ this definition also take the linear number density into account by $1/d = dN/ds$. Note, that this definition gives no quantitative measure in case $\Gamma_{\|} \ll 1$ for phase-space but a qualitative deviation from an ordered state.

For very low beam densities, the intermediate particle distance $d$ is small compared to the amplitude $x$ of the betatron oscillation. In this case, the one-dimensional definition of the plasma parameter gives way to the 3D definition. In the comoving frame, the transversally oscillating ions approach each other until they are reflected due to the repulsive Coulomb interaction (figure 2.4. In this picture, it is possible to estimate a transverse beam temperature needed to observe Coulomb ordering: The minimum distance between to approaching ions is

$$d = \frac{1}{4\pi\epsilon_0}\cdot\frac{q^2}{k_{\mathrm{B}}T_{\|}} \quad . \tag{2.13}$$

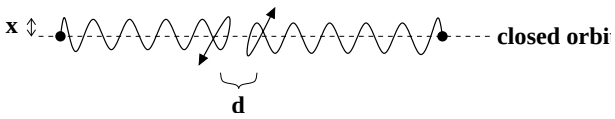


**Figure 2.4:** *Beam crystallization can be treated as a one-dimensional problem if the intermediate distance $d$ is small compared to the betatron amplitude $x$. Ions approach each other and are reflected due to the repulsive Coulomb interaction.*

The betatron amplitude can be estimated as

$$x = \sqrt{\frac{2k_{\mathrm{B}}T_{\perp}}{m}} \cdot \frac{1}{2\pi\nu_{\beta}} \quad , \tag{2.14}$$

with the betatron frequency $\nu_beta$. The combination of both equations with the assumption $x \ll d$ leads to an estimation of the transverse temperature for a given longitudinal temperature

$$k_{\mathrm{B}}T_{\perp} \ll \frac{m}{2}\left(\frac{\nu_{\beta}}{2\epsilon_0} \cdot \frac{q^2}{k_{\mathrm{B}}T_{\parallel}}\right)^2 \quad . \tag{2.15}$$

At the experimental conditions ($^9Be^+$ at TSR), a longitudinal temperature of $T_{\parallel} \simeq 1\,\mathrm{K}$ leads to $T_{\perp} \ll 1\,\mathrm{K}$. For $T_{\parallel} \simeq 100\,\mathrm{mK}$ a transverse temperature of $T_{\perp} \ll 100\,\mathrm{K}$ would be necessary.

## 2.3 Laser cooling

As shown above, beam cooling means a reduction of the velocity spread of the ion ensemble. According to Liouville's theorem, phase-space density is a constant of motion if one uses only conservative forces. Hence, one way to achieve beam cooling is the use of velocity-dependent friction forces. This force must be able to accelerate ions moving too slow as well as decelerate ions moving too fast. At the storage ring, two methods are used to compress phase-space: electron cooling and laser cooling. For electron cooling the hot ion beam is merged with a cold electron beam. Through Coulomb collisions between ions and electrons, the electron beam acts as a heat sink for the ion beam. Ions moving to slow are accelerated by the ion beam and vice versa. The mean velocity where the revolving ions are drawn to is determined by the velocity of the electron beam. In our experiments, the electron cooler is used to precool the hot ion beam right after injection before starting laser cooling. A more detailed description of electron cooling is given in Appendix A. On the other hand, laser beams being resonant with an atomic transition of the stored ion species offers an elegant way to apply friction forces to the beam.

### 2.3.1 Longitudinal cooling

Laser cooling exploits the resonant light pressure force acting on ions or neutral atoms while interacting with photons [Metcalf and van der Straten, 1994]. During repeated absorption and emission processes the atom experiences momentum exchanges with the photons. While the momentum transfer during an absorption process always takes place in direction of the laser beam, a spontaneous emission emits the photon statistically in *any* direction. Therefore, the mean momentum transfer over many emission cycles vanishes ($\langle \hbar\vec{k} \rangle = 0$). For the absorption process however, the mean transferred momentum becomes $\langle \vec{p} \rangle = \hbar\vec{k}$. The resulting force acting on the ion is the product of the momentum transfer and the scattering rate $r(\omega_{\mathrm{D}})$ for a given laser frequency $\omega_{\mathrm{D}}$ which corresponds to a Lorentzian function:

$$r(\omega_{\mathrm{D}}) = \frac{\Gamma}{2} \cdot \frac{S}{1 + S + \left(\frac{2(\omega_{\mathrm{D}} - \omega_0}{\Gamma}\right)^2} \tag{2.16}$$

($\Gamma$: natural line width of the transition, $\omega_0$: atomic transition frequency at rest, $S$: saturation parameter). For an ion moving with a velocity $\vec{v}$ the Doppler effect leads to a shift of the transition frequency in the laboratory frame: $\omega_{\mathrm{D}} = \gamma(\omega_0 + \vec{k}_0 \cdot \vec{v})$. Hence, one gets a velocity-dependent laser cooling force

$$\vec{F}_{\mathrm{las}} = \langle \Delta\vec{p} \rangle \cdot r(\omega_{\mathrm{D}}) = \hbar\vec{k}_{\mathrm{L}} \cdot \frac{\Gamma}{2} \cdot \frac{S}{1 + S + \left(\frac{2\Delta(v)}{\Gamma}\right)^2} \quad , \tag{2.17}$$

with $\Delta(v) = \omega_{\mathrm{L}} - \gamma(\omega_0 + \vec{k}_0 \cdot \vec{v})$. For laser cooling at a storage ring the laser is superimposed with the ion beam only over a fraction $\eta$ of the whole ring circumference. Thus, the ring-averaged cooling force becomes $F_{\mathrm{avg}} = \eta \cdot F_{\mathrm{las}}$. A plot of the force profile for $^9\mathrm{Be}^+$ ions is shown in figure 2.5.

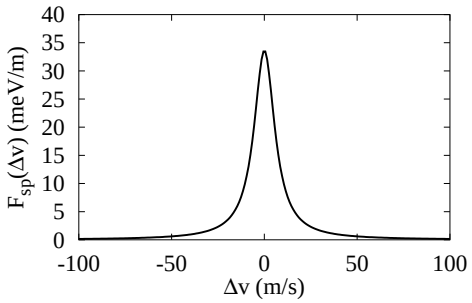


**Figure 2.5:** *Calculated laser force profile in velocity space for the case of $^9$Be+ ions in the storage ring TSR. The velocity range in which the laser force is notably present is roughly 150 m/s.*

In case of a copropagating beam, one attains an accelerating force. As mentioned above, beam cooling requires the existence of both accelerating and decelerating forces. Hence, an additional counterforce has to be applied. First cooling experiments at TSR were performed with an induction accelerator (INDAC) [Ellert et al., 1992]. This device exploits the transformer principle to generate a counter force: According Faraday's law, a linear current ramp in a coil covering the beam pipe leads to an induction voltage in the second coil which is in our case the ion beam itself. This induction voltage leads to a constant accelerating or decelerating force acting on the ions whose strength depends on the slope of the current ramp. Together with the laser interaction, the resulting cooling force profile is shown in figure 2.6 Since the maximum current in the primary coil must

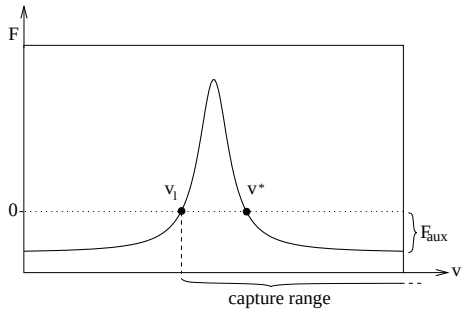


**Figure 2.6:** *Laser cooling with a constant counter force as provided by the induction accelerator. The velocity $v^*$ denotes the stable point of the cooling force where the ions are drawn to. The second zero crossing $v_1$ is an unstable point. Ions are pushed apart from it.*

not exceed a given limit, the counterforce can only be generated for a limited amount of time. One therefore has to find a compromise between the strength of the counterforce which determines the cooling rate and the time this force can be generated. A comparably week counterforce of $F_{\mathrm{aux}} \approx 1\,\mathrm{meV/m}$ would lead to a maximum cooling time of 10 seconds while a force of $\approx 18\,\mathrm{meV/m}$ lowers this limit to less than 60 ms. Hence, a detailed investigation of long-term beam dynamics during cooling is not possible.

In this work, two more elegant methods are presented to realize a counter force. On the one hand we make use of an external longitudinal confining potential achieved by beam bunching as presented in chapter 3. A counterforce can also be realized by applying a second counterpropagating laser which leads to a force profile depicted in figure 2.7. Experiments using this scheme are presented in chapter 4.

Both force profile have a *stable point* $v^*$ in velocity space where the cooling force vanishes. Due to the negative derivative ($\partial F/\partial v < 0$), ions are drawn to this

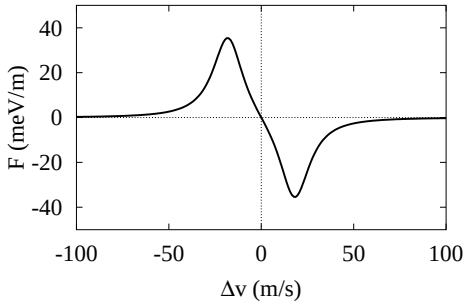


**Figure 2.7:** *Calculated cooling force of an optical molasses consisting of a co- and a counterpropagating laser with respect to the ion beam.*

point in velocity space. The slope at this point determines the cooling rate (see section 2.2).

While the maximum laser force can become very strong (the maximum acceleration being achieved corresponds to roughly $10^5 g$!) the velocity range of $\simeq 150$ m/s in which the cooling force is apparent is comparably small. This width also defines the *capture range* of the cooling force. Since velocity changes due to hard intra beam Coulomb collisions can be on the order of 1000 m/s this property of the cooling force has a major influence on the cooling dynamics which is discussed in the next chapter.

However, it is possible to extend the capture spanning a broader velocity range by exploiting the *rapid adiabatic passage* technique described in detail in [Wanner et al., 1998]. For this purpose, ions are repeatedly accelerated and decelerated by passing a set of high-voltage drift tubes as shown in figure 2.8. In the comoving frame of the ions, these velocity changes correspond to frequency chirps of the cooling laser which lead to an excitation of ions in a broad velocity range. This effect leads to a modified laser force as depicted in figure 2.9.

Another possibility is the direct modification of the frequency profile of the laser using a comb of frequencies produced by an acousto-optical modulator. This cooling scheme has also been demonstrated at TSR [Atutov et al., 1998].

### 2.3.2 Transverse cooling

So far, a laser superimposed with the ion beam directly cools only the longitudinal degree of freedom (figure 2.10). A direct cooling of the transverse degrees of freedom using additional laser beams installed perpendicular to the direction of motion is practically impossible: On the one hand, the interaction time of some picoseconds would be far too short to achieve efficient beam cooling. On the other hand, the use of perpendicular laser beams would be extremely sensitive

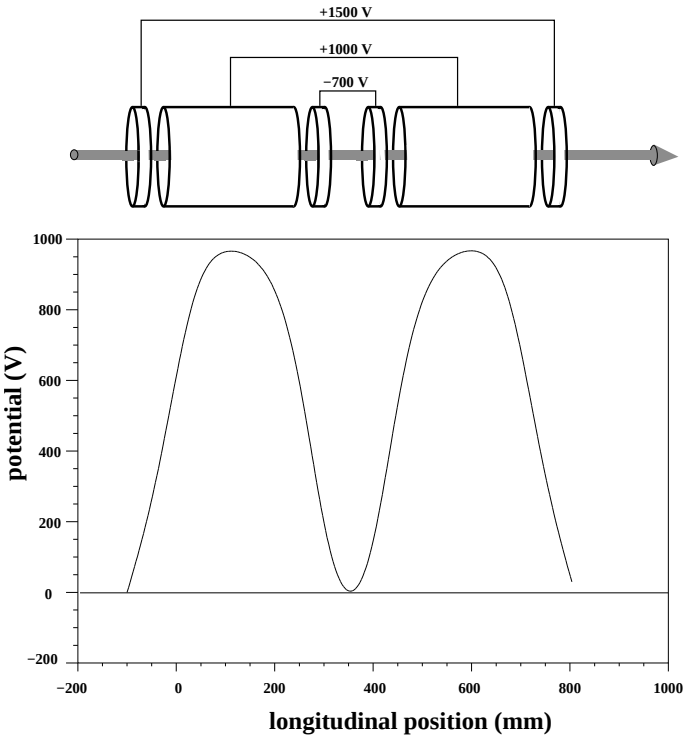


**Figure 2.8:** *Calculated potential profile of the drift tube section for the realization of a rapid adiabatic passage. The repeated velocity changes of passing ions leads to a broadband excitation which is exploited as a capture range of the laser force.*

to small angle deviations. Even an angle misadjustment on the order of $\delta\phi \simeq 0.01\,\mu$rad would lead to a Doppler shift of roughly one atomic resonance width ($\delta\nu \simeq 60\,$MHz), so that the ion would no longer experience the laser force.

However, cooling of the transverse degree of freedom can be indirectly achieved exploiting coupling mechanisms between the longitudinal and transverse directions. As described in section 2.2.2 IBS permanently leads to a thermal relaxation between all degrees of freedom. In this system, the longitudinal very efficiently cooled degree of freedom acts as a heat sink for the transverse direction. Therefore, the relaxation process also leads to a reduction of the transverse temperature [Miesner et al., 1996b]. The coupling and thus the transverse cooling rate strongly depends on the collision rate of the ions. This rate itself depends on the ion density. Hence, this cooling mechanism is a multi-particle effect and becomes inefficient for very dilute beams. In addition, for a beam crystallization one expects a complete disappearance of IBS which also stops transverse cooling. Therefore, the observation of Coulomb ordering requires a

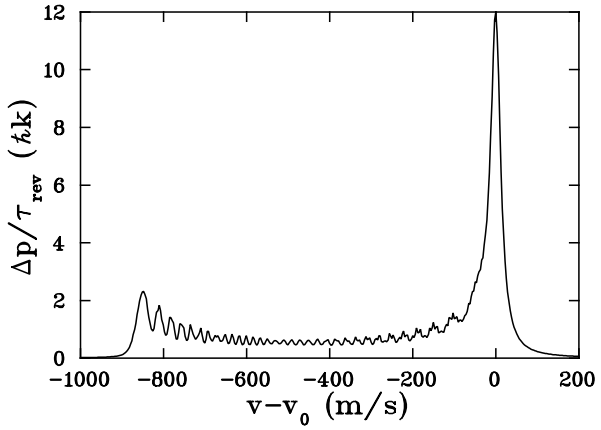


**Figure 2.9:** *Calculated laser force profile using the capture range extension. Even ions far away from the laser resonance in velocity space still experience a light pressure force.*

single-particle cooling mechanism. Such a cooling mechanism has been realized in [Lauer et al., 1998, Lauer, 1999, Grimm et al., 1998]. This method employs the coupling through the storage ring dispersion (see section 2.1) in connection with the horizontal gradient of the longitudinal laser cooling force. Figure 2.11 shows in two extreme cases the influence of the dispersion on an ion performing betatron oscillations around its closed orbit while changing the longitudinal momentum by photon absorption. In the first case (a), the ion changes its momentum at the outer turning point of the oscillation. The shift of the closed orbit leads to a damping of the betatron amplitude. In picture (b) the ion absorbs a photon being on the opposite turning point of the oscillation. The ion is accelerated which leads to the same orbit shift as in the first case. This leads to a driving of the oscillation. The first process corresponds to horizontal cooling and can be preferred against the second process by a horizontal shift of the Gaussian intensity laser profile outwards with respect to the position of maximum intensity of the ion beam. A shift of the laser inwards therefore leads to a heating of the beam. The maximum cooling or eating rate can be achieved with a horizontal laser shift corresponding to a half Gaussian beam waist ($\omega_0/2$). Since a storage ring has only a notable dispersion in the horizontal degree of freedom, the presented cooling method would be limited to this direction. However, it is possible to couple both transverse degrees of freedom through *linear betatron coupling* [Bryant, 1994]. In this case the horizontal and the transverse tunes are equal due to an adjustment of the magnetic ring lattice. In the following, this 3D cooling method is called *dispersive cooling*.

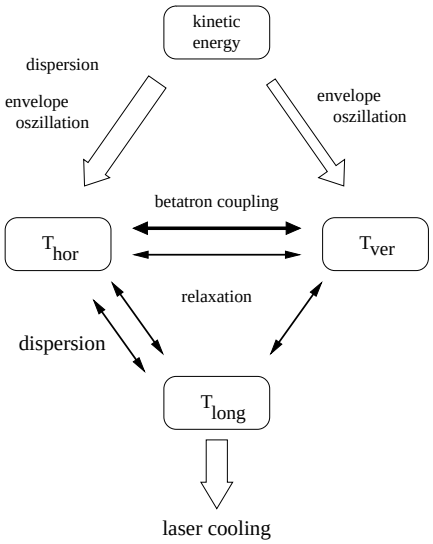


**Figure 2.10:** *Heat transfer of a cooled ion beam. For transverse beam cooling, the ring dispersion can be exploited providing a coupling between the longitudinal and the transverse degree of freedom. Full 3D cooling is realized using linear betatron coupling.*

## 2.4 Experimental techniques

The experiments are performed at the Heidelberg Test Storage Ring (TSR) with singly charged $^9Be^+$ ions at an energy of 7.3 MeV which corresponds to 4.1% of the speed of light. A ring circumference of 55.4 m leads to an ion revolution frequency of 225 kHz. A typical ion current after multi-turn injection [Bisoffi et al., 1990] of 1$\mu$A corresponds to $10^7$ ions in total. The lifetime of the

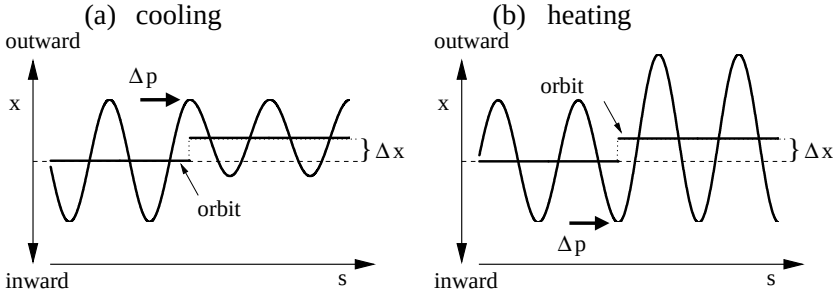


**Figure 2.11:** *Dispersive cooling principle. A longitudinal change of momentum leads to a shift of the closed orbit which can be exploited to damp (a) or drive (b) the transverse betatron oscillation.*

stored beam limited due to collisions with rest gas atoms is about 30 seconds at a vacuum of $5 \cdot 10^{-11}$ mbar.

### 2.4.1 Laser system at 300 nm

For laser cooling, one uses the $^2S_{1/2} \rightarrow^2 P_{3/2}$ transition with a wavelength of $\lambda = 313.13$ nm at rest. The corresponding level diagram is shown in figure 2.12. The lifetime of $\tau = 8.3 \cdot 10^{-9}$ s leads to a resonance width of $\Gamma = 19.4$ MHz. The

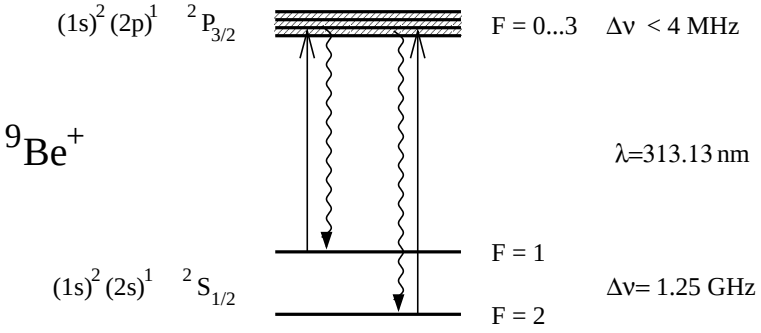


**Figure 2.12:** *Term scheme of $^9$Beryllium$^+$. For laser cooling, the transition $^2S_{1/2} \rightarrow^2 P_{3/2}$ is used.*

beam energy of 7.3 MeV corresponding to a velocity of $1.24 \cdot 10^7$ m/s ($\simeq 4.1\%c$) leads to a Doppler shift of 12.83 nm. Due to a ground state hyperfine splitting of 1.3 GHz (in laboratory frame) a second accordingly detuned laser system is needed to avoid optical pumping between both states. Note, that the $^2P_{3/2}$ level is also hyperfine split in 4 levels. However the splitting of these levels is less than 4 MHz which is smaller than the natural line width of the cooling transition, so that these lines cannot be resolved. The wavelengths are generated by two Argon-ion lasers (Coherent INNOVA 200 and 400) with an output light power of about 90 mW each (figure 2.13). In order to achieve stable cooling conditions the *master* laser is frequency locked against an ultra-stable Helium-Neon laser by a Fabry-Perot resonator [Becker, 1992, Gruber, 1993]. The detuning between the master and the *slave* laser is stabilized by a direct measurement of the beating signal of both superimposed laser beams with a fast avalanche photodiode. The measured frequency is compared with a local quartz oscillator in order to produce an error signal which is used to change the frequency of the slave laser accordingly [Schünemann et al., 1999]. The merged laser beams go through a telescope such that the focus is exactly in the middle of the cooling section in the storage ring. A change of the lens configuration makes it possible to adjust the laser beam waist in the experiment section. The overall distance between the laser system and

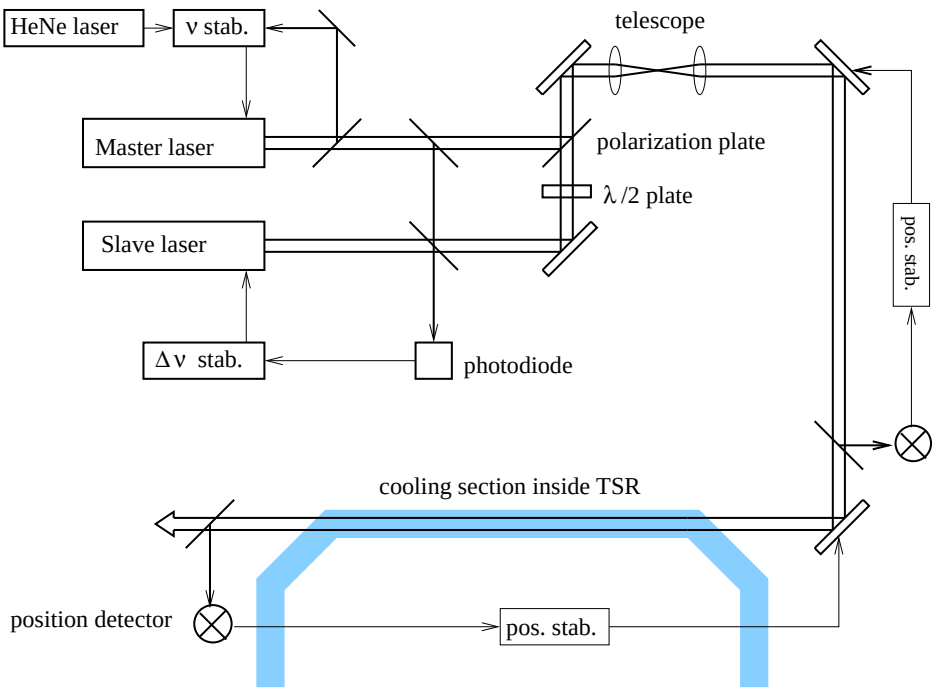


**Figure 2.13:** *Basic laser setup. Two argon ion lasers at 300 nm with a relative detuning of 1.3 GHz are superimposed in order to avoid optical pumping between the hyperfine-split ground states.*

the ring section is about 23 m. Due to mechanical vibrations and changes in the refractive index of the air the laser beam shows position fluctuations that cannot be neglected. To suppress these fluctuations and to precisely position the beam we use an active regulation system consisting of a set of piezo mirrors and position-sensitive photodiodes [Wernøe, 1993]. The achievable positioning accuracy is about 100 $\mu$m. With this technique it is possible to attain an overlap with the ion beam of more then 5 m.

### 2.4.2 Beam bunching

For laser cooling, an additional conterforce has to be provided. One method to realize this counterforce is beam bunching where the ions are longitudinally confined in a pseudopotential. Beam bunching is a well-established method for the generation of ion beams moving in separate particle packets (*bunches*) [Wille, 1996]. For beam bunching in a storage ring, ions pass a longitudinal electrical radio frequency field tuned at a harmonic $h$ of the ion revolution frequency $\nu_{\mathrm{rev}}$ ($\nu_{\mathrm{rf}} = h\nu_{\mathrm{rev}}$). Usually, the RF field is applied by a dedicated resonant

bunching device [Blum, 1989] which is limited to the use of sinusoidal potentials. For our purposes, non-sinusoidal waveforms have been applied to a non-resonant kicker device. This device consists of a pair of parallel plates with a length of $L \approx 20\,\text{cm}$ as shown in figure 2.14. Each kicker plate is set to the same potential,

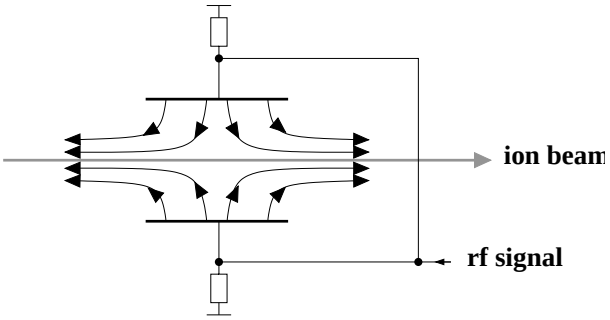


**Figure 2.14:** *Experimental setup for beam bunching using non-resonant kicker plates.*

so that ions only experience forces along the beam axis exploiting the stray fields. Due to these stray fields ions effectively see a longer set of plates expressed by the effective length $L_{\text{eff}}$. This length can be indirectly measured using Schottky analysis as explained in Appendix A.

Ions enter the pair of plates at the voltage $U(t)$ and leave at $U(t+\Delta t)$, where $\Delta t$ is the time needed for passage. Therefore, the ions run through a net potential difference $\Delta U(t) = U(t) - U(t+\Delta t) \approx \dot{U}(t)\Delta t$ assuming $\Delta t$ to be short. This results in a phase-dependent, ring-averaged force $F_{\text{rf}}(t) = e\Delta U(t)/C$ in the longitudinal direction ($C$: ring circumference). With the relation $t(s) = \gamma^2 \eta h s/(\nu_{\text{rf}} C)$ between time and the longitudinal position $s$ in the comoving frame ($\gamma \approx 1$: relativistic parameter, $h$ harmonic number, $\eta$ machine parameter) one calculates the position-dependent force

$$F_{\text{rf}}(s) = \frac{e}{C}\Delta U\left(t(s)\right) \quad . \tag{2.18}$$

Furthermore, one can ascribe a longitudinal pseudopotential to this force:

$$V_{\text{rf}} = \frac{eL_{\text{eff}}\nu_{\text{rf}}}{\gamma^2 \eta v_{\text{ion}}} U(t(s)) \tag{2.19}$$

Note that the pseudo potential corresponds to a simple linear transformation of the applied RF-voltage, and the shape of the potential reflects the RF-waveform. The bunching frequency defines the *synchronous velocity* $v_{\text{synch}} = \nu_{\text{rf}} C/h$ of the pseudopotential moving in the ring. The harmonic number determines the number of bunches per round-trip and therefore the bunch length $l_{\text{bunch}} = C/h$.

In chapter 3 we investigate the influence of different potential shapes on the efficiency of laser cooling. Besides the sinusoidal potential we made use of dedicated *barrier buckets* that are of particular interest to study the dynamics of the cooling process [Eisenbarth et al., 2000a]. The barrier potential consists of a square-well potential which longitudinally confines the ions, and a bottom of constant slope in order to counteract the laser force. A plot a typical potential and the corresponding force is shown in figure 2.15. In contrast to sinusoidal po-

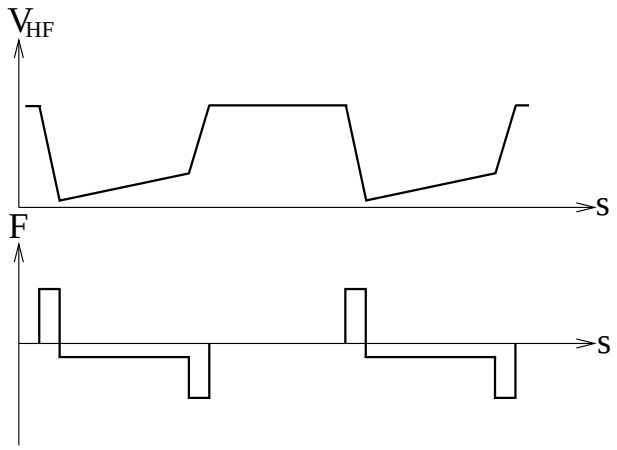


**Figure 2.15:** *Schematic picture of the barrier bucket potential consisting of a square-well potential an a bottom of constant slope. The corresponding resulting force profile is plotted below.*

tentials, the barrier bucket provides a constant, position-independent counterforce for the confined ions. Therefore, it is possible to produce a laser-cooled ion ensemble with an almost constant longitudinal ion density. This would correspond to a coasting chopped ion beam. This waveform is of particular interest for the observation of Coulomb ordering. The longitudinal ion distance being a critical parameter for the crystallization (see section 2.2.4) is also constant inside the bunch. The combination of the laser force and the counter force produced by the potential slope form an unstable equilibrium: even slight changes in the cooling condition have a strong influence on the longitudinal ion distribution which makes this method to a sensitive tool to investigate the cooling dynamics.

While cooling in barrier buckets only compresses the ensemble in velocity space, a sinusoidal potential also compresses the longitudinal spatial distribution. However, an increase in the number density leads to an unavoidable increase of intra beam scattering which further contributes to the heating rate in this system.

Ions confined in barrier buckets perform an an-harmonic oscillatory motion in the comoving frame. The longitudinal phase-space diagram for particles with

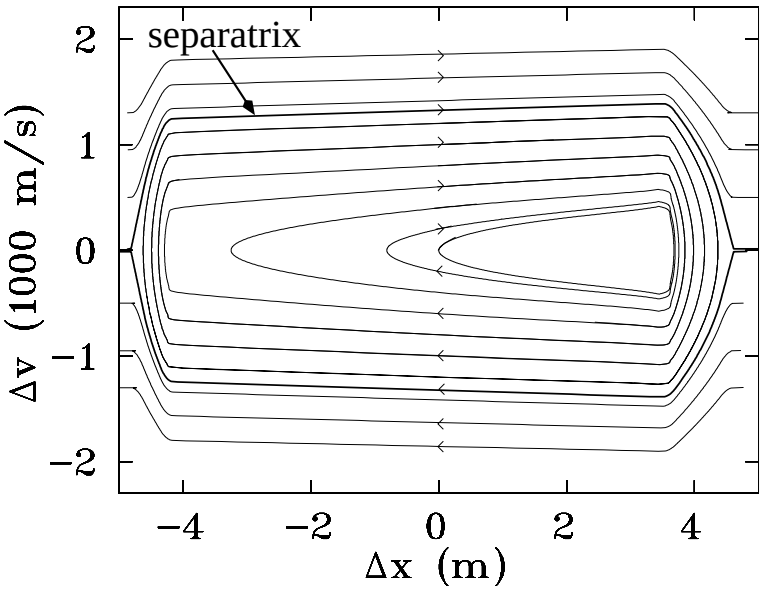


**Figure 2.16:** *phase-space trajectories of a bunched ion*

different kinetic energies is depicted in figure 2.16. Ions confined in the bucket are reflected at the bucket walls. Without any cooling, the potential slope leads to a biasing of the motion towards the right wall. Ions with velocities larger then the *bucket acceptance* are not trapped in the potential and perform an unbound motion. The trajectory between both types of motion is the *separatrix*.

Figure 2.15 and 2.16 take into account that the potential walls have finite slopes in reality. This comes from the fact that for fast voltage steps as it is the case for barrier buckets the approximation $\Delta U \approx \dot{U}(t)\Delta t$ is no longer valid. The ions are therefore "smoothly" reflected at the walls which results in the arc-shaped trajectories at the potential borders. For sinusoidal potentials, ions with small amplitudes oscillate in a nearly harmonic potential which results in a single velocity-independent *synchrotron frequency*

$$\nu_{\mathrm{sync}} = \sqrt{\frac{l_{\mathrm{eff}} h^2 eU}{2\pi m\gamma^2 C^3}} \quad . \tag{2.20}$$

For the rectangular waveform, the oscillation frequency depends on the difference $\Delta v = v_{\mathrm{ion}} - v_{\mathrm{synch}}$ of the ion velocity and the synchroneous velocity: $\nu_{osc} = h\Delta v/(2Cd)$ with the duty cycle $d$ corresponding to the on-off ratio of the square-well waveform. The maximum frequency limited by the bucket acceptance is about 100 Hz assuming a typical potential depth of $U = 30\,\mathrm{V}$. This leads to a maximum velocity deviation from the synchronous velocity of $\Delta v_{\mathrm{max}} = 1500\,\mathrm{m/s}$. The synchrotron frequency is several orders of magnitude

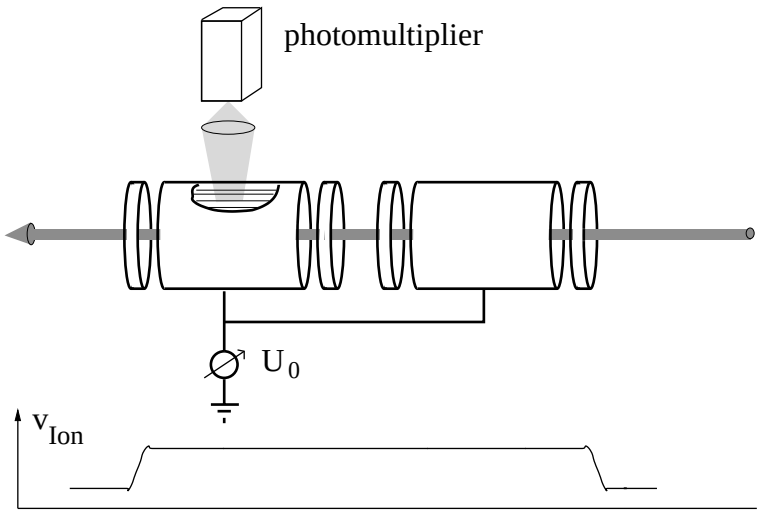


**Figure 2.17:** *High voltage drift tubes are installed at the position of the photomultipliers in order to locally accelerate or decelerate the ions.*

smaller than the betatron frequency $\nu_{\mathrm{beta}} = Q\nu_{\mathrm{rf}}/n \approx 600\,\mathrm{kHz}$ ($Q \approx 2.7$).

### 2.4.3 Diagnostic tools

The various diagnostic tools presented in the following allow the observation of the complete three dimensional phase space. The data acquisition system to actually record and store the signals for further data analysis is described in Appendix B.

#### Fluorescence measurement

The fluorescence light produced by the ions in resonance with the cooling laser is measured with two photomultiplier tubes installed perpendicular with respect to the beam pipe and 2.3 m apart from each other. The count rate corresponds directly to the number of ions in resonance with the laser. This tool can be used to optimize the overlap between the laser and the ion beam by maximizing the fluorescence count rate. Furthermore, the use of two photomultipliers allows to minimized the angle between both beams. This method leads to an angle accuracy of better then 100 $\mu$rad. In addition, a set of cylindrical high-voltage drift tubes installed around each photomultiplier are used to locally accelerate or decelerate then ions through electric fields (figure 2.17). The velocity change of the ions $\Delta v = eU_{\mathrm{tube}}/p_0$ leads to a changing Doppler shift of the absorption frequency. In the comoving frame the ions experience a shift of the laser frequency. A voltage

ramp applied to the drift tubes therefore corresponds to a continuous sweep of the laser frequency. During this sweep every velocity class of the longitudinal thermal ion distribution becomes locally resonant with the laser. The number of ions for a given velocity is measured through the particular fluorescence rate. With this so-called *HV-scan* the whole longitudinal velocity distribution can be measured. For one measured cycle a typical voltage ramp goes from -1.5 kV to +1.5 kV in 100 ms corresponding to a scan range of 1300 m/s in velocity space.

For the resulting velocity profiles one has to consider the use of a bichromatic light field driving two atomic transitions. Figure 2.18 shows the physical situation in the comoving frame of the ion. The atomic resonance frequencies are drawn

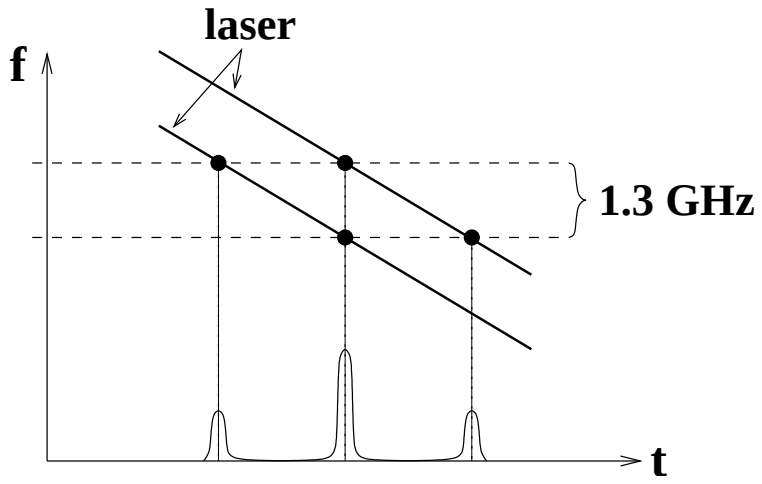


**Figure 2.18:** *The use of a bichromatic light field and two atomic transition frequencies leads to a characteristic three-peak structure during a HV-scan (see text).*

as dashed horizontal lines. Both laser frequencies being scanned show up as diagonal solid lines. Each intersection of both lines corresponds to a fluorescence peak in the spectrum. The resulting plot is shown below and consists of a middle peak and two crossover side peaks. The distance between the peaks corresponds exactly to the hyperfine splitting and is used to calibrate the spectrum. The longitudinal temperature can now be calculated from the $\sigma$-width of the middle peak. Mathematically spoken, the observed profile represents a convolution of the actual velocity distribution with the the Lorentzian-shaped absorption probability of the atomic transition. For a Gaussian velocity distribution, the resulting curve would be a Voigt profile. It turned out that due to the small natural line width in comparison with the Doppler broadening the convolution effects only play a role for very low temperatures ($< 50$ mK) and have been neglected in the temperature measurements presented in this work.

**Pickup measurements**

For a coasting (unbunched) beam it does not make sense to measure the longitudinal spatial ion distribution which would be a constant. However, for a bunched beam separate ion packets (*bunches*) revolve in the storage ring confined by an external potential (see next chapter). At a given location of the ring, one observes a fluctuating ion current due to the separate bunches passing by. The longitudinal ion distribution inside a bunch giving valuable information on the cooling process can be measured with an *electrostatic pickup* device [Albrecht, 1993]. The pickup consists of a short metal tube (length $L = 8\,\mathrm{cm}$) enclosing the ion beam (figure 2.19). A changing ion current influences mirror charge fluctuations which

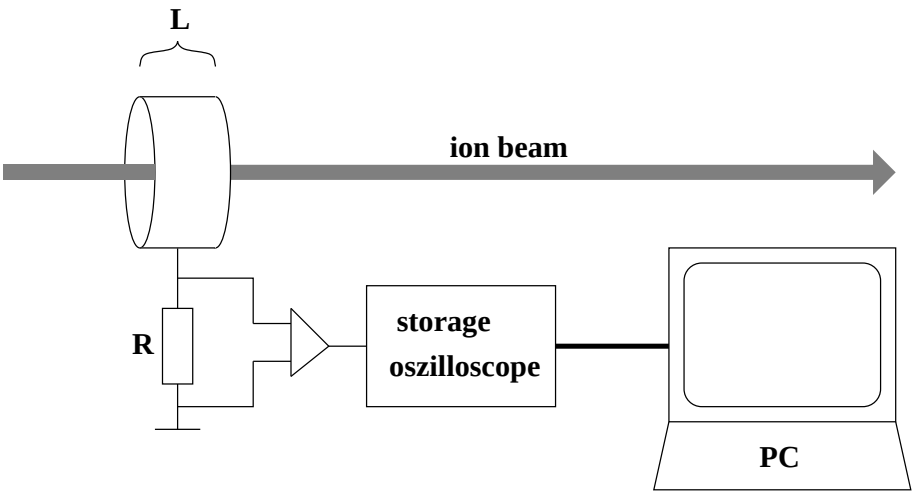


**Figure 2.19:** *Experimental setup of the electrostatic pickup system to measure the longitudinal ion distribution.*

can be measured as a voltage signal over a very large resistor ($R > 2\,\mathrm{M\Omega}$). The charge fluctuations in the metal ring are calculated as

$$\dot{Q} = I_{\mathrm{ion}}(t) - I_{\mathrm{ion}}(t - \Delta t) \approx \dot{I}_{\mathrm{ion}}(t)\Delta t \quad . \tag{2.21}$$

For short times of flight $\Delta t$ through the metal ring (in our case $\Delta t \approx 6\,\mathrm{ns}$) an integration delivers

$$U(t) = \frac{RL}{vC} \cdot I_{\mathrm{ion}}(t) \quad , \tag{2.22}$$

with $C = 120\,\mathrm{pF}$ as the capacitance of the whole system. The spatial ion distribution therefore corresponds to the measured voltage signal in the time domain. The voltage is amplified and fed to a digitizing scope which can be read out by a PC. Since this method is non-destructive the ion distribution can be monitored online

during the cooling process. The pickup device has a electronic high-pass characteristic with a cutoff frequency of $1/RC \approx 50\,\mathrm{kHz}$ (3 dB point). For data analysis, this behavior has to be corrected by performing a Fourier transform and applying an inverse response function to compensate the damping of high frequency components. A subsequent back transform delivers the actual ion distribution. A more detailed description of the correction is given in [Mudrich, 1999].

**Beam profile monitor**

The transverse degree of freedom can be observed with the *beam profile monitor* (BPM) [Hochadel, 1994a]. At a given location of the storage ring it is possible to measure the horizontal and vertical density distribution of the ion beam. From these data one can determine the emittances or transverse temperatures respectively using the known $\beta(s)$ function at this position. For the measurement, one makes use of the restgas atoms in the vacuum pipe that are ionized through collisions with the ion beam. The rate for this process depends on the beam density at a given position. The ionized atoms are accelerated by an electric field ($|\vec{E} = 60\,\mathrm{kV/m}$) towards a micro-channel plate detector where they can be spatially resolved. The measured distribution of restgas ions corresponds to the shape of the beam. At this point, one has to consider that the BPM has a limited spatial resolution due to its function principle. Even for an infinitely narrow ion beam one measures a Gaussian profile with a limited *resolution width* $\sigma_{\mathrm{res}}$, which relies on the fact that the recorded restgas ions have a thermal energy of about room temperature. During the drift from the position of ionization to the micro-channel plate, the thermal motion leads to a smear out of the initial transverse positions. Hence, the measured distribution is a convolution of the actual transverse ion beam profile and the resolution width of the BPM. Since the beam profile of a cooled ion beam also has an almost Gaussian shape, the actual width $\sigma_{\mathrm{ion}}$ can is determined by quadratic subtraction of the measured width $\sigma_{\mathrm{meas}}$ and the resolution ($\sigma^2_{\mathrm{ion}} = \sigma^2_{\mathrm{meas}} - \sigma^2_{\mathrm{res}}$. The resolution width can be determined by extrapolating the BPM measurements of long-term electron cooling measurements [Lauer, 1999]. A typical value for the resolution width is $\sigma_{\mathrm{res}} \approx 0.3\,\mathrm{mm}$. The uncertainty of the transverse temperature resulting from the measurement itself and the subtraction of the resolution width can be estimated with 150 Kelvin.

Due to the good vacuum of $5 \times 10^{-11}$ mbar, the BPM count rate becomes very small especially for low density beams. The count rate could be increase by locally heating the beam pipe around the position of the BPM to about 60° Celsius. This leads to a desorption of particles from the inner surface increasing the number of restgas atoms. One achieves this way an increase of the count rate by a factor of ten. On the other hand, the lifetime of the ion beam is reduced by a factor of two due to the worse the vacuum. However, this reduction is practically no limitation

for the cooling experiments.

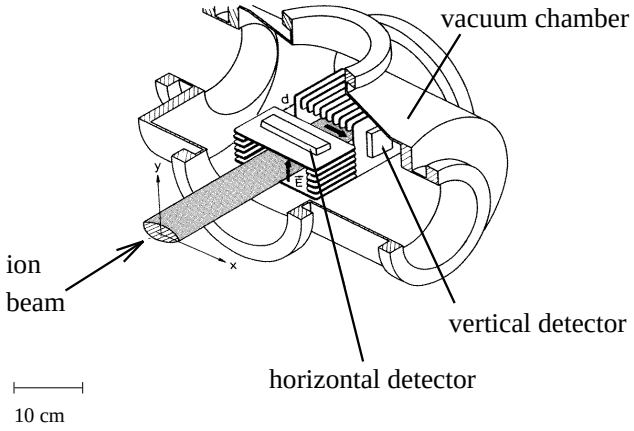


**Figure 2.20:** *Schematic picture of the beam profile monitor (BPM). Restgas atoms ionized by the ion beam are accelerated in an electric field towards a multi-channel plate detector to be spatially resolved.*

Recently, a new magneto-optical trap was install at the storage ring which turned out to be an extremely sensitive target for the ion beam [Luger, 1999, Eike, 1999, Eike et al., 2000]. This device will make it possible to measure low-density beams with much better statistics and an improved spatial resolution.

### Schottky noise analysis

A coasting beam offers an additional possibility for a non-destructive measurement of the longitudinal velocity distribution relying in Schottky noise analysis [Boussard, 1995].

For a single particle circulating in the storage ring (charge $q$, revolution period $T = 1/f$) the beam current, at a given location in the ring, is composed of an infinite train of delta pulses separated in time by $T$ as shown in figure 2.21. In frequency domain, this periodic waveform is represented by a line spectrum, the distance between lines being $f = \omega/2\pi$.

$$A(t) = qf \sum_{n=-\infty}^{+\infty} e^{in\omega t} \tag{2.23}$$

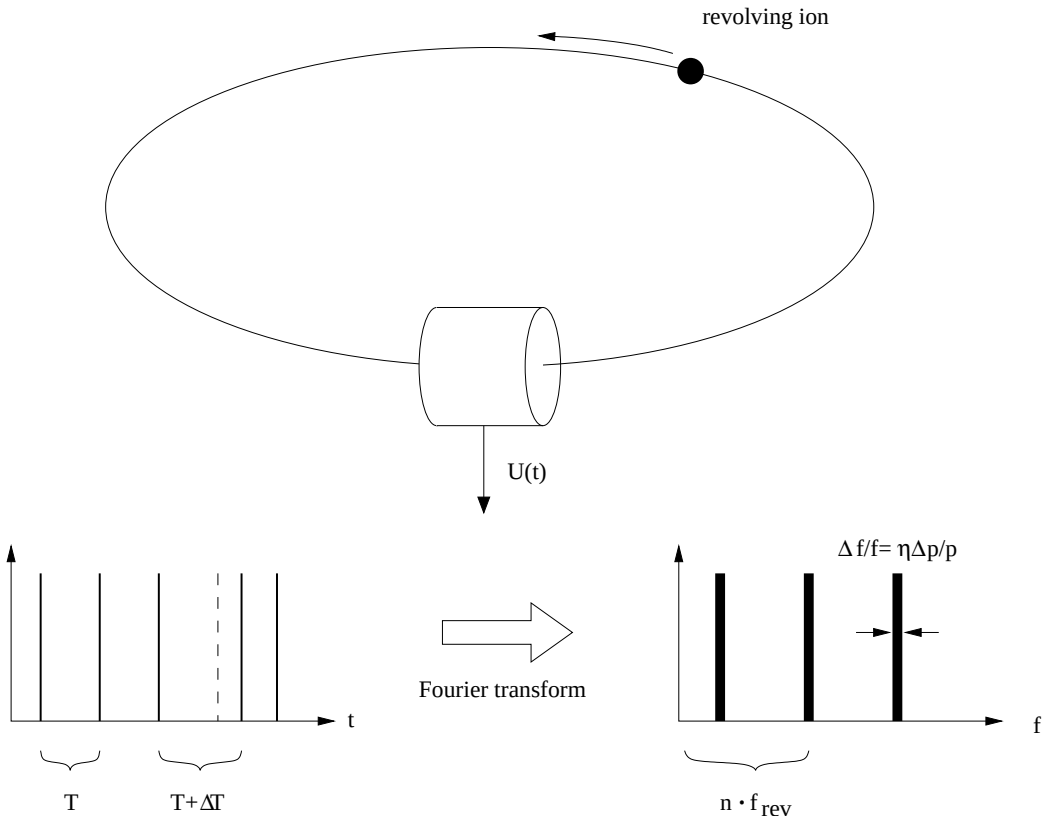


**Figure 2.21:** *Principle of Schottky analysis. One revolving ions produces a series of delta spikes in an electrostatic pickup device reflecting its revolution frequency. An ensemble of ions produces a noise signal. A Fourier transform leads to the distribution of revolution frequencies and therefore the velocity spread of the beam.*

Looking at positive frequencies only:

$$A(t) = qf + 2qf \sum_{n=-\infty}^{+\infty} \cos n\omega t \tag{2.24}$$

For $N$ particles randomly distributed along the ring circumference and moving with different revolution frequencies, each line at frequency $nf$ will be replaced by a frequency band (*Schottky band*) whose width is simply

$$\Delta f = n f_0 \cdot \eta \frac{\Delta p}{p} \quad . \tag{2.25}$$

$f_0$ is the average revolution frequency and $\eta$ the so-called *slip factor*, a machine-specific parameter ($\eta_{\mathrm{TSR}} = 0.985$) [Hofmann and Kalisch, 1996]. Hence, the frequency width is proportional to the relative longitudinal momentum spread $\Delta p/p$

of the ion beam. From the momentum spread one can directly calculate the longitudinal beam temperature. When averaging equation 2.24 over N particles, only the DC terms remain ($A_{\mathrm{DC}} = Nqf_0$), the other components cancel due to the random phase factor. However, the r.m.s current per frequency band which is given by the sum

$$\langle A^2 \rangle = [2qf_0(\cos\theta_1 + \cos\theta_2 + \cdots + \cos\theta_N)]^2 \tag{2.26}$$

does not vanish because of the $\cos\theta^2$ terms. One obtains:

$$A_{\mathrm{rms}} = \sqrt{\langle A^2 \rangle} = 2qf_0\sqrt{N\langle\cos\theta_i\rangle^2} = 2qf_0\sqrt{\frac{N}{2}} \tag{2.27}$$

Thus, the spectral power density $\langle A^2 \rangle$ per frequency band is proportional to the number of ions in the ensemble.

Due to technical reasons (bandwidth limitations of the used amplifier, frequency properties of the pickup device) all experiments used the 15th harmonic of the revolution frequency ($\omega_{15\mathrm{th}} \simeq 3.1\,\mathrm{MHz}$). Note, that Schottky noise analysis can only be used for a coasting beam. In a bunched beam, the revolution frequency of the ion packets lead to a huge peak in the frequency spectrum which makes it almost impossible to derive informations on the longitudinal velocity distribution. However, with this method it is possible to measure the frequency of the ions oscillating in a harmonic bunch potential (synchrotron oscillation) which is described in Appendix A.

### 2.4.4 Time scheme of the cooling procedure

The time for one cooling experiment is typically about 2 to 4 beam lifetimes (50–200 s). During laser cooling the steady state for the longitudinal degree of freedom (direct laser cooling) is reached after roughly 1 ms. Since much lower cooling rates for the transverse cooling process (indirect cooling through collisions and ring dispersion) are achieved, the time for relaxation of these degrees of freedom is in the order of seconds. The longer cooling times are used to observe the influences of the decreasing particle number on the cooling process. Many of the presented diagnostic methods are performed in parallel. Hence, it is possible to get a full picture of the 3D phase-space development during the cooling process. A typical scheme of the experimental timing is shown in figure 2.22. Right after beam injection, the ions are precooled for 6–12 s by the electron cooler from initial temperatures of roughly 20,000 K down to room temperature. During the subsequent actual laser cooling phase the fluorescence count rate is permanently recorded. HV-scans, beam profile and pickup measurements are periodically performed at well-defined times. The repetition rate for the Schottky noise analysis is limited by the time needed for transferring the data to the computer. During

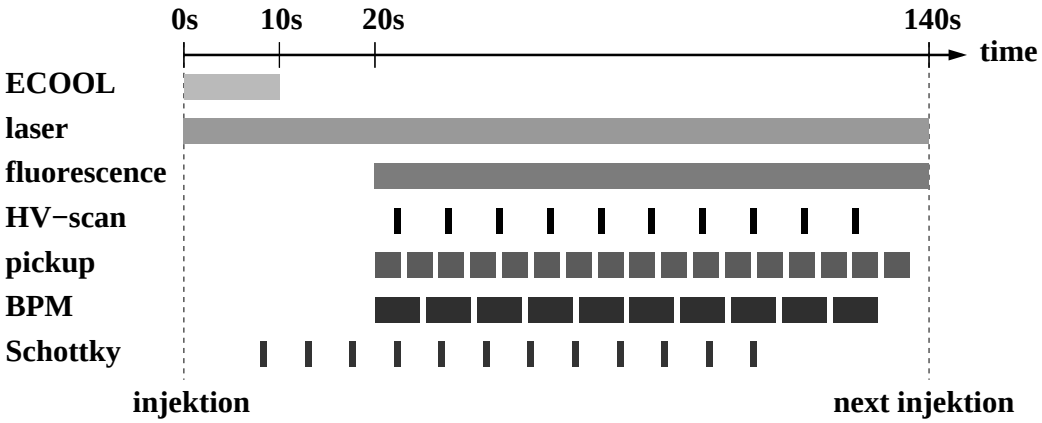


**Figure 2.22:** *Experimental timing during a typical cooling experiment.*

bunched cooling (chapter 3) the radio frequency field was on for the complete measurement cycle. The statistical errors are minimized by averaging over 3–10 injection cycles. Note, that this averaging is not possible for the observation of the anomalous beam behavior as presented in section 3.3. In this case, the beam behavior strongly differs from injection to injection so that averaging does not make any sense.

# Chapter 3

# Anomalous behavior of laser-cooled bunched beams

This chapter investigates laser cooling of bunched beams, where the ions are longitudinally confined by a pseudopotential and its corresponding force counteracts the laser. First experiments of bunched laser cooling using sinusoidal bunch potentials were performed at the ASTRID storage ring [Hangst et al., 1995b]. This cooling scheme was further investigated at TSR [Madert, 1995, Luger, 1996, Miesner et al., 1996a] and extended to efficient three-dimensional cooling using the dispersive cooling method [Lauer et al., 1998].

Here, new systematic measurements on the cooling process in non-sinusoidal bunch potentials are presented. The use of a sinusoidal confining bunch potential leads to an inhomogeneous longitudinal ion density distribution. As described in section 2.2.4 the observation of Coulomb ordering however strongly depends on the ion distance which is not constant in a sinusoidal bunched beam. Therefore, laser cooling was investigated in novel dedicated bunch potentials called *barrier buckets* (section 2.4.2). Experiments were performed in order to examine and compare the cooling dynamics of three different bunch potentials: sinusoidal potential, barrier potential and a pure square-well potential. In addition, newly developed simulations including the effect of hard Coulomb collisions give a very clear picture on the physics of laser cooling of fast ion beams. At very high phase-space densities one observes a sudden change of the beam behavior which clearly shows an abrupt disappearance of intra beam collisions.

## 3.1 Laser cooling of bunched beams

Figure 3.1a) shows the calculated phase-space trajectory of an ion in a barrier bucket experiencing the laser force in a frame moving with the synchronous veloc-

ity. The ion experiences a position-dependent force resulting from beam bunching which plot above the graph. The velocity-dependent laser force is depicted vertically on the right side. During an oscillation cycle, the ion is drawn over the laser resonance. In the case shown, the laser counteract the ion motion. This leads to a damping of the oscillation. The laser therefore acts as a friction force. Note, that during the first oscillation cycles the ion interacts with the laser for very short time. Hence, the damping of the oscillation is small. After several cycles the interaction time becomes gradually longer and longer until the ion is drawn to the synchronous velocity ($\Delta v = 0\,\mathrm{m/s}$) in an over-damped motion. The oscillation can also be driven by the laser force if the ion comes in resonance at positive deviation from the synchronous velocity as shown in figure 3.1b).

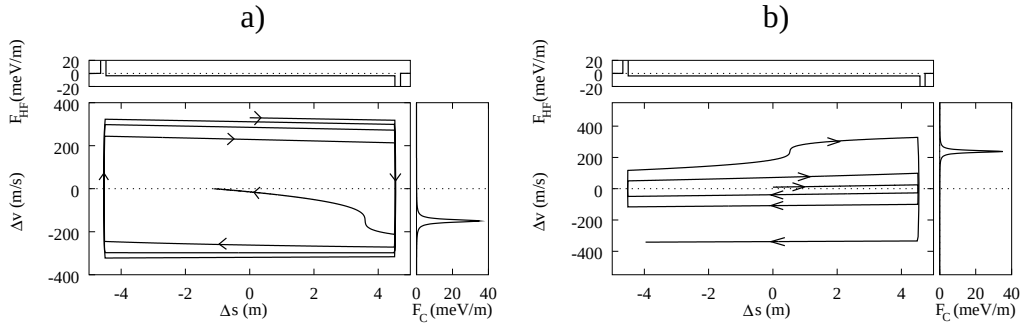


**Figure 3.1:** *Phase-space plots of a bunched ion cooled (a) as well as heated (b) by the laser force.*

Depending on the laser position in velocity space with respect to the ion motion it is possible to either heat or cool the beam longitudinally. Because the experimental setup uses fixed-frequency lasers, the position of the laser with respect to the bucket can be adjusted by changing the synchronous velocity, which depends on the bunching frequency. A shift of the bunching frequency corresponds to a shift of the velocity zero line in the shown phase-space diagrams.

In this system two velocities are defined: the synchronous velocity $v_{\mathrm{synch}}$ defined by the bunching frequency and the "stable velocity" $v_{\mathrm{stable}}$ determined by the equilibrium of the laser force and the counterforce $F_{\mathrm{slope}}$ which is produced by the slope of the barrier bucket (figure 3.2). A mismatch between both velocities leads to an additional constant force $F_{\mathrm{mis}}$ acting on the ion. During the cooling process the ion in this case pushed towards the front or the rear bucket border depending on the sign of the force. In another picture, an ion is cooled to the stable velocity. The bunch potential however moves with the synchronous velocity. Hence in the comoving frame the ion is pushed towards one of the bucket boundaries.

For a set of ions distributed around a velocity one has to use the mean values.

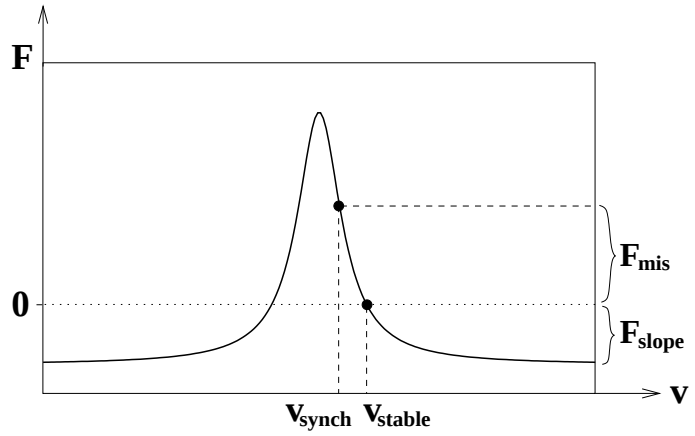


**Figure 3.2:** *A mismatch between the stable velocity $v_{\mathrm{stable}}$ and the synchronous velocity $v_{\mathrm{synch}}$ leads to an additional constant force $F_{\mathrm{mis}}$ acting on the ion.*

Therefore the mean mismatch force acting on the ion ensemble is calculated as

$$\langle F_{\mathrm{mis}} \rangle = \alpha \cdot \langle v_{\mathrm{stable}} \rangle - v_{\mathrm{synch}} \quad , \tag{3.1}$$

with the friction coefficient $\alpha$. In the experiments the mismatch force leading to inhomogeneous longitudinal ion distributions can be avoided by adjusting the bunching frequency, so that the synchronous velocity exactly matches the stable velocity.

## 3.2 Systematic measurements & comparison with simulations

### 3.2.1 Longitudinal dynamics: observations

To introduce the concepts of laser cooling in bunched beams, we first show some typical results. The experiments presented here were done with barrier buckets. The experiments were performed at a laser power of $P \simeq 90\,\mathrm{mW}$ at a laser beam waist of $w_0 \approx 1.7\,\mathrm{mm}$. For optimum dispersive cooling of the transverse degrees of freedom a relative ion-laser beam offset of $\Delta x = 600\,\mu\mathrm{m}$ was chosen. Beam bunching was done at the third harmonic of the ion revolution frequency ($\nu_{\mathrm{rf}} = 676\,\mathrm{kHz}$). The detuning of the bunching frequency with respect to the laser velocity was $\delta\nu = 4\,\mathrm{Hz}$ which turned out to be the optimum values to achieve efficient longitudinal cooling.

As described in chapter 2 the longitudinal velocity distribution is measured with the HV-scan method. A typical picture is shown in figure 3.3 (very left plot).

The velocity distribution shows the typical three-peak structure due to the hyperfine splitting as explained in 2.4. Theoretically this structure could be deconvolved in two steps. In the first step the spectrum is corrected considering the bichromatic

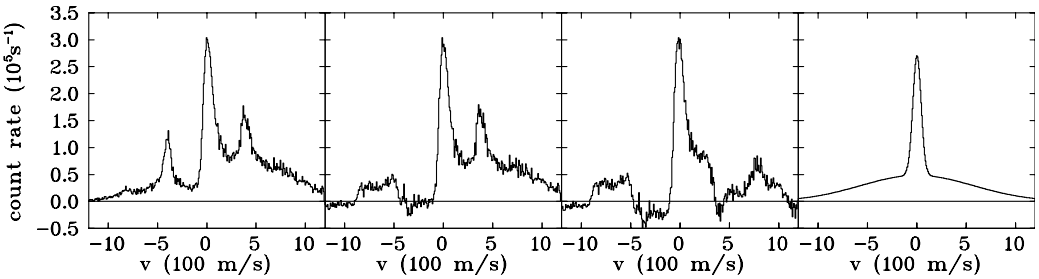


**Figure 3.3:** *The measured HV-scan is deconvolved in two steps. Since this process is numerically unstable the data has been fit by a et Gaussian functions. The actual velocity distribution derived this way is shown in the very right plot.*

laser field with the values of the laser frequency widths and their relative detuning. This leads to a two-peak structure (second plot) reflecting the two hyperfine ground states of Beryllium. A second deconvolution with the atomic three-level scheme then leads to the actual longitudinal velocity distribution of the ion ensemble (third plot). However it turned out that the two step deconvolution process carried out with experimental noisy data sets is numerically rather unstable. Even slight differences between the experimental and the assumed laser detuning for example leads to an oscillation in the resulting profile. This can also be observed in the presented calculation. The determination as well as an analysis of the distribution shape is therefore almost impossible. To avoid these problems the original data was fit with a sum of six Gaussian distributions. For the fit procedure certain parameters such as the position of the peaks are kept fixed. In addition, the width of each peak should give the same velocity spread. These restrictions improve the numerical stability of the fit. From the result the actual velocity distribution can be derived (figure 3.3, very right plot)

Figure 3.4 shows the longitudinal velocity distribution measured with the HV-Scan method as well as the corresponding spatial ion distribution in the bunching potential observed with the electrostatic pickup. The data on the right side corresponds to the same cooling conditions as on but with the use of the capture range extension (see section 2.3). The plot shows the ion distribution 5 seconds after starting laser cooling. From this plot one extracts a characteristic two-component distribution: The velocity ensemble consists of a narrow and peak with a width on the order of 10 m/s as well as a broad pedestal covering a velocity range of about 1000 m/s. In addition, one notices an asymmetry of the peak. The peak shows a sharp edge on the left and a smoother decrease on the right side. The use of

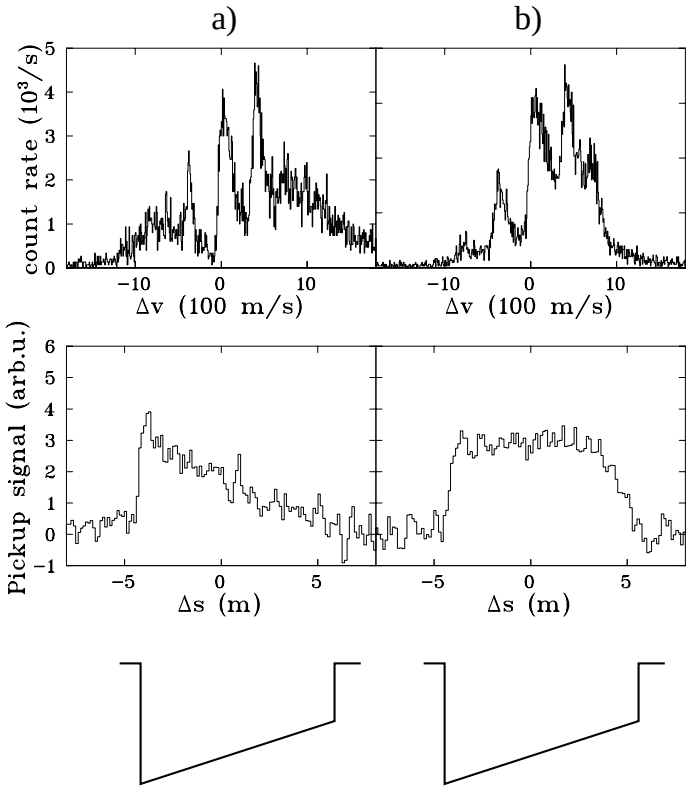


**Figure 3.4:** *Laser-cooled velocity and spatial distributions without (a) and with (b) the capture range extension.*

the capture range extension significantly changes the shape of the velocity distribution (right plot). As described in section 2.3 the capture range extension also leads to an excitation of ions not being at the resonance velocity of the cooling laser. Therefore mainly the shape of the broad pedestal of ions not in resonance with the laser is modified. The use of the capture range extension leads to a compression of the ion background. Ions apart from the stable point in velocity point are more efficiently drawn to the laser resonance. The velocity width of the peak is almost unchanged. The temperature derived from the velocity spread of the peak is $T_{||} \approx 1\,\mathrm{K}$ without and $T_{||} \approx 1.5\,\mathrm{K}$ with the capture range extension.

The lower row of figure 3.4 shows the spatial longitudinal ion distribution in the barrier bunch potential, which is sketched below the plot. Without the capture range extension one observes an increase of the ion density at the left side of the bunching potential. For the ions sitting at the left bucket border the laser force is obviously not strong enough to compensate the counterforce produced by the potential slope. This is the case for ions being part of the pedestal of the velocity distribution since these ions are not in resonance with the laser. In the right picture

measured with the capture range extension one observes an almost constant ion distribution. The extended laser force in velocity space leads to the situation that also ions apart from the stable point experience a notable laser force. The ion ensemble stands in equilibrium with the counterforce produced by the bunching potential. Therefore, the resulting ion distribution is balanced.

### 3.2.2 Longitudinal dynamics: model

In order to get a further insight into the ion dynamics and to model the observed effects, a computer simulation program was written which calculates the ion trajectories in longitudinal phase space. It numerically solves the equation of motion for arbitrary pseudopotentials and velocity-dependent forces. The repeated calculation of the single-particle motion beginning with a set of different starting conditions allows the simulation of the phase-space evolution of an ion ensemble. The influence of the transverse-longitudinal coupling is taken into account using a Monte-Carlo approach.

Considering only the longitudinal motion of the ions one has to solve Newtons's equation of motion

$$m\ddot{s} = F_{\mathrm{rf}}(s) + F_{\mathrm{las}}(\dot{s}) \tag{3.2}$$

($m$: ion mass, $s$: longitudinal coordinate along the bunch potential). The force $F_{\mathrm{rf}}$ produced by beam bunching and the laser force $F_{\mathrm{las}}$ are defined in equation. 2.18 and 2.17 respectively. The above equation represents a second-order non-linear ordinary differential equation (ODE) which has no analytical solution for arbitrary bunching potentials. The computer code uses the Runge-Kutta method with adaptive step width [Press et al., 1992]. The computation accuracy can be controlled by a parameter $\epsilon$ defining the average step width. The value of $\epsilon$ was optimized, so that the relative deviation of the total energy after one second of integration time was below 1%. This values turned out to be a good trade-off between accuracy and calculation time.

The effect of intra beam scattering (see section 2.2.2) has been included by a Monte-Carlo model. In particular, the influence of hard Coulomb collisions with large velocity changes during the scattering process has to be considered due to the small capture range of the laser cooling force (see 2.3). During the calculation of a single-particle trajectory the time for the occurrence of a scattering process is randomly determined assuming a given constant scattering rate $r$ which is a free parameter in the simulation. A scattering process changes the longitudinal velocity of the particle by $\delta v$. $\delta v$ is again randomly determined according to a given probability function $W(\delta v)$. For the probability function we

set [Miesner, 1995, Lauer, 1999]

$$W(\delta v) = \begin{cases} \left|\frac{\delta v_{\mathrm{cut}}^2}{\delta v^3}\right| & : \quad |\delta v| > \delta v_{\mathrm{cut}} \\ 0 & : \quad \mathrm{otherwise} \end{cases} \tag{3.3}$$

with the cutoff velocity $\delta v_{\mathrm{cut}}$ which is needed to normalize the distribution function. It is the second free parameter of this model. This relation results from the theory of binary collisions based on Rutherford's scattering formula. In [Miesner, 1995] the probability for a collision outside the capture range $v_c$ was calculated as $W \propto 1/v_c^2$. A differentiation delivers $W(\delta v) \propto 1/\delta v^3$. A plot of the probability function 3.3 is shown in figure 3.5. This model neglects colli-

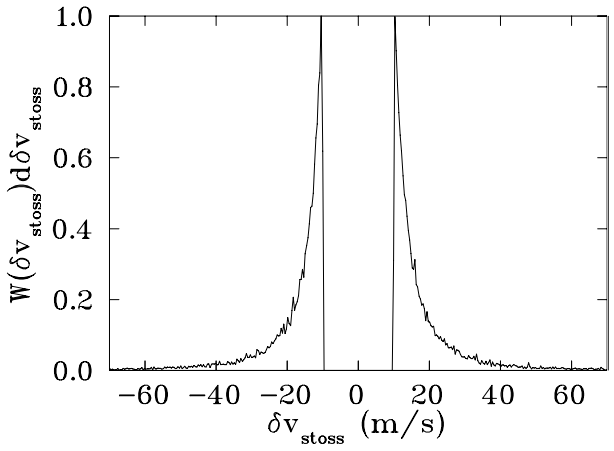


**Figure 3.5:** *Plot of the probability function $W(\delta v)$ used for determining the longitudinal velocity change after a simulated collision.*

sions with small energy transfers which would correspond to a diffusion process. This assumption is valid due to the fact that only the hard Coulomb collisions notably contribute to the heating rate because of the small capture range. Ions that have undergone velocity changes smaller than the capture range are immediately cooled back. The cutoff velocity in this simulation is set to $\delta v_{\mathrm{cut}} = 10\,\mathrm{m/s}$ which is smaller than the velocity spread of the laser force.

Typical phase-space trajectories of a single laser-cooled ion are shown in figure 3.6. The plots show the cooling dynamics for a barrier potential. The left plot shows the particle motion without collisions. The right plot demonstrated the influence of collisions using the model described above. Without any collisions, the ion is drawn to the synchronous velocity sitting at the right bucket wall. The presence of scattering processes leads to a permanent change of the ion velocity either within or outside the capture range. In the first case the is immediately

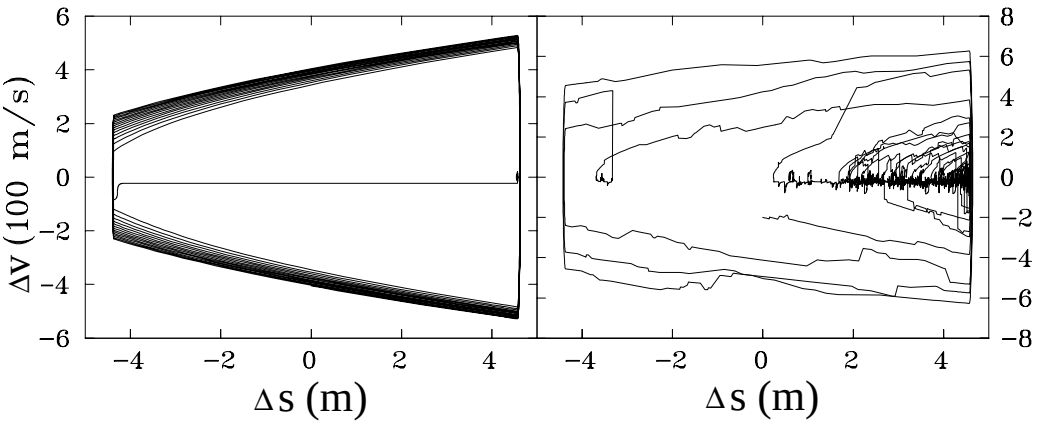


**Figure 3.6:** *Simulated trajectories without (a) and with (b) collisions.*

drawn back to the stable point in an over-damped motion. In the latter case the ion starts oscillation again and it takes several cycles to reach the stable velocity.

These two types of motion (oscillating and over-damped) are the reason for the experimentally observed two-component distribution in velocity space: the cold peak corresponds to the particles within the capture range of the cooling force. The hot pedestal consists of ions that have undergone a hard Coulomb collision out of the capture range and are now oscillating again. The process of cooling back these ions takes several oscillation cycles so that one always has a subensemble of hot ions underlying the cold ensemble being at the stable point of the cooling force. Furthermore, one can say that the presence of a hot background is a clear signature for the existence of hard Coulomb collisions in the ion beam. In steady state, the ratio of the number of ions in the hot and the cold fraction is thereby determined by the scattering rate and the cooling rate of the laser. The scattering rate thereby depends on the 3D ion density. The cooling rate is determined by several experimental parameters: potential shape and depth, bunching frequency and the laser intensity. Since all these parameters can directly be measured the two remaining parameters of the simulation (cutoff frequency $\delta v_{\mathrm{cut}}$ & scattering rate $r$) have been fitted to match the experimental data.

The computer model also simulates the influence of the capture range extension. For this purpose, the laser force profile is modified accordingly to figure 2.9. This modified cooling force also acts on ions not being at the stable point. Therefore, scattered ions that oscillate in the bucket can be faster cooled back. In steady state, this leads to a compression and a reduction of the hot pedestal.

### 3.2.3 Longitudinal dynamics: comparison of bunch forms

Furthermore, we investigated the influence of different potential shapes on the cooling dynamics. Figure 3.7 shows ion distributions in longitudinal velocity and real space that are cooled in the bunching potentials schematically depicted above the data.

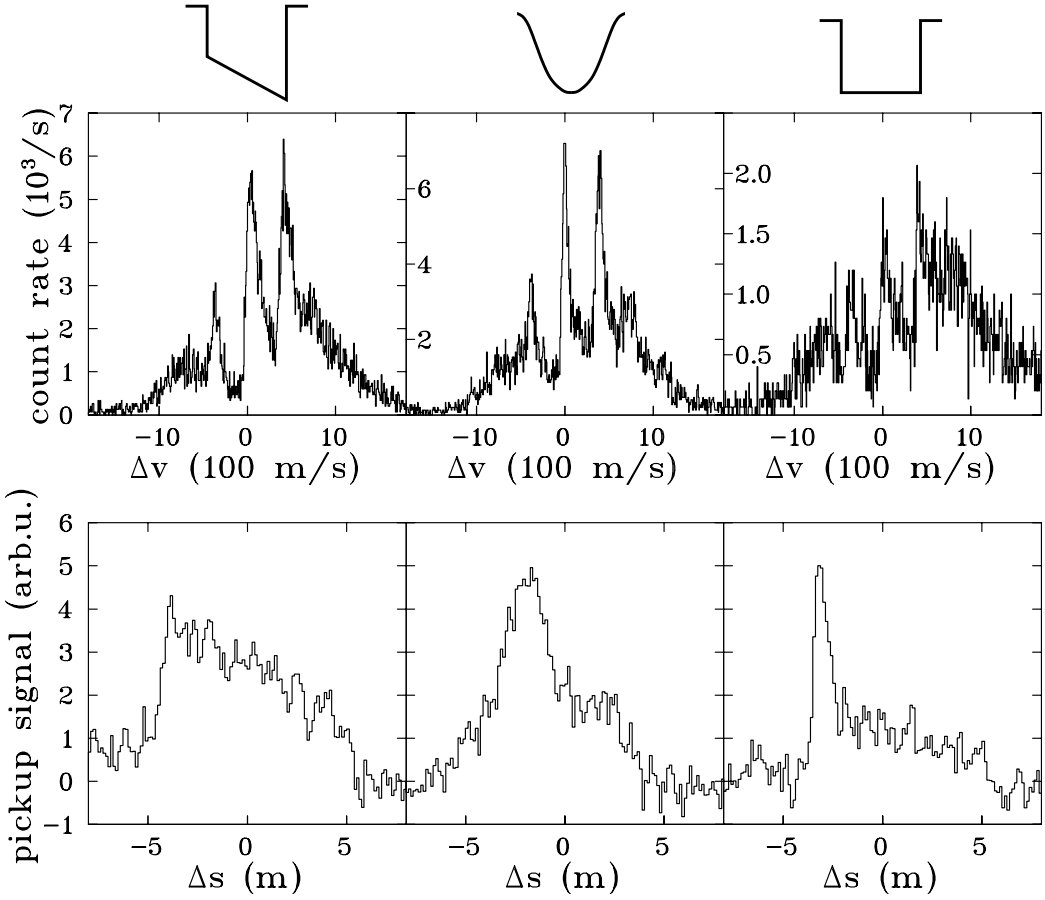


**Figure 3.7:** *Experimental ion distribution in different bunch potentials.*

For the sinusoidal potential the cold peaks are narrower than for the barrier bucket which indicates a better cooling in the sinusoidal potential. In case of the pure square-well bucket the peaks are hard to distinguish from the broad pedestal. The spatial ion distribution in the barrier bucket is homogeneous but slightly shifted to the left potential wall. This is the result from a misadjustment of the potential slope with respect to the laser force. For the square-well potential the ions are pushed against the potential wall. In addition one measures a second set of ions almost homogeneously distributed along the bunch. The maximum ion

distribution in the sinusoidal potential is markedly shifted to the left. In addition, the ion distribution shows a characteristic "shoulder" located near the center of the potential.

Although the longitudinal velocity distribution of a laser-cooled ion beam is not in thermal equilibrium it turned out that the spatial distribution $n(s)$ of an ion ensemble (longitudinal temperature $T_{\|}$) in an external potential $V_{\mathrm{ext}}(s)$ is described by Boltzmann's law

$$n(s) = n_0 \cdot e^{-\frac{V_{\mathrm{ext}}(s)}{k_{\mathrm{B}} T_{\|}}} \quad . \tag{3.4}$$

Since a temperature in a thermodynamical sense is only defined for an ion ensemble being in thermal equilibrium one has to put in the temperature definition given in section 2.2.

A potential slope $V_{\mathrm{ext}}(s) = F_{\mathrm{slope}} s$ given by the barrier potential therefore leads to an exponential distribution

$$n(s) = n_0 \cdot e^{-\frac{F_{\mathrm{slope}} s}{k_{\mathrm{B}} T_{\|}}} \quad . \tag{3.5}$$

As mentioned above, for an exact equilibrium between $F_{\mathrm{slope}}$ and $F_{\mathrm{laser}}$ ions inside the bunching potential experience no net forces. The effective external potential becomes constant ($V_{\mathrm{ext}}(s) = V_0$). The ions are therefore homogeneously distributed in the bunch.

$$n(s) = n_0 \cdot e^{-\frac{V_0}{k_{\mathrm{B}} T_{\|}}} \quad . \tag{3.6}$$

A sinusoidal potential which can be approximated by a parabola $V_{\mathrm{ext}}(s) = Ds^2$ for small oscillation amplitudes thus gives a Gaussian distribution

$$n(s) = n_0 \cdot e^{-\frac{Ds^2}{k_{\mathrm{B}} T_{\|}}} \quad . \tag{3.7}$$

One has to bear in mind that this description can only be an approximation due to the obviously invalid assumption of having an ion ensemble being in thermal equilibrium. In particular the effect of a two component distribution leads to notable deviations from the theoretically expected density distributions. It is possible to extend the description assuming that the measured distribution is a superposition of two ensembles (a hot and a cold one) with different force conditions. While the background ensemble only experiences the forces produced by the bunching potential the cold ensemble also interacts with the laser force. In addition the effect of space-charge is neglected. An extension of this model would also be possible leading to a Debye-Hückel approach [Fowler and Guggenheim, 1956, Eisenbarth, 1998].

A full understanding of the experimental observations is possible with the use of the computer model. Responsible for the different cooling dynamics is the

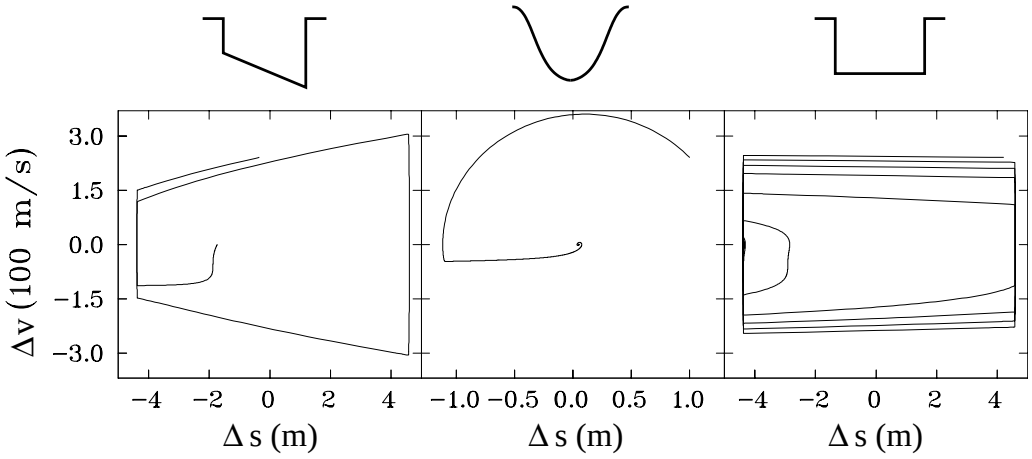


**Figure 3.8:** *Simulated cooling trajectories in different bunch potentials: barrier bucket (left), sinusoidal bucket (middle) and square-well potential (right). The plots show the trajectories for equal simulation times.*

characteristic motion of a particle in the bunching potentials as simulated in figure 3.8. The simulation time for the three pseudopotentials as well as the laser position in velocity space were the same. Also the starting velocities of the ions were equal. The middle plot shows the situation for a sinusoidal-bunched beam. Under these conditions, the ion is drawn to the stable point after less than one synchrotron cycle. The stable point in real space is slightly shifted with respect to the potential minimum. At this point, the counterforce is in equilibrium with the laser force. For the pure square-well potential, the ion performs several oscillation cycles until the stable point is reached. Since there is no counterforce present inside the bucket, the ion is pushed against the left bucket border. The motion of the barrier bucket lies in between the described cases. The final spatial position of the ion depends on the start parameters (velocity and position). Since there is no longitudinal position preferred, an ion ensemble will be homogeneously distributed in the potential. Experimentally, one observes a biasing of the spatial distribution towards the left bucket border. The comes from a misadjustment of the bunching frequency which defines the synchronous velocity of the ions and the stable velocity determined by the laser force and the potential slope.

The cooling dynamics in the three potential shapes therefore mainly differs in the time needed to cool an ion to the stable point. The time for cooling back an ion is determined by the average time an ion being resonant with the cooling laser while oscillating in the bucket. The sinusoidal potential steadily changes the ion velocity. In contrast, the ideal square-well potential would only change the

direction of motion while being reflected at the bucket wall. The very short time when the ion becomes resonant with the laser leads to a weak damping.

The different times needed to cool ions to the stable point explain the ratio of hot and cold ions in the two-component distribution. The recycling of ions that have undergone a Coulomb collision in a square-well potential therefore takes a long time. In steady state, the hot fraction is comparably large. With respect to the shorter time needed to recool scattered ions in the sinusoidal bucket, the hot fraction is in this case much smaller. The number of hot ions in the barrier bucket lies in between. A simulation of a particle ensemble including collisions as described above is shown in figure 3.9. The used parameters correspond to the experimental conditions leading to the distributions shown in figure 3.7.

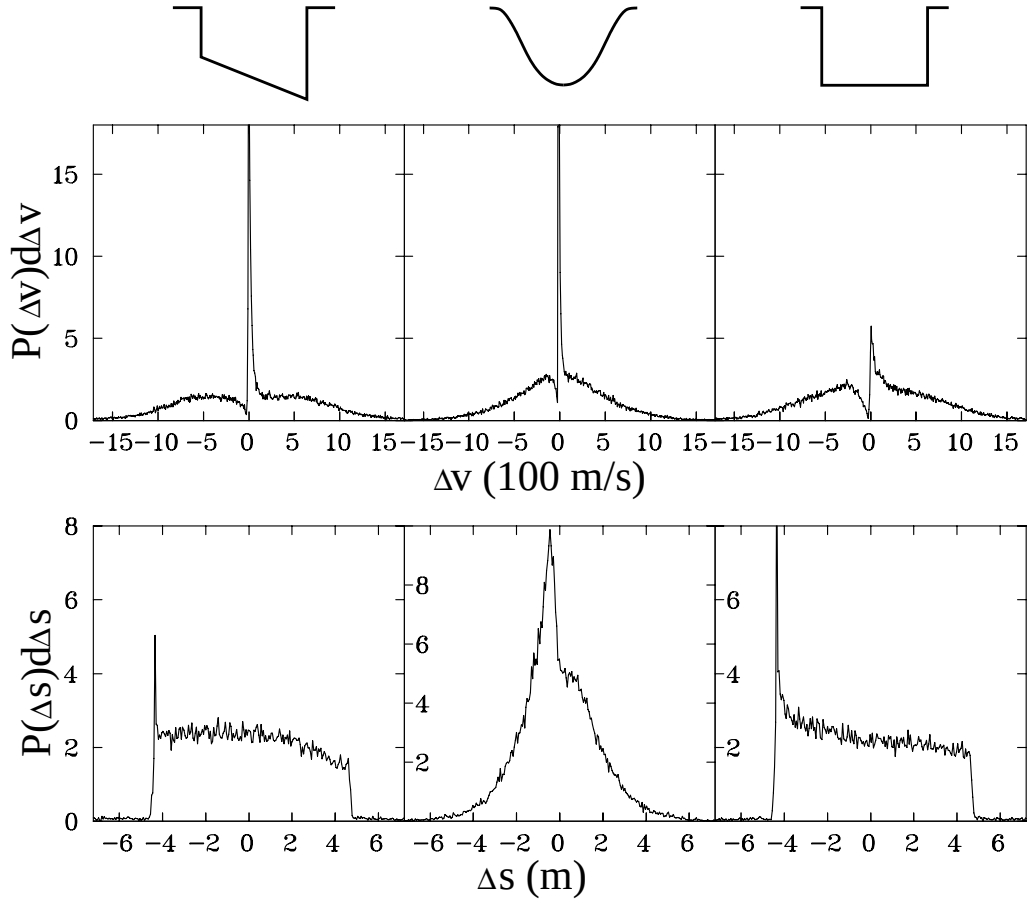


**Figure 3.9:** *Simulated distributions of laser-cooled ions in different bunch potentials. The simulation parameters correspond to the experimental conditions in figure 3.7.*

The simulation results agree qualitatively with the experimental data. Since

the simulation considers an optical two-level system and only one laser frequency, the calculated profiles reflect the actual velocity distribution and do not show the three-peak structure resulting from the HV-scan. One clearly observes the two-component structure. Also the asymmetry of the cold peak is visible. The spatial distribution matches the main features of the experimental data but there are some differences. The simulation also shows a two-component distribution in real space. This comes from the fact that the hot and the cold subensemble experience different forces. The hot ions are not in resonance with the laser. Hence, these ions only experience the forces produced by the bunch potential. This leads to a constant distribution in case of the square-well potential and a Gaussian shape for the sinusoidal bucket, which is visible in the plots. The cold distribution being in resonance with the laser also experiences the light pressure force. Hence, these ions are pushed to the bucket wall in the rectangular waveform and pushed slightly out of the potential minimum of the sinusoidal bucket. The sum of both distributions lead to the described density profiles.

The barrier bucket and the square-well potential show distributions with very sharp peaks in the longitudinal ion density. The experimental distributions are much broader. This may rely on the complete neglect of inter-particle effects such as space charge. The repulsive mutual Coulomb interaction of the ions would smear out these high ion densities.

The evolution of longitudinal phase space was measured over four beam lifetimes to study the long-term dynamics of a laser cooled ion beam. In figure. 3.10 one can compare the temperatures of the cold fraction as well as the ratio of the cold fraction and the total ion number with respect to the cooling time. This has again been measured for the three bunch potentials with and without the capture range extension. While the temperatures for each data set show almost no change during the cooling process, the fraction of ions in the cold section with respect to the total ion number steadily increases. The decreasing ion number leads to a decreasing IBS rate which is responsible for the existence of the hot background ensemble. Hence, the size of the hot fraction steadily shrinks. It turns out, that the largest cold fraction is achieved using the sinusoidal bunch potential which leads to the best recycling rate as shown above. The sinusoidal bunch also leads to the lowest temperatures of about one Kelvin. The temperatures for the barrier buckets are slightly above. For the rectangular waveform, the temperature measurement has a huge uncertainty since it is hard to distinguish between the cold fraction and the background (see figure 3.7).

### 3.2.4 Transverse dynamics

The transverse beam temperatures were determined using the beam profile monitor. A Gaussian fit on the horizontal beam profiles together with the storage ring

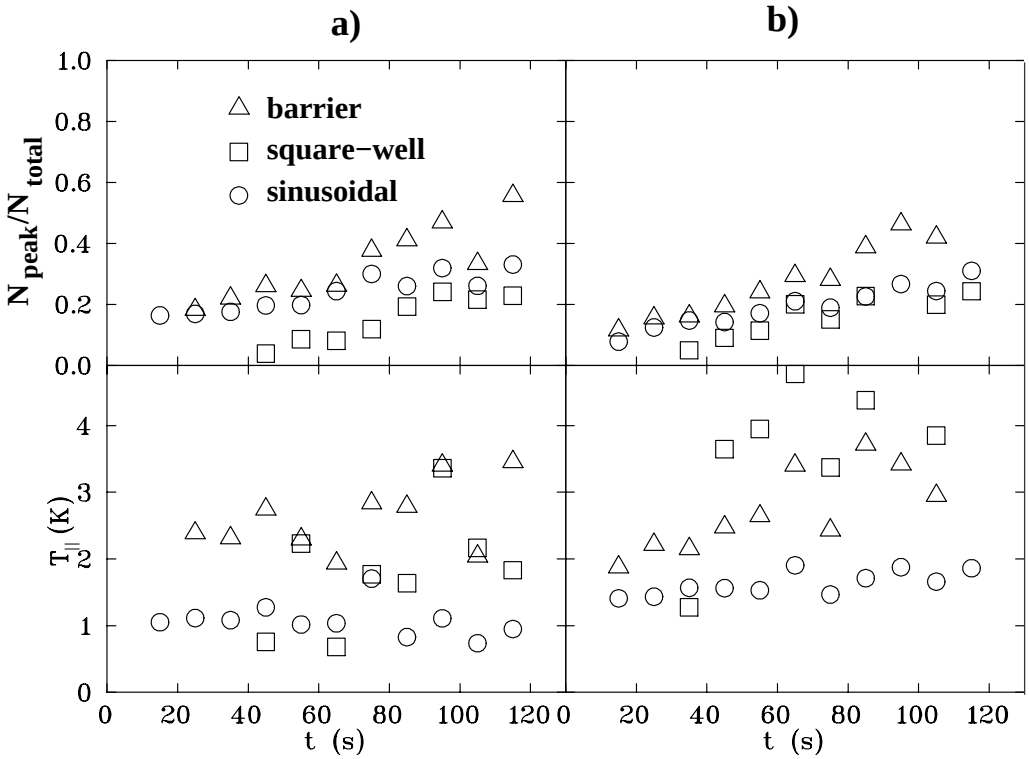


**Figure 3.10:** *Time evolution of laser-cooled ion beam under various cooling conditions: The first row shows the fraction of hot ions from the total ion number. The second row depicts the longitudinal temperatures of the cold fraction.*

function $\beta$ at the position of the BPM allows the calculation of the beam emittance or the temperature respectively. Figure 3.11 shows the time evolution of the horizontal beam temperatures for the same experimental conditions as discussed above. The vertical temperatures are exactly equal due a well-adjusted betatron coupling. Therefore, we will only consider the horizontal degree of freedom. Each data point was taken at the same time where a measurement of the longitudinal temperature was made in figure 3.10. Due to the low ion beam current, the count rates of the BPM are very small. This leads to a comparably large scattering of the transverse temperature data. Without the capture range extension (left diagram) the temperatures of the sinusoidal and the barrier bucket are almost the same. Starting at $T_\perp \approx 600\,\mathrm{K}$ the transverse temperatures steadily decrease to $T_\perp \approx 200\,\mathrm{K}$ after four beam lifetimes. This again results from the decreasing heating rate due to IBS with a decreasing beam current. The pure square-well potential shows significantly higher temperatures of more the $T_\perp \approx 700\,\mathrm{K}$ due to a much lower longitudinal cooling rate. The use of the capture range range ex-

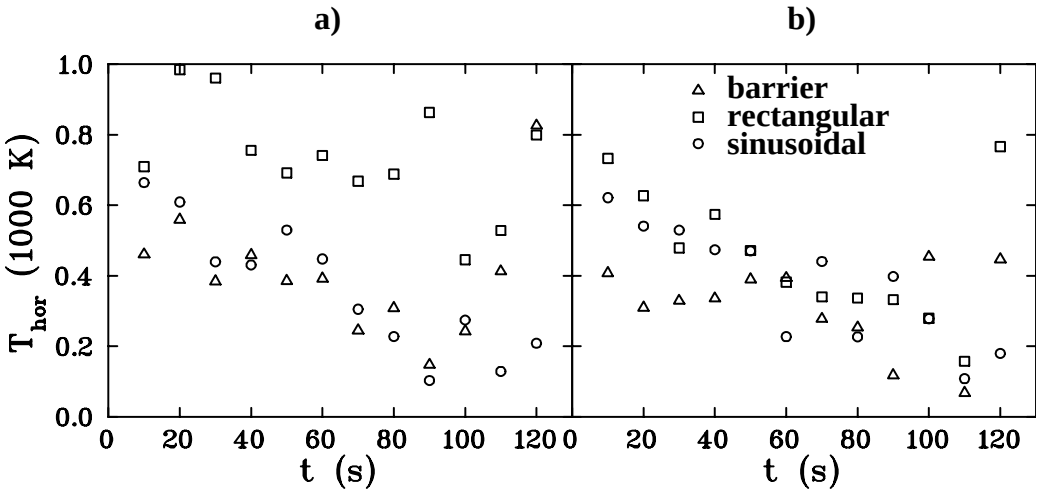


**Figure 3.11:** *Time evolution of the horizontal beam temperatures during the laser cooling process in different bunch potentials with and without the capture range extension.*

tension (right diagram) has only little influence on the sinusoidal and the barrier bucket data. However, the temperatures for square-well potential are noticeably lower. As already seen for the longitudinal degree of freedom, due to the poor recycling of hot background ions in the square-well potential the capture range extension has a strong influence on the overall longitudinal velocity spread. A smaller longitudinal velocity spread acts as a better heat sink for the transverse degree of freedom while cooling through collisions.

As a result of the systematic measurements one can say that the sinusoidal and the barrier bunch potentials give the best results for efficient laser cooling of a bunched beam. In view of the observation of Coulomb ordering, the barrier bucket generating constant longitudinal density distributions would be preferred.

## 3.3 Anomalous beam behavior at extreme phase-space densities

During laser cooling in a barrier bunched beam and carefully optimized cooling conditions we observed a dramatic change in the beam dynamics. For a dilute ion beam, we measured a sudden disappearance of hot background ions accompanied be a drop in the longitudinal temperature [Eisenbarth et al., 2000b]. This effect has been first observed during a beam time in November ’98 and could be reproduced in several succeeding measurement sessions.

For the measurements we injected a small beam current of $I_{\mathrm{ion}} \approx 30\,\mathrm{nA}$ which corresponds to $10^6$ stored ions in total. For beam bunching we used our "standard" conditions: The bunching frequency $\nu_{\mathrm{rf}} = 676\,\mathrm{kHz}$ corresponding to the third harmonic of the revolution frequency. The applied rf voltage was $32\,\mathrm{V}_{rmpp}$ corresponding to a bucket acceptance of 1300 m/s. The voltage slope of 12 V along the bucket length leads to a counter force of $F_{\mathrm{slope}} =$ meV/m. The waist of the laser beam was $w_0 = 1.8\,\mathrm{mm}$ with the focus exactly in the middle of the cooling section of the storage ring. A relative horizontal displacement of 400 $\mu$m ring outwards with respect to the ion beam leads to weak dispersive cooling. The capture range extension was permanently in use. The detuning of the bunching frequency $\delta\nu$ has been varied within $\pm 1\,\mathrm{Hz}$ around $\delta\nu = 0$. This variation is in the same order as fluctuations of the revolution frequency produced by drifts of the storage ring itself. The occurrence of the abrupt change in the beam behavior was extremely sensitive to changes in the bunching frequency. A negative detuning directly leads to a longitudinal heating of the beam and a positive detuning apart from the optimum significantly lowers the cooling rate. So, the effect presented here is a fragile phenomenon but a reproducible one.

### 3.3.1 Longitudinal dynamics

A very dramatic example for the sudden anomalous behavior is depicted in figure 3.12 monitoring the temporal evolution of the fluorescence count rates over more than five beam lifetimes. The fluorescence rate is measured with two photomultipliers located at separate drift tube sets (see figure 2.17). The first photomultiplier $F_1$ measures the fluorescence light around a grounded drift tube set. Therefore, the count rate corresponds to the number of ions being directly in resonance with the cooling laser (upper plot). This also corresponds to the number of ions in the cold fraction of the longitudinal two-component distribution. The second photomultiplier $F_2$ is located at the drift tube set which realizes the capture range extension by repeatedly accelerating and decelerating the ions (middle plot). This leads to the broadband excitation of ions outside the laser resonance. The count rate measured with this photomultiplier thus corresponds to the number of ions being part of the hot fraction in longitudinal velocity space.

During the first 90 s the fluorescence rates exponentially decrease which relies on the decreasing ion current due to collisions with restgas atoms. After 90 s one observes a sudden increase of the fluorescence signal in $F_1$ accompanied by a drop of the count rate in $F_2$ down to stray light level. Subsequent drops in the $F_1$ signals synchronously go with an increase in $F_2$, which points to a time correlation between both signals. The weighted sum of both signals $F_{\mathrm{sum}} = F_1 + \alpha F_2$ is depicted in the lower plot. The weighting results from the different scaling between fluorescence count rate and the corresponding number of ions. The sum

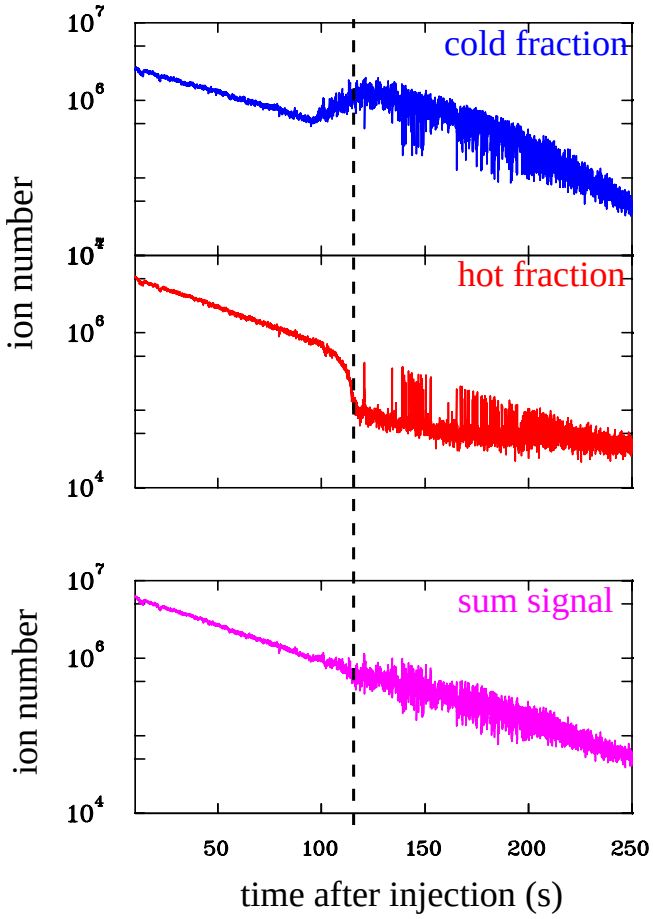


**Figure 3.12:** *Time evolution of the fluorescence signals measured with photomultiplier 1 (upper graph) and 2 (middle graph). The lower plot shows the weighted sum of both.*

signal clearly shows, that the fluctuations seen in one photomultiplier are exactly compensated by the other one. The resulting curve shows an almost perfect exponential decrease. The time constant of $\tau = 45\,\mathrm{s}$ matches the beam life time that has been verified measuring the integral count rate of the BPM. The remaining slight increase in the noise of the sum data after 100 s relies on the measurement process. The fluorescence counts are measured in discrete time bins. The noise comes from the statistical rate fluctuations within one bin due to the low total count rate.

The exponential decay with a time constant of the beam lifetime obviously excludes a loss of ions with the occurrence of the phenomenon. One can also rule out losses due to an extreme dispersive transverse heating which would lead

to a strong decrease of both fluorescence signals. Hence, the transition after 90 s leads to an abrupt transfer of ions formerly in the hot subensemble into the cold fraction. This effect must be explained with a more efficient longitudinal cooling. This can either be caused by an increased cooling rate or a greatly diminished heating rate. Both effects indicate a sudden disappearance of intra beam Coulomb scattering. In particular, the absence of hard Coulomb collisions suppresses the transfer of cold ions into the hot background. In addition, the velocity spread of the remaining cold ensemble becomes that narrow that all ion become resonant with the cooling laser for a bunch frequency detuning near $\delta\nu \approx 0$. This leads to the maximum cooling rate achievable in this system.

The drawn conclusions are confirmed by the measurement of the longitudinal velocity distribution using HV-scans depicted in figure 3.13. The experimental

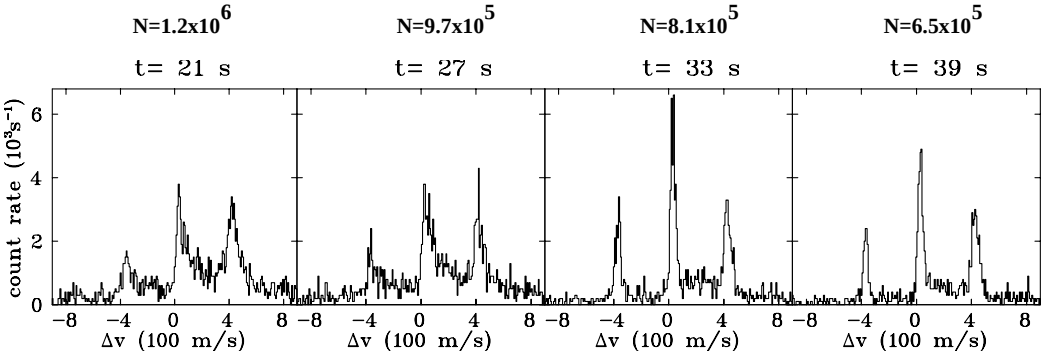


**Figure 3.13:** *Longitudinal velocity distribution measured before and after the transition. One observes a disappearance of the hot background after 27 s and a reduction of the velocity spread in the cold fraction.*

conditions were the same except the number of ions during injection. This leads to the observation of the effect already after $t \approx 27$ s. However, the estimated total ion number of roughly $10^6$ at the time of the transition corresponds to the first observation. One notices a sudden disappearance of the hot background accompanied by an obvious shrinking of the cold velocity width reaching the apparative resolution limit.

For a further analysis, the HV-Scan data has been fitted using a sum function of six Gaussian distributions. For each peak one assumes a superpositions of a narrow Gaussian peak and a broad one to model the two-component distribution. Since the intermediate distance of the peaks corresponds to the known hyperfine splitting, the positions are kept constant during the fitting process, which reduces the set of variation parameters. From the fitted data one calculates the ratio of hot ions with respect to the total ion number (figure 3.14). The width of the cold subensemble was used to determine the longitudinal temperatures.

The relatively poor counting statistics and the complex fitting procedure contributes to an estimated statistical and systematical uncertainty of $\Delta T_{\parallel} \simeq 0.2\,\mathrm{K}$ and $\Delta(N_{\mathrm{hot}}/N\mathrm{total}) \simeq 0.1$. However, after 23 s one clearly observes a sharp drop

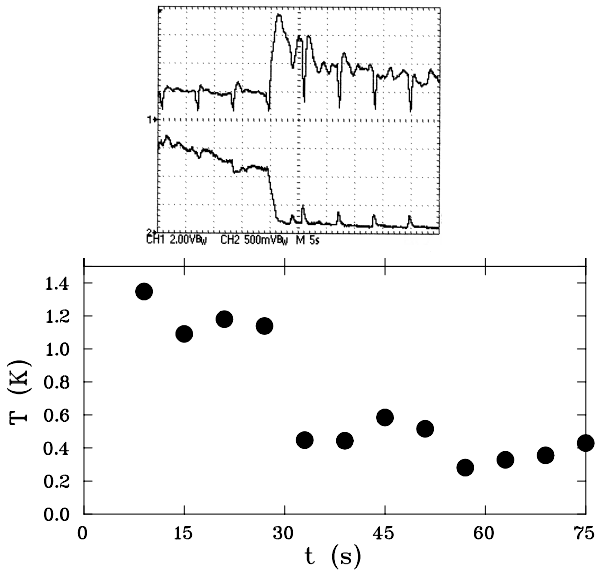


**Figure 3.14:** *The transition observed in the fluorescence signals (upper plot) is accompanied by a drop in the longitudinal beam temperature.*

in the longitudinal temperature from $T_{\parallel} = 1.2\,\mathrm{K}$ to 200 mK. During these measurements both photomultiplier signals were online monitored with a digitizing oscilloscope (Tektronix TDS 210). A screenshot is also presented in figure 3.14. The temperature drop and the disappearance of hot ions is coincident with the sudden change of the fluorescence signals. The periodical dips and spikes in the fluorescence signals result from the HV-scans which disturb the ion distribution due to the acceleration at the the drift tube section. During the scan, the signal of photomultiplier 1 (cold fraction) produces a dip while the second detector (hot fraction) shows a spike. This might indicate a transfer of cold ions into the hot background due to the disturbance of the system. After the scan has been finished, the hot ions are cooled back to the cold subensemble.

The repeated transfer of ions between the hot and the cold subensemble can already be seen in the first presented fluorescence measurement (figure .3.12). Although the system was not disturbed by velocity measurements, one notices repeated changes of the fluorescence rate between two levels. The hot fraction fluorescence fluctuates between straylight level and a signal rate that corresponds to the usual exponential decrease of the ion current. The similar case for the cold distribution: The increased fluorescence rate after the transition from time to time

drops to the rate expected for a regular beam behavior. The fluctuations in the fluorescence signals between two states without changing the cooling conditions demonstrate the fragility of the effect. The fluctuations might be caused by the limited stability of the storage ring components. The relative current stability of the dipole magnets is on the order of $10^{-5}$. These small drifts in the magnetic field lead to shifts of the closed orbit and thus to changes in the ion revolution frequency. The estimated fluctuation would be $\Delta\nu_{\mathrm{rf}} \simeq \pm 0.5\,\mathrm{Hz}$, which strongly influences the cooling rate.

For the observation of the longitudinal spatial distribution in the barrier bucket, a series of pickup measurements has been taken during the cooling process which is depicted in figure 3.15.

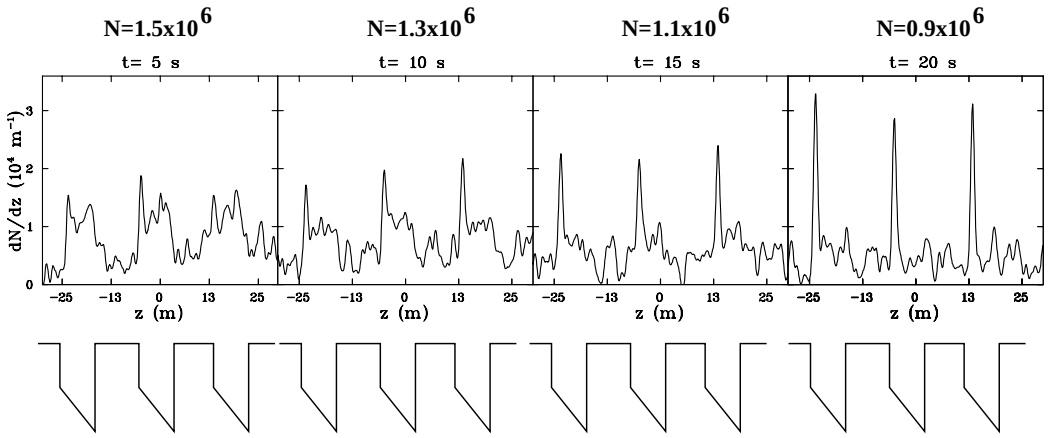


**Figure 3.15:** *Longitudinal ion distribution before and after the transition measured with the electrostatic pickup. The bunch potential is sketched below the plot. After the transition, the ion ensemble is pushed against the potential slope towards the left potential wall.*

Each pickup diagram shows the longitudinal density distribution of three bunches circulating in the ring. The bunch potential is sketched below the plots. The data has been carefully smoothed using a Gaussian filter to get rid off a large noise background. In the first two pictures, the ions are homogeneously distributed along the bucket. After 15 s one observes a significant increase of the ion density at the left bucket border. This effect occurs at the time of the drop in the fluorescence signal for the hot ions. This behavior strongly differs from the longitudinal ion dynamics of a transverse temperature increase due to dispersive heating as demonstrated in [Mudrich, 1999]. In this case, the beam transversally blows up, so that its diameter becomes larger than the laser beam waist. Ions experience a reduced average laser force because of their worse spatial overlap. Hence, ions are no longer in equilibrium with the counter force of the barrier

bucket, which leads to a density increase at the lower edge of the bucket (the right side in figure 3.15). The observation presented here shows an opposite behavior. Ions are pushed against the counter force towards the left bucket wall. Since the strength of the counter force does not change during the cooling process, it follows that the ions must experience a much stronger laser force after the occurrence of the transition. This result agrees with the increase of the fluorescence signal corresponding to the cold subensemble.

The onset of the anomalous beam behavior clearly depends on the number of ions stored. Experiments with higher beam currents at injection time leads to a disappearance of hot ions at later times respectively. The estimated particle number for the transition is $10^6$. Additional experiments were performed under the same conditions but with sinusoidal bunch potentials. The fluorescence signals show a similar behavior as already described. However, the pickup distributions showed a behavior which clearly indicate a transverse heat-up.

### 3.3.2 Transverse dynamics

For the examination of the transverse beam dynamics, the beam profile monitor (BPM) was used. Due to the low beam current the count rate was extremely small. It is not possible to measure a complete time series of profile pictures during the cooling process as presented for the other measurements. Hence, we accumulated a histogram of the transverse distribution over ten seconds during the time of regular beam behavior. A second measurement was made right after the transition for another ten seconds. Afterwards, the still very noisy data sets were filtered using the Savitzky-Golay method which widely conserves the zeroth and higher order statistical moments of the distribution [Press et al., 1992]. The resulting beam profiles before and after the transition are depicted in figure 3.16. One observes an increase of the beam diameter with the described change of the beam behavior. Therefore, the transition seems to be connected to an increase of the transverse beam temperature. Gaussian fits considering the apparative resolution limit of the BPM lead to a temperature of $T_{\perp,\mathrm{regular}} \simeq 1200\,\mathrm{K}$ for the regular and $T_{\perp,\mathrm{anom}} \simeq 5000\,\mathrm{K}$ for the anomalous beam behavior. The dashed curves represent the Gaussian intensity profile of the cooling laser. These profiles have been scaled to take into account that the focusing strength of the BPM position differs from the average strength along the laser cooling section, which is expressed by the ratio of the beta functions ($\overline{\beta_{\mathrm{laser}}}/\beta_{\mathrm{BPM}} \approx 1.3$). The measured beam dynamics obviously indicate a transverse heating effect. However, this heat-up differs significantly from the blow-up behavior through dispersive heating, which would lead to a temperature increase of $T_{\perp\mathrm{hot}} \geq 20000\,\mathrm{K}$. In our case, we observed a limited heat-up where the ion beam stays inside the laser intensity profile. The beam diameter does not broaden over all limits but stabilizes at a higher value.

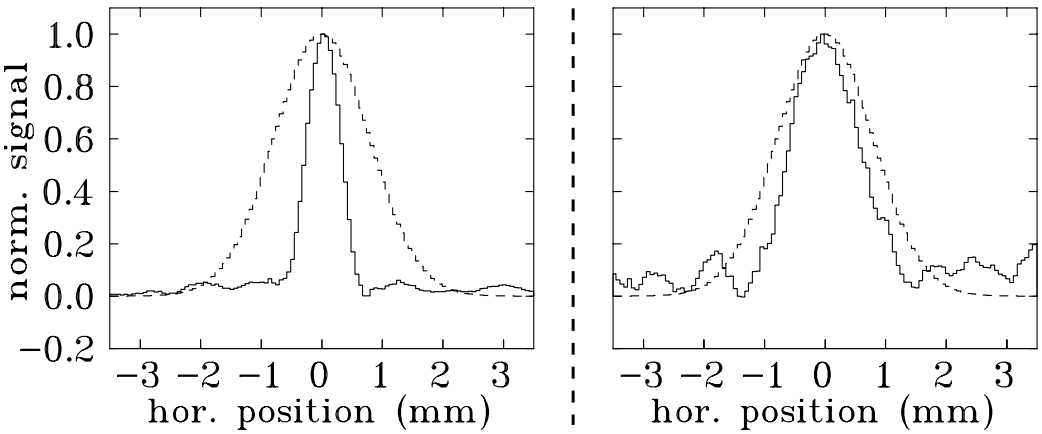


**Figure 3.16:** *transverse beam profiles before and after the transition*

## 3.4 Conclusion

The observation of the anomalous beam behavior can be summarized as follows: For a laser-cooled, barrier-bunched beam with weak dispersive cooling, an abrupt change of the cooling dynamics is observed at a given particle number. The anomalous beam behavior is measured by characteristic changes in the measurement data:

- Fluorescence scan: Increase of count rate in PM 1 accompanied by a drop of PM2 count rate down to stray light level.
- HV-scan: sudden disappearance of hot background ions, longitudinal temperature drop of the cold distribution.
- Pickup: sharp peak at the left bucket border.
- BPM: limited broadening of the transverse beam profile.

The measured laser beam blow-up could indicate a transverse heating process. This blow-up also leads to a decrease in the phase-space density and thus a reduction of the intra beam collision rate. Hence, a transverse heating would also explain the disappearance of hot background ions due to a complete vanish (or strong suppression) of IBS heating. However, one observes only a limited heating. Although the BPM statistics is quite poor, the width of the ion beam does not become wider than the laser width. This fact is also confirmed by the observation that the ion ensemble jumps repeatedly between the regular and the anomalous state back and forth. An unlimited blow-up with a beam diameter much bigger than the spatial laser width would be irreversible [Mudrich, 1999]. Therefore, the ion beam reveals a bistable longitudinal-transversal coupled dynamics.

A possible interpretation of the presented effects would be a one-dimensional beam crystallization. Theoretically, a condensation would be connected to a complete disappearance of IBS. This interpretation would also be carried by molecular dynamics simulations done for the TSR lattice that predict a 1D beam crystallization for inter-particle distances of 30 $\mu$m which correspond to the experimentally achieved total ion number of $10^6$. The measured increase of the beam-diameter however would stay in contradiction to the assumption of Coulomb ordering. Due to the strong shear forces an ion crystal would experience while passing a dipole magnet it is not expected to observe Coulomb ordering for beams with transverse diameters larger than the mean longitudinal particle distance. In addition, the typical 1D longitudinal plasma parameter (as defined in section 2.2.4) right after the observed effect derived from the experimental data (longitudinal/transverse temperatures and densities) is $\Gamma_{1\mathrm{D}} \approx 0.1$. This value is one order of magnitude smaller than the value ($\Gamma_{1\mathrm{D}} \approx 1$) for the expected onset of Coulomb ordering.

For the beam profile measurement, one has to consider the very poor statistics which lead to a large uncertainty in the determination of the beam width. In addition, the BPM measurement has been integrated over ten seconds. The permanent fluctuations during this time seen in the fluorescence signals could not be resolved. Furthermore, the broadening of the BPM signal does not necessarily need to be caused by a heat-up of the beam. One could possibly think of a coherent horizontal oscillation of the whole bunch around the closed orbit. Such a phenomenon has actually been observed for crystalline beams in small ion traps (PALLAS,[Schätz et al., 2001]).

An alternative interpretation for the described effect relies on a weak dispersive heating: One assumes the the position shift of the laser width with respect to the ion beam leads to a very weak transverse heating. For a high beam current however, the indirect cooling mechanism due to IBS still overcomes this heating which avoids a beam blow-up. With the decreasing ion current during the cooling process, IBS cooling becomes more and more inefficient until dispersive heating overcomes the indirect cooling. The resulting blow-up further reduces IBS which leads to a strong suppression of scattered background ions in the longitudinal degree of freedom. The longitudinal velocity distribution collapses and almost all ions become resonant with the laser. The resulting significantly enhanced cooling rate then might possibly stabilize the transverse beam dynamics. However, the stabilization of the transverse degree of freedom contradicts the assumption of extremely weak coupling through IBS. In addition, for the presented experiments we adjusted and repeatedly verified the horizontal laser position to ensure dispersive cooling.

Further possibilities for the interpretation of the effects assuming weak dispersive cooling would include additional mechanisms that depend on the phase-space density or the beam width. It is known that space charge could produce a shift of

the betatron tune. Such a shift could also lead to beam instabilities (ring resonances). An instability would reduce the space-charge effect and therefore the tune shift which leads to a stabilization. Higher order coupling effects such as the storage ring chromaticity could also be possible candidates for a heating mechanism. The coupling through chromaticity would depend on the beam width or its shape respectively. In this case, the decreasing beam diameter during the cooling process would cause an additional heating effect. The beam blow-up would again lead to stabilization. However, this mechanism would not suddenly occur in an abrupt step as experimentally observed.

In conclusion, the experimentally observed effects can not fully be explained in a consistent picture. In particular, the transverse dynamics has to be examined in much more detail with the help of improved diagnostic tools. In the future, the recently installed magneto-optical trap possibly allows a further insight to this phenomenon. On the other hand, the presented experiments represent the physical and technical limit for the cooling rate that can be achieved using bunched beams. In particular, the adjustment of the bunching frequency turned out to be very critical. At very small detunings $\delta\nu \approx 0$ needed to achieve high longitudinal cooling rates one comes close to the regime of strong longitudinal heating for $\delta\nu$ slightly below zero. This tricky adjustment makes it hard to achieve the presented extreme phase-space densities never reached before at a storage ring. Therefore, the following experiments employ a completely different method to achieve a counter force using a second counterpropagating laser.

# Chapter 4

# Coasting beam cooling in an optical molasses

The following chapter describes first experiments on laser cooling of coasting (unbunched) ion beams using a so-called optical molasses. For bunched beams the cooling forces consisted of the copropagating argon ion laser accelerating the ion and the bunching potential producing the needed counterforce to decelerate them. The cooling scheme presented here makes use of a second counterpropagating laser to realize the counterforce. This method overcomes several limitations of the bunched cooling scheme. Since laser forces are much stronger than the forces that technically be reached through beam bunching it is in principle possible to achieve much higher friction coefficients using two laser beams as shown in figure 4.1. Higher friction coefficients lead to higher cooling rates and thus to lower beam

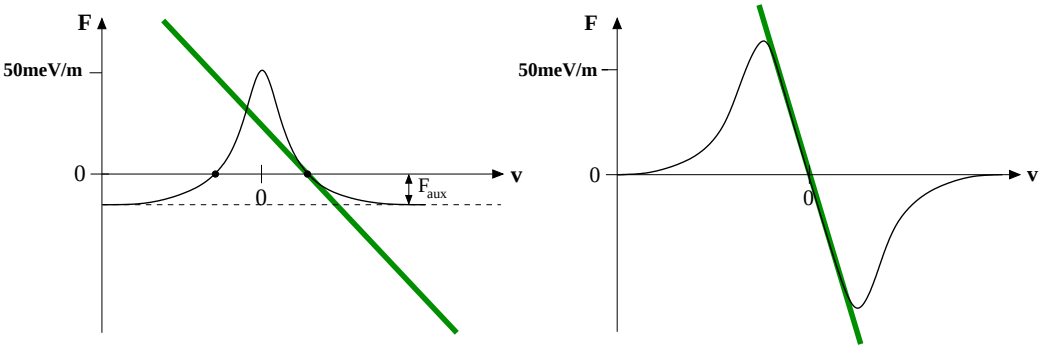


**Figure 4.1:** *Schematic force profiles in case of bunched cooling in barrier buckets (left) and molasses cooling (right). It is possible to achieve higher friction coefficients (represented by the slopes in the plots) in an optical molasses than for bunched beam cooling.*

temperatures (section 2.2.3).

Furthermore, a coasting beam is much better suited in view of the observation of Coulomb ordering. Since there are no forces confining the ions longitudinally, the number density along the closed orbit and therefore the intermediate ion distance is homogeneous. In particular, the longitudinal spatial distribution remains constant independently from the cooling conditions.

Another critical point of bunched cooling is extreme sensitivity of the cooling process on the bunching frequency especially during the observation of the disappearance of hot background ions. The cooling conditions during molasses cooling are almost independent from drifts of the storage ring. They are only defined by the properties of the laser system (frequencies, intensities).

The use of a second, frequency-tunable laser system offers the possibility of an additional longitudinal velocity measurement (Doppler thermometry). Furthermore, for a coasting beam, Schottky analysis becomes a valuable tool for a non-destructive investigation of longitudinal phase space. Therefore the cooling dynamics can be examined in even more detail than in case of bunched cooling.

The transition wavelength of Beryllium ions at rest is $\lambda = 313.13\,\text{nm}$. The velocity of 4.1% of the speed of light leads to a Doppler shift of 13 nm, so that the 300.13 nm line of the argon ion laser is used for the copropagating direction. For the counterpropagating direction the sign of the Doppler shift is reversed. Hence, the new cooling method requires a second tunable laser system with a wavelength of $\lambda = 326\,\text{nm}$. Since there is no laser system commercially available which directly delivers this wavelength, we built up a frequency-doubling system to convert laser light at $\lambda = 652\,\text{nm}$ delivered by a dye laser to the needed wavelength.

## 4.1 Laser system at 326 nm

The use of a fixed-frequency argon ion laser system at $\lambda = 300\,\text{nm}$ for the copropagating direction makes it necessary to build up a frequency-tunable laser system at $\lambda = 326\,\text{nm}$ for the copropagating direction. There are Helium-Cadmium laser systems available providing light with $\lambda \approx 326\,\text{nm}$ at an cw output power of $P \simeq 100\,\text{mW}$. Unfortunately, these lasers are fixed-frequency systems and can only be frequency-tuned in narrow range of less than 500 MHz. For bunched cooling, the optimum cooling conditions are adjusted by a variation of the bunching frequency which shifts the ions in longitudinal velocity space to become resonant with the cooling laser. For coasting beam cooling, the ions have to be resonant with both lasers which can practically only be realized by a laser system with an adjustable light frequency. For laser cooling, the needed frequency range should be at least 25 GHz around the optimum adjustment. For our purposes, the needed wavelength is produced by frequency doubling a commercially available dye laser

system. The dye laser (Coherent INNOVA CR-699, laser dye: DCM) produces light with a wavelength of 652 nm with a typical cw output power of 700 mW. This system is pumped by a frequency-doubled Nd:YAG laser (Coherent VERDI-10) at 532 nm and a power of typically 6 Watts. The wavelength of the dye laser system can be mechanically tuned over 70 nm. At a given wavelength, the laser is able to perform a continuous frequency scan over 30 GHz in 5 seconds.

For the frequency doubling process one makes use of a special crystal with non-linear optical properties. For an efficient light conversion process, high input light power is needed, which can be achieved by the use of an optical resonator. Some years ago, such a laser system has already been built up [Horvath, 1994] for longitudinal beam diagnostics [Stoessel, 1997]. However, the output power of about one milliwatt was too small to use this system to counteract the argon ion laser. The reason for that was the resonator geometry which made it necessary to use crystals with an anti-reflective coating. It turned out that the low destruction limit of the coating greatly limited the achievable output power. To overcome this limitation, a new resonator geometry was chosen where the non-linear crystal is cut in a Brewster angle to avoid reflection losses. A detailed description of the new experimental setup is given in [Friedmann, 2001].

### 4.1.1 Frequency doubling

In the linear optical regime, one assumes the conservation of frequency for light passing matter and the validity of the superposition principle. Two different electromagnetic waves can overlay without influencing each other. However, both assumptions are only correct for small light intensities as produced by conventional light sources. Therefore, the linear relation between the polarization $\vec{P}$ of a medium and the electric field $\vec{E}$ is a valid approximation for small field strengths only:

$$\vec{P} = \epsilon_0 \chi \vec{E} \tag{4.1}$$

($\epsilon_0$: electric field constant, $\chi$: electric susceptibility). This linearity relies on the harmonic atomic binding potential for electrons oscillating with small amplitudes. For larger amplitudes due to a stronger electric driving field, electrons more and more experience deviation from the parabola shape of the potential. The oscillation becomes an-harmonic. In this case, the susceptibility $\chi$ is no longer a constant but also depends on the electric field strength

$$\vec{P} = \epsilon_0 \chi(\vec{E}) \vec{E} \quad . \tag{4.2}$$

This relation can be expanded in a Taylor series

$$\vec{P} = \epsilon_0 (\chi_1 \vec{E} + \chi_2 \vec{E}^2 + \chi_3 \vec{E}^3 + \cdots) \quad . \tag{4.3}$$

For an electromagnetic wave $\vec{E} = \vec{E}_0 \sin(\omega t + kz)$ one attains besides the linear term of the polarization for the quadratic part

$$\vec{P}_2 = \epsilon_0 \chi_2 \vec{E}_0^2 \sin^2(\omega t + kz) \tag{4.4}$$

$$= \frac{1}{2}\epsilon_0 \chi_2 \vec{E}_0^2 + \epsilon_0 \chi_2 \vec{E}_0^2 \cos(2\omega t + kz) \quad . \tag{4.5}$$

Hence, the polarization oscillates with the *double* frequency of the the driving field. This is the basic principle of optical frequency doubling (second harmonic generation, SHG). The following third and higher order corrections lead to frequency tripling and so forth respectively. A further detailed description can be found in [Franken et al., 1961]. From the above equation, one can derive another important property of frequency doubling: Since the light intensity is proportional to the square of the electric field ($I \sim \vec{E}_0^2$), one gets the relation

$$I(2\omega) \sim I^2(\omega) \quad . \tag{4.6}$$

Therefore, the intensity of the fundamental light wave fed to the non-linear medium strongly influences the efficiency of the conversion process.

### 4.1.2 Experimental realization

Typical values for the coefficients $\chi_1, \chi_2, \ldots$ are in the order of

$$\chi_1 \approx 1 \quad , \quad \chi_2 \approx 10^{-10}\,\frac{\mathrm{cm}}{\mathrm{V}} \quad , \quad \chi_3 \approx 10^{-18}\,\frac{\mathrm{cm}^2}{\mathrm{V}^2} \quad . \tag{4.7}$$

Due to the small values of $\chi_2$ and $\chi_3$, high intensities are needed to have notable non-linear effects for light going through matter. In order to achieve UV light with a power of some milliwatts, the needed input intensity fed into the crystal must be in the range of some megawatts/cm$^2$. To achieve these extreme intensities one can focus the beam to very small beam waists. However, a focus area of $3 \cdot 10^{-5}$ cm$^2$ (beam waist 28 $\mu$m) still leads to a needed input power of some ten watts, which is not achievable with todays available cw dye laser systems. The needed input power can be produced by enhancing the dye laser light through an optical resonator. The light continuously fed into an optical resonator is stored in it which leads to a summ-up of the light power inside this resonator [Lange, 1994].

#### The non-linear crystal

An important factor for optimum frequency conversion is the choice of the right crystal type. For the given conversion process (652 nm $\rightarrow$ 326 nm) Lithium iodate

($LiIO_2$) has the highest conversion efficiency $\eta_k = 2.65 \cdot 10^{-4}$/W of all crystals commercially available. Furthermore, optimum conversion strongly depends on the focusing of the fundamental light wave. At this point, one has to find the optimum trade-off between different effects: On the one hand, a small focus produces high intensities important for the conversion process. On the other hand, an extremely focussed beam has a large divergence. The extreme light intensity is thus limited to a comparably small range (Rayleigh range) around the focus on the optical axis. Considering several further parameters such as crystal length, absorption, phase-matching conditions [Franken et al., 1961] etc, an optimization procedure [Boyd and Kleinmann, 1968] leads to an optimum Gaussian beam waist of $w_{\mathrm{opt}} = 28\,\mu$m for a given crystal length of $l$ =6 mm. The optimum beam waist inside the crystal is also the starting point for the calculation of the optical resonator.

**Optical resonator**

For the setup of optical resonators different arrangements of mirrors are possible. The easiest setup is the well-known Fabry-Perot resonator consisting of two mirrors facing each other. This type can not be used since UV light generation of a crystal placed inside would go in both directions along the optical axis. A comparison of different possible resonator designs with their particular advantages and disadvantages is presented in [Horvath, 1994].

For our doubling system, we chose a resonator design consisting of two concave and two plain mirrors arranged in "bow-tie" (double-Z) geometry as depicted in figure 4.2. The non-linear crystal is placed in between the concave mirrors. The crystal surfaces are arranged in a Brewster angle with respect to the optical axis in order to avoid losses due to reflections. As mentioned, this design does not need any anti-reflective coatings on the crystal surfaces which limited the input power in former SHG systems. The dimensions of the resonator have been calculated using Gaussian matrix optics [Kogelnik, 1966] with the goal to produce the optimum focus $w_{\mathrm{opt}}$ inside the crystal as derived above. Furthermore, the mirror distances have to be calculated in view of an maximum optical stability [Lange, 1994]. This means that the resonator is most insensitive to small geometry deviations from the calculated optimum. This is comparable to the situation of the storage ring where one has to ensure stable ion trajectories. The bow-tie design has the advantage, that optical aberrations such as beam astigmatism produced by the concave mirrors can be exactly compensated by the Brewster geometry of the crystal.

For an enhancement of the input power, one additional condition has to be fulfilled: The optical length of the resonator must exactly match an integer number of $\lambda/2$, so that the system actually becomes resonant. In this case, all light power fed into the system is coherently summed up. From the experimental point of

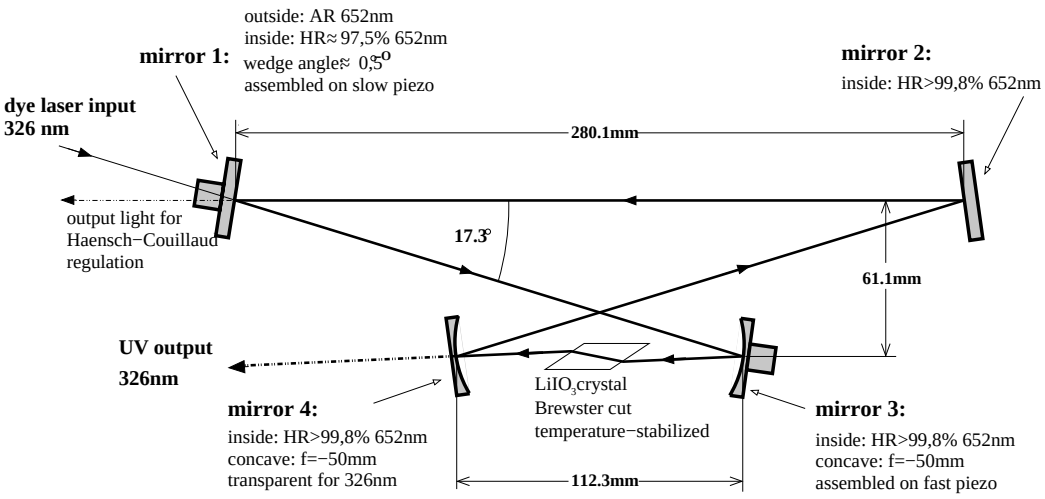


**Figure 4.2:** *Schematic picture of the frequency doubling system (AR: anti-reflective coating, HR: high-reflective coating). The non-linear crystal is centered between both concave mirrors that produce the optimum beam waist for the second harmonic generation (SHG).*

view, this means that the optical length must be kept constant on a nanometer scale to achieve stable conditions of operation. For this purpose, the resonator length is actively stabilized by mounting two of the resonator mirrors on piezo actuators. These piezo elements can compensate unavoidable fluctuations due to acoustic and other mechanical disturbances from the environment as well as temperature drifts.

### Resonator stabilization

For the regulation, one makes use of a locking scheme first demonstrated by Hänsch and Couillaud [Hänsch and Couillaud, 1980]. This method derives an error signal by measuring the relative phase between the light reflected at the input coupling mirror and the wave that has passed an integer number of round-trips of the resonator. In case of resonance, the phase is exactly zero. For a positive length deviation, the phase shift is also positive and vice versa. Hence, the error signal derived from the phase shift can be used to produce a control voltage that is applied to the piezo mirrors. The resonance properties as well as the corresponding regulation signal is shown in figure 4.3. The upper picture shows the light power directly measured behind a resonator mirror (mirror 2 in figure 4.2) by a photodiode. The measured power of light passing the mirror due to the non-perfect reflectivity is proportional to the light power in the resonator. To demonstrate the resonance behavior, the length of the system is continuously swept by applying

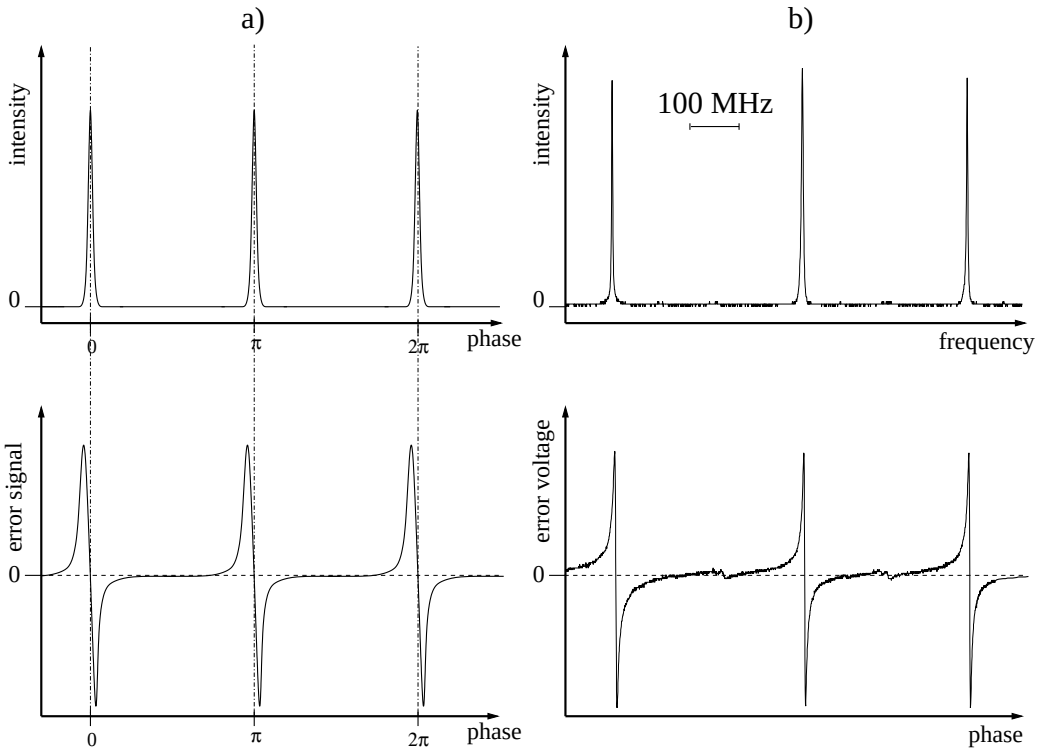


**Figure 4.3:** *Mode spectrum and error signal for the resonator stabilization using the method of Hänsch and Couillaud. The left side shows the theoretical signals while the corresponding measured data is depicted in the right column.*

a linear voltage ramp to one piezo. During the scan, for well-defined lengths the resonance condition is fulfilled and the light power is strongly enhanced which results in the series of peaks. The lower plot shows the corresponding error signal. At the resonance maximum the signal crosses the zero line. For length stabilization the electronic regulation system (three-point PID regulator) changes the piezo voltage (and thus the resonator length), so that this signal is kept zero. The distance between two resonance peaks corresponds to the *free spectral range* $\nu_{\mathrm{FSR}}$ of the resonator. This value corresponds to the frequency the laser has to be detuned to hop from one resonance to the next one. It can be calculated as $\nu_{\mathrm{FSR}} = c/L$ with $c$: speed of light and $L$: optical resonator length. The frequency width (FWHM) $\Delta\nu$ of the resonance peak determines the quality of the resonator mainly influenced by the reflectivity of the mirrors and losses due to crystal absorption as well as the wanted conversion process itself. The ratio of the frequency width and the free spectral range is the so-called *finesse* $F = \Delta\nu/\nu_{\mathrm{FSR}}$. This value can be interpreted as the average number of round-trips a photon performs in the resonator until it is lost or converted respectively. An characteristic value is the light ampli-

fication factor $A$ which is the ratio of the light power inside the resonator $P_{\text{res}}$ and the power fed into $P_{\text{in}}$. It can be calculated from the finesse $F$ and the reflectivity $R_{\text{i}}$ of the input coupling mirror: $A = P_{\text{res}}/P_{\text{in}} = F^2(1 - R_{\text{i}})/\pi^2$. Typical values of the whole setup are given in table 4.1.

| **Basic data** | |
|---:|---|
| basic wavelength | $\lambda_\omega = 652\,\text{nm}$ |
| UV wavelength | $\lambda_{2\omega} = 326\,\text{nm}$ |
| crystal type | $LiIO_2$, Brewster cut |
| crystal length | $L_{\text{c}} = 6\,\text{mm}$ |
| refractive index | $n_0(\omega) = 1.879$ |
| crystal phase matching | angle-tuned, $\theta_{\text{phase}} = 59.8°$ |
| crystal focus | $w_0 = 29\,\mu\text{m}$ |
| **Resonator data** | |
| optical resonator length | $L_{\text{res}} = 803.2\,\text{mm}$ |
| free spectral range | $\Delta\nu \approx 373\,\text{MHz}$ |
| resonance width | $\delta\nu \approx 2\,\text{MHz}$ |
| finesse | $F \approx 183$ |
| typ. input power | $P_{\text{in}} \approx 600\,\text{mW}$ |
| power enhancement | $A \approx 86$ |
| input coupling efficiency | $\epsilon \approx 75\%$ |
| light power in resonator | $P_{\text{res}} \approx 45\,\text{W}$ |
| typ. output power | $P_{\text{out}} \approx 35\,\text{mW}$ |

**Table 4.1:** *Important technical specifications of the frequency-doubling system.*

As mentioned, *two* of the four mirrors are equipped with piezo actuators. The first piezo element produces maximum elongations of 8 $\mu$m and can be driven with frequencies up to 8 kHz. The frequency limit of the second piezo is about 10 Hz but with a bigger elongation of 35 $\mu$m. While the first actuator compensates fast acoustic and other mechanical vibrations, the slow piezo compensates long-term fluctuations such as temperature drifts. Furthermore, the slow piezo is needed to keep the system in resonance while performing a frequency scan with the dye laser.

Picture 4.4 shows the achieved UV light power with respect to the input dye laser power. One clearly observes the quadratic dependency as described in equation 4.6. The solid line is a fit through the experimental data. From this curve, one calculates a conversion efficiency of $\eta_{\text{k}} = 7.9 \cdot 10^{-2}\,/\text{W}$. The quadratic dependency over the whole input power range shows that this system is not limited due to thermal lenses or crystal degeneration which should result in deviations from the fit curve for higher input intensities.

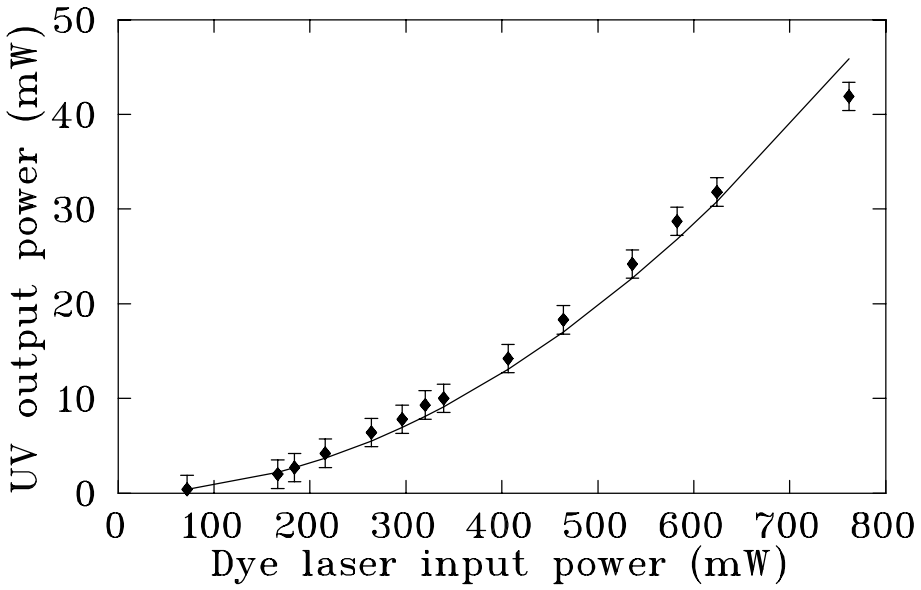


**Figure 4.4:** *Converted ultraviolet output power ($\lambda_{\mathrm{UV}} = 326\,nm$) plotted against the dye laser input power ($\lambda_{\mathrm{dye}} = 652\,nm$). One observes the characteristic quadratic dependency for a frequency doubling system. The solid line is a quadratic fit through the experimental data.*

### Beam shaping

Like all technically used non-linear optical crystals, the used lithium iodate crystal is birefringent. The crystal has two optical axes with different refractive indices. An incoming beam not aligned along one of these axes is split up in two beams (ordinary and extraordinary beam) with a *walk-off* angle. For frequency doubling, the refractive index of the fundamental light frequency must be equal to the index of the doubled frequency ($n(\omega) = n(2\omega)$). This is the so-called *phase matching* condition. This condition is in our case be fulfilled by shining in the fundamental frequency with a well-defined angle ($\theta = 59.8°$) with respect to the ordinary optical crystal axis. This leads to the described beam walk-off for the frequency-doubled light coming out of the crystal. Due to the modified output angle, the frequency-doubled light hits the output crystal surface as well as the output coupling mirror of the resonator such that the intensity profile is no longer radial-symmetric. The outcoming light has an elliptic cross section. This effect is known as beam astigmatism. In order to produce a symmetric Gaussian beam, a telescope of cylindric lenses was set up, which modifies only the horizontal beam waist. In our case, a telescope consisting of a convex (f=300 mm) and a concave (f=-300 mm) lens with an intermediate distance of 610 mm positioned 375 mm apart from the resonator results in an almost perfect Gaussian beam profile.

**Beam guidance**

The setup for beam guidance is similar to the argon ion laser system as shown in figure 4.5. A second laser beam positioning and stabilization system was installed

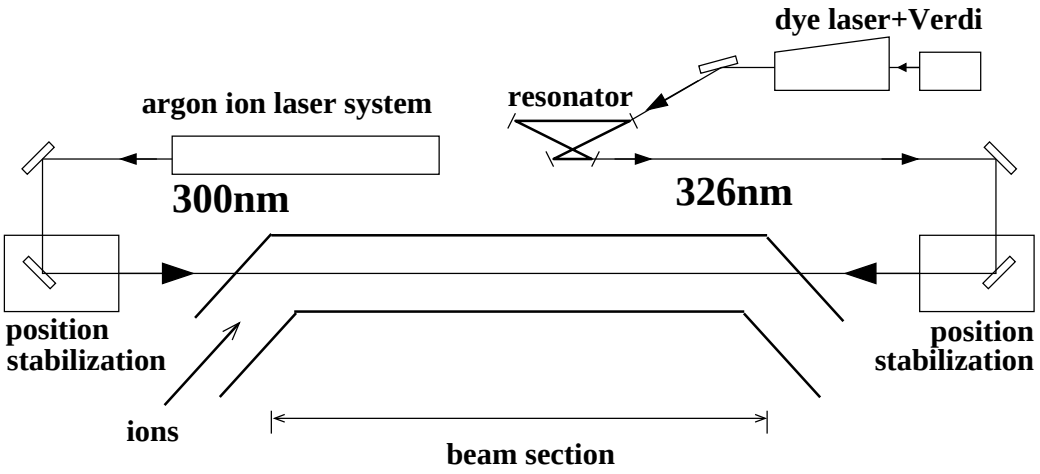


**Figure 4.5:** *Experimental setup for molasses cooling. Similar to the copropagating argon ion laser beam, the frequency-doubled light is guided by a set of mirrors to the cooling section of the storage ring.*

to also ensure a perfect overlap with the ion beam as well as the copropagating laser system over more than five meters. A perfect alignment of both laser systems however would lead to a reflection of the 300 nm light from the copropagating argon ion laser back to the frequency doubling system leading to disturbances. To avoid this, one of the dielectric mirrors was chosen to be high reflective for a wavelength of $\lambda = 326\,\mathrm{nm}$ and has an anti-reflective coating for 300 nm light, thus blocking the argon ion laser light. Due to the lower output power of the frequency-doubled light the beam was focussed to a comparably small beam waist of $w_{326} \approx 1\,\mathrm{mm}$ at the storage ring in order to increase the intensity. Furthermore, the small diameter reduces the influences of the non-perfect Gaussian intensity profile on the cooling process.

A frequency scan of the dye laser system is performed by applying an external control voltage (between $\pm 10\,\mathrm{V}$) to the control system of the laser. In our experiments, this voltage was supplied by an arbitrary function generator (HP 33120A). A scan was done by sending a trigger signal to this device which feeds a preprogrammed voltage ramp to the laser system. This setup gives us an extreme flexibility for diagnostics scans as well as a very precise control of the cooling conditions.

**Generation of the second frequency**

Similar to the argon ion laser system one has to provide *two* laser frequencies to avoid optical pumping between both hyperfine-split ground states (see figure 2.12). That was the reason why two separate argon ion lasers with a relative detuning of 1.3 GHz (due to the Doppler-shifted splitting of 1.25 GHz at rest) were used. For efficient cooling of a coasting beam, one also has to provide a second laser frequency for the counterpropagating direction. which must be detuned by 1.2 GHz due to the negative Doppler shift. This second laser beam was produced by frequency shifting a part of the generated UV light through an acousto-optical modulator (AOM). An AOM consists of a crystal or glass material. An acoustic wave ($\nu_{\mathrm{AOM}}$) is fed into this medium which leads to the generation of a phonon lattice inside. Laser light ($\nu_{\mathrm{las}}$) going through can do Bragg scattering on this lattice which results in a second beam diffracted by a definite angle. Scattered photons pick up the phonon momentum which leads to a frequency shift of the deflected beam $\nu_{\mathrm{scatter}} = \nu_{\mathrm{las}} + \nu_{\mathrm{AOM}}$. Since the diffraction efficiency of AOM systems with an acoustic frequency of 1.2 GHz is extremely low ($< 2\%$) we made use of a double-pass technique schematically depicted in figure 4.6. For this method, an

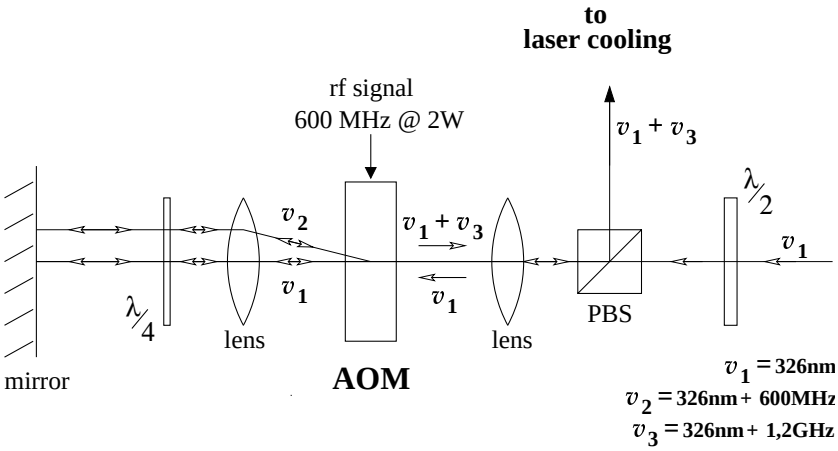


**Figure 4.6:** *The second laser frequency detuned by 1200 MHz is generated using an acousto optical modulator system in double-pass technique.*

AOM with $\nu_{\mathrm{AOM}} = 600$ MHz (Brimrose UV series, input power 2 Watts) is used and the laser frequency is shifted in two steps. The original laser frequency ($\nu_1$) delivered by the SHG system first passes a polarizing beam splitter cube (PBS) with maximum transmission due to a well-adjusted polarization angle (half-wave plate). The focussed beam goes through the AOM producing a second diffracted beam $\nu_2 = \nu_1 + 600$ MHz. A second lens and a mirror are arranged in a "cat's eye configuration", which leads to a perfect back reflection of laser rays coming from

the AOM regardless of their particular angles to the optical axis. The diffracted beam $\nu_2$ passes the AOM for a second time where again a part of it is diffracted back to the original direction with a frequency $\nu_3 = \nu_1 + 2 \cdot 600\,\mathrm{MHz}$. This beam is exactly collinear with the laser light at $\nu_1$ that has passed the setup without any deflections. A quarter-waveplate in front of the mirror leads to a rotation of the beam polarization axis by 90 degrees while passing it two times (forth and back). Due to the changed polarization of the beams $\nu_1$ & $\nu_3$ they are reflected out at the beam splitter cube. The superposition of these two beams is then guided through a telescope to the laser cooling section of the storage ring.

The measured diffraction efficiency of the AOM is $\epsilon \approx 50\%$ according its specifications. Hence, one would theoretically expect an output efficiency of 25% ($\hat{=}(50\%)^2$) for each beam ($\nu_1$ & $\nu_3$). The remaining 50% of the original input power is lost at the second AOM pass consisting of deflected light $\nu_1$ and the undisturbed part of $\nu_2$ going straightly through. Experimentally, one achieves a usable output power of typically $P_{\nu_1+\nu_3} \simeq 15\,\mathrm{mW}$ with $P_{\nu_3} \simeq 4\,\mathrm{mW}$ and $P_{\nu_1} \simeq 11\,\mathrm{mW}$.

## 4.2 Measurements

### 4.2.1 Doppler thermometry

Experiments using this new system were performed in December 2000. A first proof-of-principle experiment was done by measuring the longitudinal velocity distribution of an electron-cooled ion beam. For this purpose, only the new counterpropagating laser system was used, which acted as a diagnostic tool. The AOM system was switched off so that only one laser frequency was used. After beam injection, the ions were electron-cooled for ten seconds until the beam reaches temperature equilibrium. After that a frequency scan over a UV range of 15 GHz (corresponding to a dye laser scan of 7.5 MHz) was started. The scan time was five seconds. The fluorescence light of ions being excited by the laser was recorded with the photomultipliers. During the laser scan, each velocity class of the electron-cooled ion ensemble with its particular Doppler-shifted transition frequency becomes resonant with the laser. The time profile of the fluorescence count rate thus corresponds to the longitudinal velocity distribution of the ion ensemble. Such a typical diagnostic scan is depicted in figure 4.7 where the horizontal time axis is translated into a frequency axis of the scanned laser. The measured profile matches a Gaussian distribution. A fit to the data leads to a sigma width of $\sigma_\nu = 1.8\,\mathrm{GHz}$. This frequency width can be translated to a velocity width of

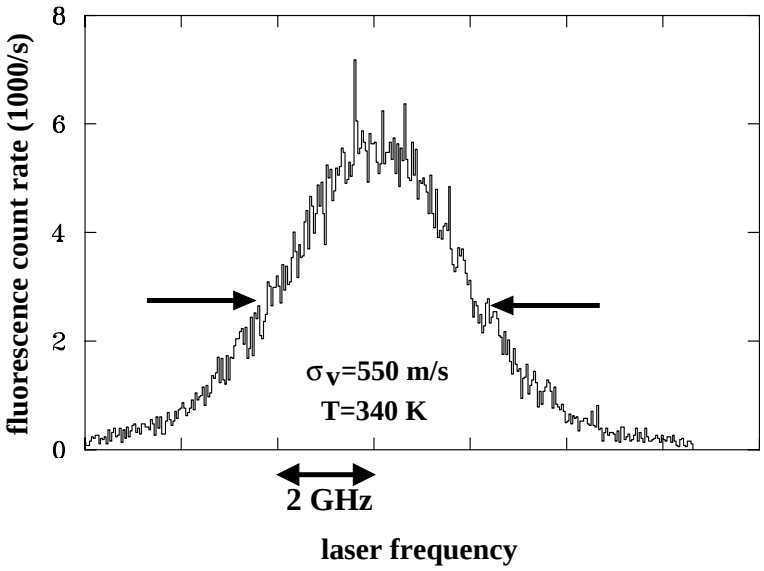


**Figure 4.7:** *Velocity profile of an electron-cooled beam measured through the fluorescence count rate during a frequency scan of the counterpropagating laser.*

$\sigma_v = 550\,\mathrm{m/s}$ using the Doppler formula

$$\sigma_v = \sigma_\nu \cdot \frac{\lambda_{\mathrm{ion}}}{\gamma} \quad , \tag{4.8}$$

with the transition wavelength $\lambda_{\mathrm{ion}}$ at rest and the relativistic factor $\gamma$. The measured velocity spread corresponds to a longitudinal temperature of $T_{||} = 340\,\mathrm{K}$ which is a typical value of an electron-cooled ion distribution. This scan method corresponds to measurements using HV-scans that lead to similar velocity widths. Instead of changing the ion velocity using drift tubes, one now changes the laser frequency.

Although the laser scan does not deliver complementary information on the cooling process with respect to the HV-scan, this method does not notably disturb the velocity distribution for small laser intensities. This is of particular interest for the observation of ordered ion beams.

### Doppler-free spectroscopy of the $\Lambda$-resonance

The new laser system can also be used to perform Doppler-free spectroscopy of the "$\lambda$-shaped" level scheme of Beryllium. For this purpose, one uses one fixed argon ion laser frequency being resonant with the transition from the upper hyperfine ground state to the excited state as shown in figure 4.8 (left). Due to the Doppler effect, this is only the case for a certain velocity class of the ion beam.

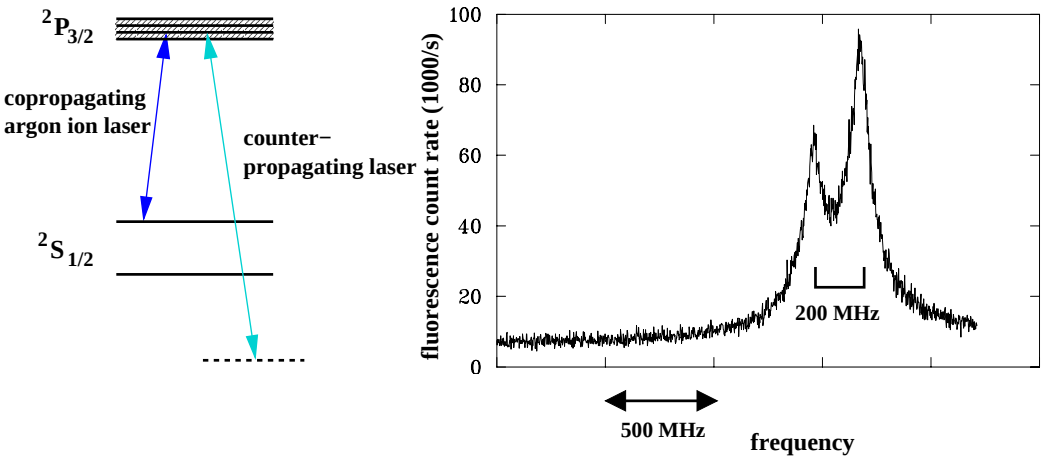


**Figure 4.8:** *Measurement of the $\Lambda$-resonance. The fixed argon ion laser is resonant with the upper hyperfine state. The excitation scheme is optically closed if the scanned laser system is resonant with the lower hyperfine transition leading to an increase of the fluorescence rate (right plot).*

The use of only one laser leads to an immediate optical pumping to the lower ground state in few absorption/emission cycles. Since the lower ground state is not resonant with the argon ion laser, ion can no longer be excited. One does not measure fluorescence light with the photomultipliers. For spectroscopy, one shines in the tunable counterpropagating laser. A frequency scan over the Doppler-shifted level scheme leads to a strong enhancement in the fluorescence rate exactly if the counterpropagating light is resonant with the lower hyperfine ground state. In this case, optical pumping is suppressed because ions being transfered to the lower ground state by the copropagating laser are now pumped back. One ends up with a closed optical transition scheme resulting in a high fluorescence rate. Due to the opposite Doppler shift of the co- and the counterpropagating laser fields, the condition for a closed optical transition can only be achieved for a certain velocity class defined by the argon ion laser frequency. Therefore, one does not observe Doppler broadening but measures the actual Lorentzian excitation probability of the atomic transition.

The measured fluorescence rate during a 4 GHz scan is shown in figure 4.8 (right). Surprisingly, instead of the expected Lorentzian peak one observes a two-peak structure with a frequency splitting of 200 MHz. Each peak can be very well fit by a Lorentzian function with a line line width of $\approx 45$ MHz. The so far unexplained splitting has been reproduced in three beam times. Detailed measurements did not show a dependency of the splitting on the the laser intensities, the scan direction or the scan time. Therefore, further investigations have to be done

to explain this effect.

This method represents an elegant way of Doppler-free spectroscopy of fast moving ions. Similar experiments are currently performed in a meta-stable $Li^+$ system to exactly measure the relativistic Doppler shift of particles moving with some percent of the speed of light. The goal of these experiments is a high-precision test of special relativity [Grieser et al., 1994]. The small line widths of the Beryllium system would suffice the requirements for a precision test, so that this ion species is also a possible candidate for a relavitity experiment.

### 4.2.2 Longitudinal cooling

For the first cooling experiments both laser systems were used. The AOM system was switched on, so that four laser frequencies (two copropagating and two counterpropagating) were acting on the ion beam. Right after injection, the beam was precooled by the electron cooler for 12 seconds. After that, repeated frequency scans of the counterpropagating laser with a span of 3.4 GHz forth and back over the ion resonance frequency have been performed. The time evolution of the measured fluorescence light during these scans is depicted in figure 4.9. The scan of

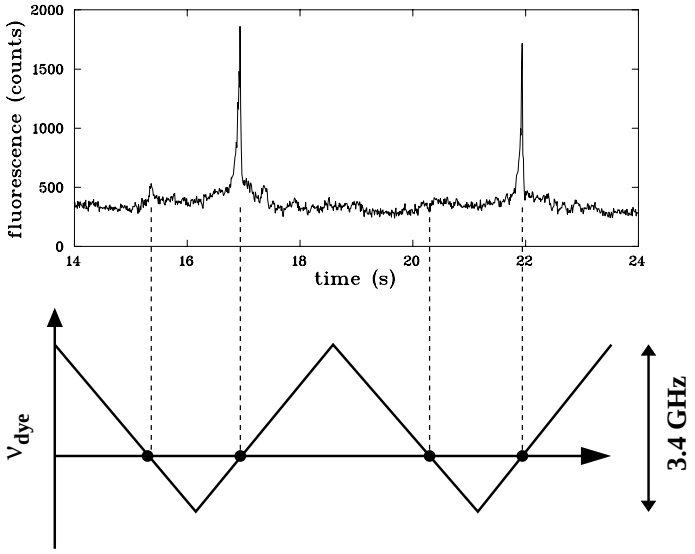


**Figure 4.9:** *First observation of molasses cooling during repeated frequency scans of the counterpropagating laser over the ion resonance. One observes asymmetric peaks in the fluorescence signal that appear only during an upward frequency ramp.*

the laser frequency is schematically shown below the plot. During these scans, one observes two narrow asymmetric peaks: The signal increases smoothly (left

side of the peak) but suddenly drops down producing a sharp edge. Furthermore, the peaks only occur if the frequency ramp goes upwards (from “red-detuned” to “blue-detuned”). This is the first clear signature of longitudinal beam cooling as explained in the following.

Figure 4.10 shows the force profiles of both lasers in velocity space as well as a zoom of the fluorescence data of the previous figure. The copropagating argon

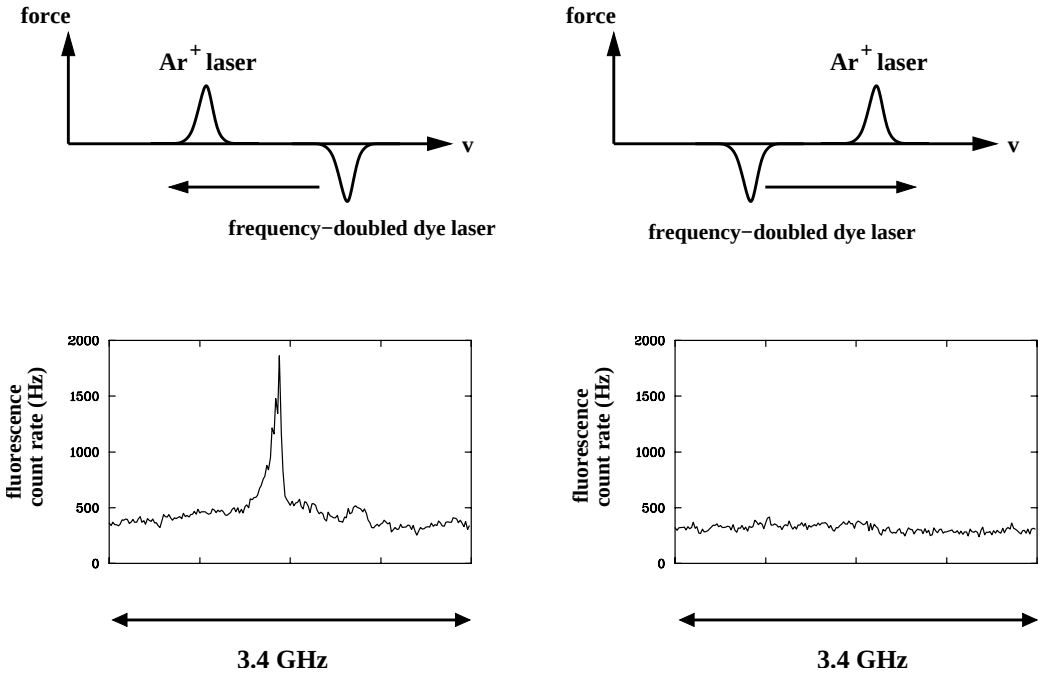


**Figure 4.10:** *The ion ensemble is either compressed in velocity space (left picture) or pushed apart (right picture) depending on the scan direction.*

ion laser accelerates the ions (positive force) while the counterpropagating laser system decelerates them (negative force). For a fixed light frequency, ions sitting around the resonance of the counterpropagating laser in velocity space would be shifted to lower velocities. Because of the changing Doppler shift, these ions immediately run out of resonance and no longer experience the laser force. Due to the frequency scan however, the decelerating force profile is shifted in velocity space.

In the left picture the frequency scan goes upwards which leads to a shift towards lower velocities. The above particles decelerated by the laser become resonant again and are thus further decelerated. The scanning laser therefore collects the ions in velocity space and pushes them ahead like a water wave in front of a ship’s bow. This is the basic principle of the *chirped laser cooling* scheme [Ertmer et al., 1985]. The whole ensemble is shifted towards lower velocities until

the distribution becomes resonant with the copropagating laser. Both force profiles leads to a velocity confinement of the ions sitting in between. While the relative detuning of the lasers becomes smaller and smaller the force profiles approach each other. The ion distribution is gradually further compressed in velocity space. More and more ions become resonant with the lasers which leads to a continuous increase of the fluorescence rate. This works until the relative detuning of both lasers becomes zero. For equal laser intensities the cooling force would exactly vanish. In our experiment with a decelerating laser of lower intensity one ends up with a weak accelerating force pushing the ion ensemble to higher velocities out of the laser resonance. Hence, an abrupt drop in the fluorescence rate occurs as experimentally observed. A further negative detuning of the cooling lasers does not change the situation: ions sitting around the argon ion laser force are accelerated, and ions being resonant with the frequency-doubled laser are further decelerated.

The opposite situation is depicted in the right picture. Ions sitting around the counterpropagating laser force profile are still decelerated as in the first case. However, the frequency scan to lower frequencies leads to a shift of the force profile towards higher velocities. Therefore, ions that have been decelerated by the laser never become resonant with the laser again during the scan. Hence, a reversed frequency scan does not lead to a collection of ions in velocity space. In addition, the negative detuning leads to an unstable point in the cooling force profile. Since there is no velocity compression of the particle ensemble and ions are permanently pushed out of the laser resonance one does not observe an increase of the fluorescence rate.

Note, that the ion ensemble is not heated for negative detunings as it is the case for the bunched cooling scheme where the laser drives the synchrotron oscillation. The ions are only pushed away from both lasers. Outside the laser resonance, the particles experience almost no laser forces. This is the reason for the observed behavior that even after a frequency scan in the “wrong” direction, the ions can be cooled back in a succeeding scan in direction of increasing frequencies.

The experiment was carried out with a total light power of the counterpropagating laser (two frequencies) of 10 mW. For a reduced laser power of $< 1$ mW as it was the case in former experiments (with almost the same beam waist) [Horvath, 1994, Stoessel, 1997] one observes almost no cooling effect. In this case, the scanned laser acts as a diagnostic tool not effecting the longitudinal velocity distribution, which leads to symmetric peaks that appear independently from the scan direction.

The presented observations clearly demonstrate the compression of the ion ensemble in velocity space. The new counterpropagating laser system in connection with the second frequency of the AOM system obviously produces a counterforce well suited for coasting beam cooling. Since the ion ensemble is in the above experiment only cooled for a very short time while the two force profiles

approaching each other the next measurement investigates coasting beam cooling for longer times.

### Long-term cooling

An ion ensemble can be cooled for longer times by stopping the laser scan at a given relative detuning. As in the previous experiment the ion ensemble is compressed during the laser scan. However the frequency scan is stopped just before the maxima of both laser force profiles are at the same position in velocity space (zero detuning). The development of the fluorescence signal during such an experiment is shown in figure 4.11. The ion beam is again precooled by the electron

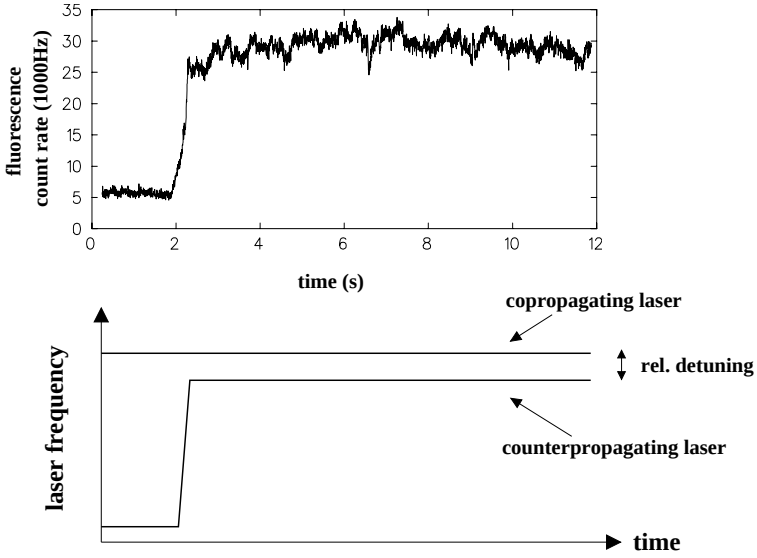


**Figure 4.11:** *Fluorescence signal during long-term molasses cooling. The counterpropagating laser scan stopped at a given relative detuning (schematic picture below the plot). The almost constant fluorescence rate indicates that the ions can be hold at the stable point in velocity space.*

cooler for 12 seconds. The frequency scan over 1.4 GHz starts 15 s after injection. At a relative detuning of $\approx 100$ MHz the scan is stopped. One observes an increase of the fluorescence rate during the scan over a time range of seconds. During the laser frequency scan ions are collected and compressed in velocity space which leads to the increase of the fluorescence signal at $t = 2$ s. After stopping the scan, the count rate remains almost constant for several seconds. The constant rate shows that the ion ensemble stays resonant with the lasers. The particles are confined between the co- and the counterpropagating laser forces in velocity space.

Therefore, one observes longitudinal long-term cooling of a fast ion beam by an optical molasses.

Fluorescence measurements over longer times show a slow exponential decrease whose time constant of $\approx 18$ seconds is only slightly shorter than the beam lifetime ($\tau = 20\,\mathrm{s}$). The shorter time constant is caused by the loss of ions out of the capture range of the cooling force profile due to intra beam scattering. Ions scattered out of the capture range in velocity space experience almost no laser forces that could cool them back to the stable point. Therefore, ions are lost for the cooling process. In the bunched cooling scheme, these ions would start oscillating again in the bunch potential while they are cooled back to the stable point. However, the slight reduction of the time constant shows that under the presented conditions, losses through IBS are almost negligible.

One possible reason for this small influence of cooling process on hard Coulomb collisions might be the ion beam was still possibly transversally hot. As shown in chapter 3 a transverse hot beam leads to a large beam diameter resulting in a low ion density. The low density strongly reduces the collision rate and therefore the losses for the cooling process. A transversally cold beam would lead to a higher collision rate. These collision would then result in higher ion losses for the cooling process. However, the losses could be suppresses by the use of a capture range extension such as a rapid adiabatic passage (see section 2.3). This point will be examined in more detail during the next beam time (chapter 5).

**Capturing ions in an optical molasses**

A cooling effect can also be observed using fixed laser frequencies without scanning. This is demonstrated in figure 4.12 showing the fluorescence count rate during this cooling process. The laser system was adjusted with a fixed relative detuning of 160 MHz. The injected ion beam was electron-cooled for ten seconds. The stable point of the electron cooling force in velocity space was adjusted to be several 100 m/s away from the stable point produced by the optical molasses. The capturing process is schematically depicted above the fluorescence plot. The first sketch shows the situation during electron cooling. The electron cooling force draws the ions to its stable point resulting in a Gaussian distribution which is apart from the laser forces. Therefore the ion beam is not resonant with the lasers. One observes almost no fluorescence light. After the electron cooler is switched off, the ion ensemble moves apart due to diffusion and intra beam scattering. The velocity distribution broadens (second sketch). A part of this distribution approaches the molasses force profile and is drawn to its stable point. Ions are continuously captured in the molasses. These ions are now resonant with the lasers. Therefore, the fluorescence count rate increases as well which is shown in the plot. The time axis starts right after switching of the electron cooler. The ion ensemble broaden-

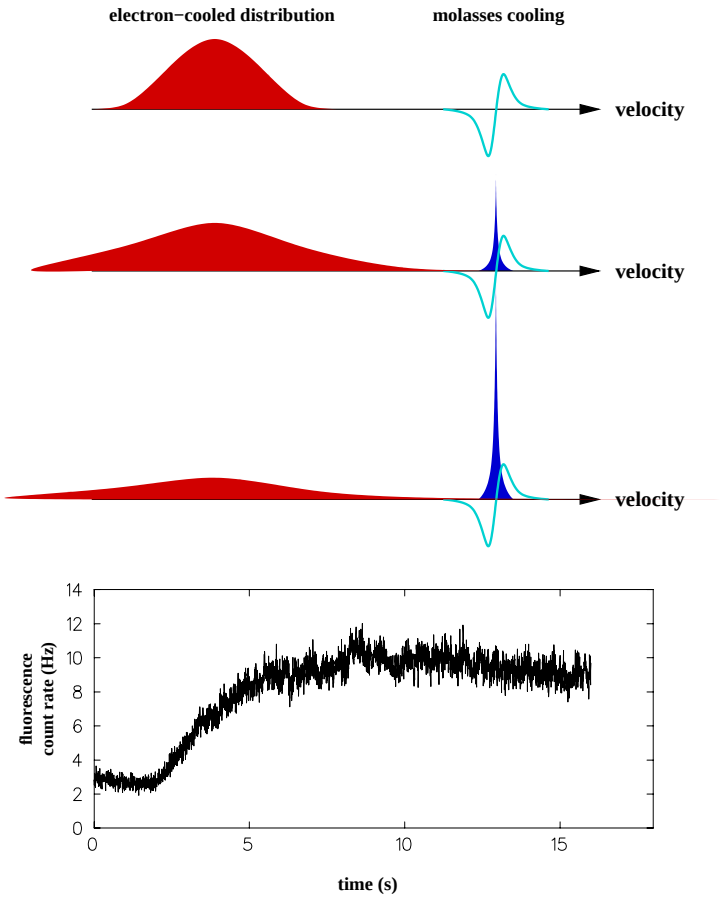


**Figure 4.12:** *Increasing fluorescence signal during the collection of electron-cooled ions into the molasses using fixed laser frequencies. The measurement starts right after switching off the electron cooler. The capturing process in velocity space is sketched for three times above the plot.*

ing in velocity space reaches the optical molasses after approximately one second. The fluorescence rate increases steadily up to $t = 10\,\mathrm{s}$ were it decreases again due to the limited beam lifetime.

Although one observes cooling, this method is not very efficient since only a small fraction of the electron-cooled distribution is captured by the molasses. A frequency scan of the counterpropagating laser however can collect almost all ions of the electron-cooled beam if the broad precooled ensemble is initially in between both far-detuned lasers. On the other hand, this experiment demonstrates the capture of ions in the molasses during the cooling process.

### Longitudinal temperatures

During the presented long-term molasses cooling experiments, the longitudinal velocity distribution was measured using an HV-scan. A typical scan is shown in figure 4.13. The measured profile shows some characteristic differences to

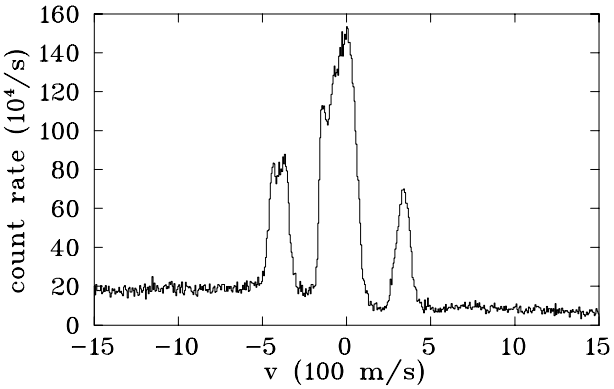


**Figure 4.13:** *Longitudinal velocity distribution during molasses cooling using the HV-scan method.*

the scans taken during bunched laser cooling. One observes a narrow peak with almost no pedestal. The significant suppression of a broad background ensemble reflects the fact that ions undergoing a collision process are not cooled back. This again shows the effect of the small capture range of the optical molasses.

Furthermore in contrast to bunched cooling, the narrow peak is now almost symmetric. The reason for that is the different motion in phase space: Since the cooling force in in optical molasses is symmetric, ions moving with a slight velocity deviation are drawn back to the stable point with the same force independent from the sign of the deviation. This is not the case in the bunched cooling scheme. Ions with a slightly lower velocity experience a strong accelerating force from the copropagating argon ion laser. Ions moving too fast however only experience the much smaller counterforce produced by the bunch potential. This leads to the characteristic sharp edge of the cold peaks as shown in figure 3.4. The remaining slight asymmetry in figure 4.13 might rely on the fact that the co- and the counterpropagating laser beams have different laser intensities. Very first results from the computer simulation that has been modified for molasses cooling validate this interpretation.

The cooling experiments were also done with different relative laser detunings after the frequency scan. For each experiment the velocity distribution was measured three seconds after the laser scan stopped using HV-scans. The longitudinal temperatures as well as the ion numbers of the cold subensemble with respect to the relative detuning is depicted in figure 4.14. With decreasing laser detuning,

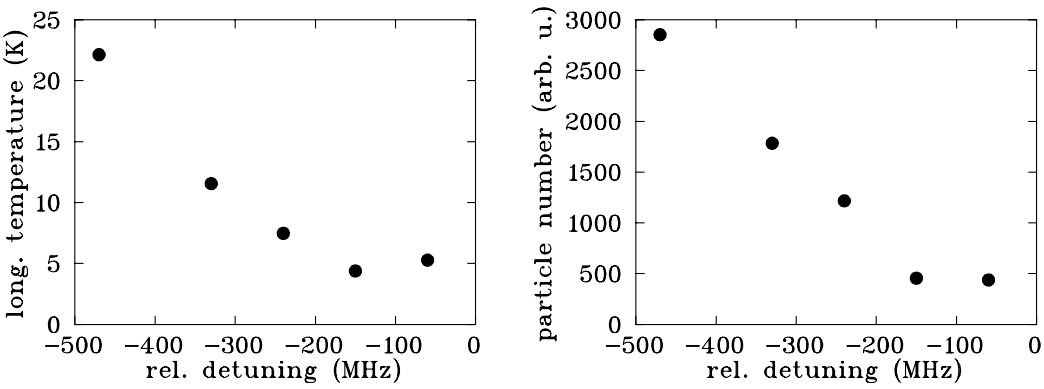


**Figure 4.14:** *Longitudinal temperatures (left) and particle numbers (right) of the cold ion ensemble captured out of the ECOOL distribution with respect to the relative detuning of the cooling lasers measured with the HV-scan method.*

the resulting longitudinal temperature also becomes lower and lower. This is the effect of the increasing slope at the stable point of the laser force profile with decreasing detuning as depicted in figure 4.15. This slope determines the friction

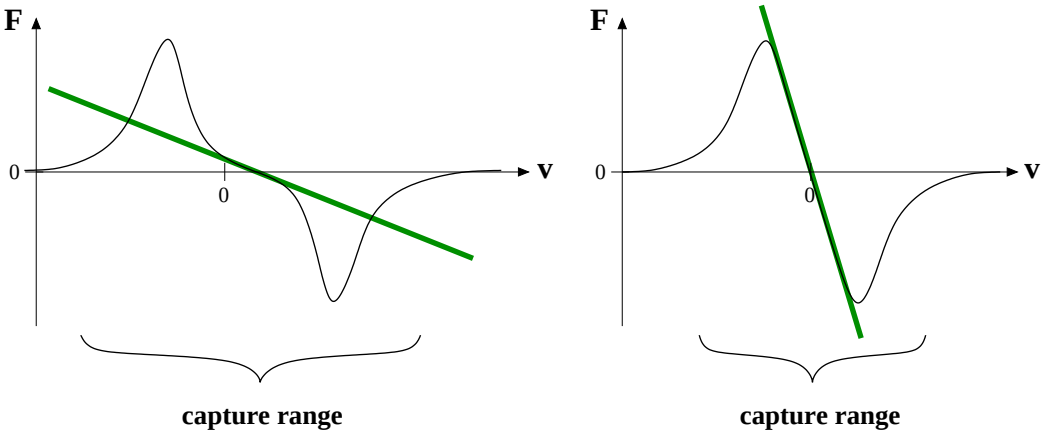


**Figure 4.15:** *Schematic pictures of the cooling force profiles for different relative detunings. The distance of the accelerating and the decelerating laser forces in velocity space strongly influences the friction coefficient represented by the slopes at the stable point.*

coefficient and therefore the cooling rate (section 2.2.3).

Theoretically, the temperature limit of laser molasses cooling is the so-called *Doppler limit* [Metcalf and van der Straten, 1999]: As shown in section 2.3 the momentum transfer averaged over many spontaneous emission processes of an excited ion vanishes ($\langle \vec{p} \rangle = 0$). The square of the momentum however does not

disappear ($\langle \vec{p}^2 \rangle = 0$). A laser-cooled ion performs a random walk which corresponds to a heating process. The diffusion constant of this motion thereby determines the heating rate. The resulting temperature is determined by the ratio of the cooling and the heating rate which leads to the expression for the Doppler temperature $\langle E_{\mathrm{kin}} \rangle_{\mathrm{Doppl}} = k_{\mathrm{B}} T_{\mathrm{Doppl}} = \hbar\Gamma/2$ ($\Gamma$: natural line width of the atomic transition). In our case, the Doppler limit for Beryllium ions is $325\,\mu$K. This small value indicates, that the cooling method is in our case not limited by photon scattering and thus the laser cooling process itself. The main reason for the much higher temperatures of some Kelvin is the existence of the very strong heating process due to intra beam scattering.

The right picture shows the number of particles being in the narrow peak of the velocity distribution. With smaller detunings the number of ions also decreases. The reason for that is the capture range of the cooling force. The capture range for molasses cooling is given by the velocity interval defined by both laser force profiles (roughly depicted as braces in figure 4.15. Ions being outside this interval are not cooled and are part of the broad background ensemble. The velocity interval and thus the capture is proportional to the relative detuning of the lasers. For a narrow capture range, even ions that have undergone a collision with a small velocity change are pushed outside the molasses. Hence, the number of ions in the cooled peak decreases with smaller-getting detuning.

Both experimental results demonstrate the significant role of intra beam scattering for cooling of fast stored ion beams. On the one hand the heating process induced by IBS is the main limiting factor for the beam temperatures that can be experimentally achieved. In connection to the capture range of the cooling force, intra beam scattering also significantly influences the number of ions in the cold peak.

The time evolution of the molasses cooling process was examined by taking a series of HV-scans at different times after the laser frequency scan. The corresponding temperatures of the cold subensemble are shown in figure 4.16. From the beam lifetime one can calculate the total number of ions stored in the ring at the time of the particular measurement. Since the number of ions right after injection as well as the fraction of particles being in the cold ensemble is currently not known, the particle number is given in arbitrary units.

One observes a decrease of the longitudinal temperatures with preceding cooling time. This behavior can on the one hand be explained by the time needed for relaxation of the longitudinal ion ensemble experiencing the laser force. Right after the frequency scan it takes some time to draw the ion ensemble to the stable point. On the other hand, the decreasing beam current leads to a reduction of intra beam scattering and thus a decreasing heating rate. Furthermore, as described above, ions scattered far away from the capture range are lost for the cooling process and no longer notably contribute to the cooling dynamics. Hence, this

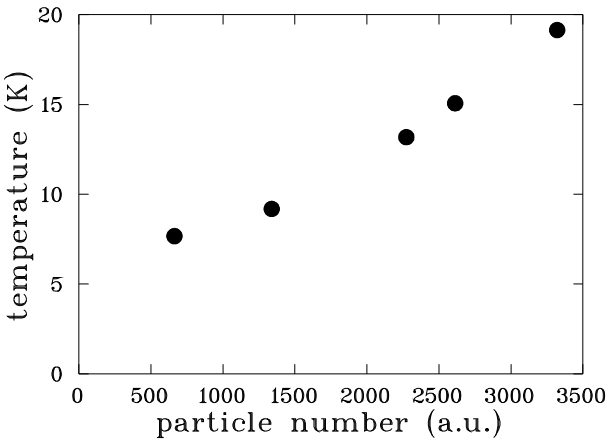


**Figure 4.16:** *Longitudinal beam temperatures during molasses cooling at a fixed relative laser detuning with respect to the particle number.*

measurement directly demonstrates the influence of intra beam scattering on the laser cooling process.

### Schottky noise analysis

As described in section 2.4.3 for coasting beams it is possible to measure the distribution of the ion revolution frequencies by Schottky noise analysis. This method allows a non-destructive measurement of the longitudinal velocity distribution. In addition, this method has the advantage that that distribution is not hidden behind the three-peak structure as in HV-scans. Figure 4.17 shows longitudinal velocity distributions using Schottky noise analysis for different laser detunings. The first plot (left) is measured for a large detuning of 600 MHz. One ends up with a rather broad velocity distribution. In this case it is not possible to fit an expected Gaussian distribution to the data. A smaller detuning (middle plot) of 110 MHz however shows an almost Gaussian peak with a sigma width of 45 m/s. The third picture shows a laser detuning very close to zero. One observes a significant loss of ions whose total number corresponds to the area under the peak of the Schottky spectrum. Most of the ion ensemble is already pushed away by the laser force. The velocity spread of the remaining ions of 28 m/s is somewhat smaller compared to the middle plot. The measured longitudinal temperatures fit very well to the values determined by HV-scan measurements.

With this method, it is also possible to monitor the longitudinal cooling dynamics during the frequency scan and therefore the process of collecting and compressing the ion ensemble. For this purpose, we performed a very slow laser frequency scan over 15 seconds covering a frequency range of 2 GHz. The fre-

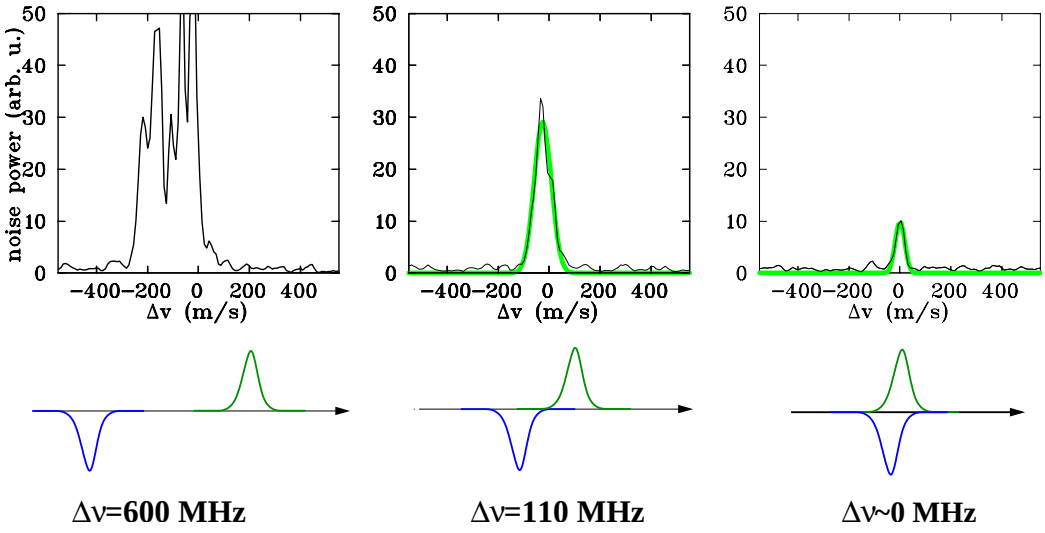


**Figure 4.17:** *Longitudinal temperatures with respect to the relative detuning of the copropagating laser measured by Schottky noise analysis. The thick lines in the middle and the right plot are fit curves assuming a Gaussian distribution.*

quency scan was started five seconds after finishing a ten second electron cooling phase. Schottky pictures were taken every second during the laser scan. Since the maximum data acquisition rate was one Schottky analysis in three seconds, several injection cycles have been used with shifted measurement times: The first injection was performed taking Schottky pictures after $t = 0\,\mathrm{s}$, $t = 3\,\mathrm{s}$, $t = 6\,\mathrm{s}$ etc. For the second injection the measurement times were $t = 1\,\mathrm{s}$, $t = 4\,\mathrm{s}$, $t = 7\,\mathrm{s}$ etc. and for third one $t = 2\,\mathrm{s}$, $t = 5\,\mathrm{s}$, $t = 8\,\mathrm{s}$ etc. Therefore, with three injections the longitudinal velocity distribution could be observed with a time resolution of one second. A series of selected Schottky pictures is shown in figure 4.18. The first plot was recorded during the electron cooling phase. One observes a comparably broad velocity distribution which corresponds to the equilibrium temperature of an electron-cooled ion beam. The next plot shows ions that are pushed by the argon ion laser outside its resonance range towards higher velocities. At this point, the force profile of the counterpropagating laser is outside the drawing area. The frequency scan starts right after the third picture. In the following for pictures, one observes the compression of the velocity distribution. One clearly sees the continuous shift of the right border of the distribution towards the velocity position of the copropagating argon ion laser. The signal height steadily increases since more and more ions are concentrated on a narrowing velocity interval. In the last two pictures, the relative detuning becomes positive, so that there is no longer a stable point in velocity space. This corresponds to the sharp drop of in the fluorescence signal in figure 4.9. The Schottky plots show an abrupt disappearance of almost

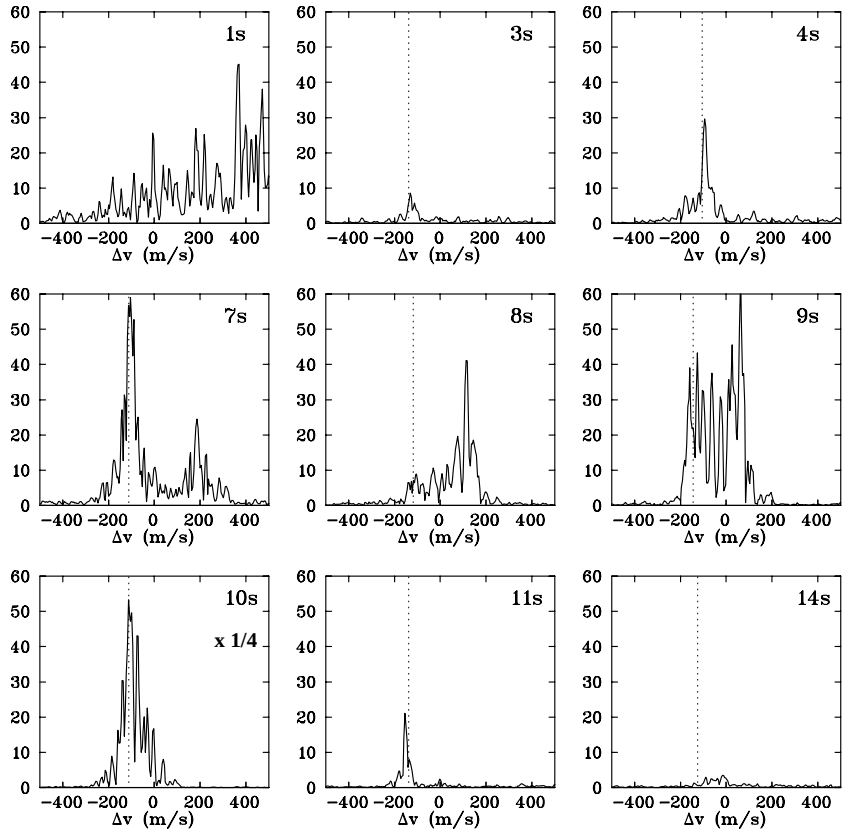


**Figure 4.18:** *Longitudinal dynamics during a slow dye ramp monitored by Schottky analysis. The dashed line denotes the position of the argon ion laser.*

the complete ion ensemble. There are only a couple of ions left being pushed away by the argon ion laser as it was the case right after electron cooling (second picture).

The shape of the Schottky signals during laser cooling has also been discussed in [Hangst et al., 1995a, Lebedev et al., 1995]. It turned out that additional effects such as Landau damping and the occurrence of plasma waves along the closed orbit influence the measurement. These effects can also be observed in our measurements as a two peak structure emerging e.g at $t = 7\,\mathrm{s}$. These observations have to be further investigated. Nevertheless, the presented method allows the realtime observation of the longitudinal velocity distribution during the scanning and cooling process. This tool will also become of particular interest for the observation of Coulomb ordering.

### 4.2.3 Transverse cooling

The transverse dynamics during coasting beam cooling is monitored with the beam profile monitor (BPM) as for the case of bunched beams. During the entire measurement cycle, a set of beam profiles was recorded by accumulating the signal counts for three seconds per profile. Therefore, the total measurement time of of 39 seconds delivers a set of 13 beam profile pictures, which shows the time development of the transverse phase-space. In addition, the measurement was averaged over three injections to improve signal/noise ratio due to the low ion beam current. The resulting profiles were fit according a Gaussian distribution function. The sigma widths determined from the fit are used to calculate the horizontal and vertical beam emittances of the ring-averaged temperatures respectively using the known values of the beta function at the position of the BPM as described in section 2.2. Furthermore, the data has been corrected considering the finite resolution temperature of the BPM (section 2.4.3).

The ion beam was electron-cooled for ten seconds right after injection. The counterpropagating laser beam was adjusted in maximum overlap position with respect to the beam. The optimum overlap was determined with an uncertainty of $\approx 150\,\mu$m by maximizing the fluorescence signals while scanning the laser over the electron-cooled velocity distribution. The beam waist of this system sitting in the center of the cooling section of the storage ring was $w_{326} \approx 1.5\,$mm. The overlap position of the copropagating argon ion laser with a beam waist of $w_{300} \approx 2.5\,$mm was also optimized by maximizing the fluorescence rate during repeated HV-scans.

Right after electron cooling, the frequency-doubled laser system was scanned over 2.5 GHz in 1.5 seconds to collect the ions in velocity space as already demonstrated in section 4.2.2. The scan stopped at a relative detuning of 200 MHz. The storage ring was oparated in betatron coupling mode (section 2.3.2) to ensure a coupling of both transverse degrees of freedom. In this case, the dispersive coupling, normally only present between the longitudinal and the horizontal beam direction, leads to a heating or cooling of the complete transverse phase-space. Dispersive heating and cooling of a coasting beam is demonstrated by separate measurements at different horizontal positions of the copropagating argon ion laser inwards and outwards with respect to the ion beam. The counterpropagating laser system was kept in the optimum overlap position with the ion beam. The measured time development of transverse phase-space at four different copropagating laser positions is shown in figure 4.19.

The very left column schematically depicts the horizontal positions of the copropagating (300 nm) and the counterpropagating (326 nm) laser beams with respect to the ions. The middle and the right columns show the horizontal and vertical ring-averaged beam temperatures with respect to the time after injection.

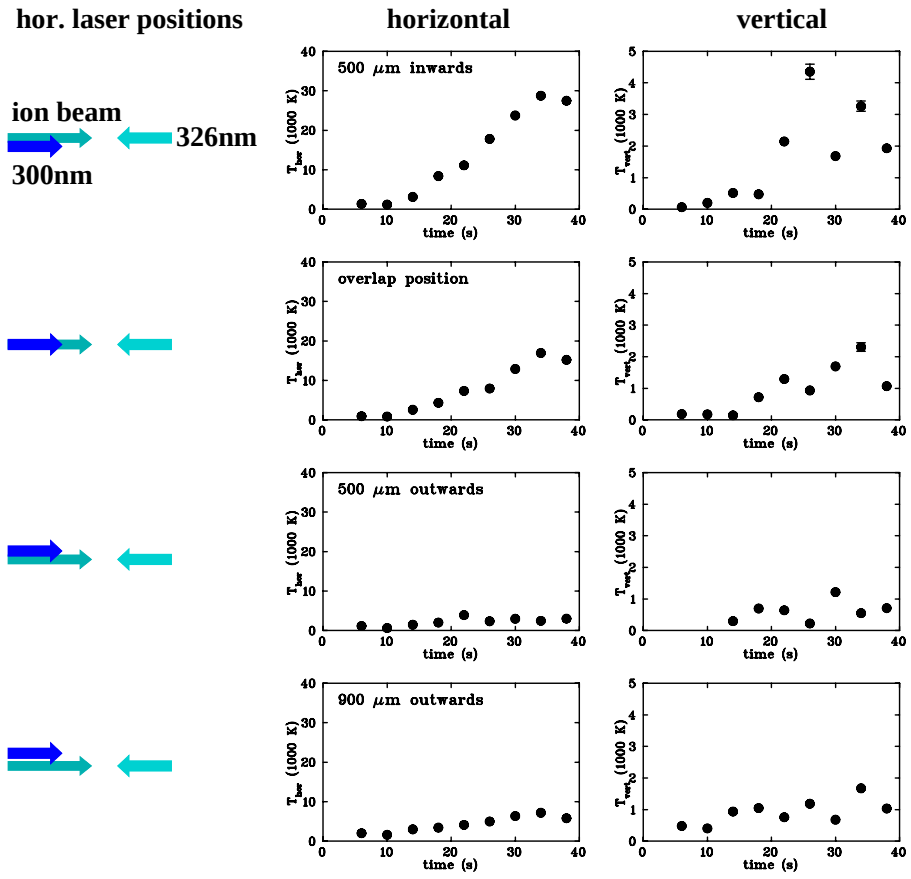


**Figure 4.19:** *Development of the transverse temperatures for different horizontal laser positions. One observes either dispersive heating (first row) or cooling (third row).*

The first two data points in each plot correspond to the equilibrium temperature of the electron-cooled beam. The very first data point at $t = 3\,\mathrm{s}$ has been excluded in all the plots because at this time the extremely hot ion beam right after injection is not yet cooled down leading to temperatures higher than 20,000 Kelvin.

In the first row, the argon ion laser was displaced 0.5 mm inwards corresponding to 1/4 of its beam waist. After switching off electron cooling ($t = 10\,\mathrm{s}$) one clearly observes a steady heat-up of the horizontal temperature. This measurement impressively shows the effect of dispersive heating. Due to a partly damaged multi-channel plate of the vertical BPM the count rates are reduced by a factor of two with respect to the horizontal direction. This leads to a comparably larger scattering of the data point. Nevertheless one also observes an increase of the vertical temperature which clearly shows the effect of betatron coupling. Without this coupling the heat-up would have only been measured in the horizontal

degree of freedom. The observed dispersive heating also overcomes the indirect cooling through intra beam scattering: Without dispersive cooling, the ion beam would be transversally cooled due to a heat exchange with the very efficiently cooled longitudinal degree of freedom (see section 2.3.2). The measured heat-up is therefore an unambigous signature of the dispersive coupling. The dispersive heating increases the beam diameter and lowers the collision rate. Therefore indirect cooling is reduced which leads to a further heat-up of the beam.

For the next measurement (second row in figure 4.19). the argon ion laser is placed in the optimum overlap position with the ion beam. The laser should now neither dispersively heat nor cool the beam. This horizontal position represents an unstable equilibrium. Even slight horizontal shifts from this overlap position would lead to dispersive cooling or heating. The beam profile measurements still indicate an increase of the transverse temperature during molasses cooling. However, the heating rate is noticeably smaller then in the first experiment. Obviously the overlap position as determined as described above is still slightly shifted ring inwards corresponding to weak dispersive heating.

In the third case the copropagating laser was shifted 0.5 mm ring outwards, a symmetrical horizontal shift in the opposite direction with respect to the first experiment. After the electron cooling phase, the beam does not blow up but the transverse temperatures remain almost constant. In this case, one clearly observes dispersive cooling. The cooling of both degrees of freedom again demonstrates the effect of betatron coupling. Both transverse cooling mechanisms, dispersive cooling and indirect cooling through collisions works in the same direction. Dispersive cooling reduces the beam diameter resulting in a higher collision rate. This increases the transversal/longitudinal IBS coupling which leads to a stronger indirect cooling as well. This experiment represents the first 3D laser cooling of a fast coasting ion beam.

A further laser beam displacement of 0.9 mm outwards from the overlap position is shown in the last row of figure 4.19. The displacement roughly corresponds to one sigma width of the laser beam. The plot again shows a slight increase of the emittances although the beam is still dispersively cooled. This behavior can be explained with a significantly reduced longitudinal cooling rate due to the rather worse overlap with the ion beam. This worse longitudinal cooling also reduces the indirect transverse cooling leading to somewhat higher temperatures.

The presented experiment clearly shows that the dispersive cooling mechanism also works very well for the coasting beam cooling scheme. The achieved transverse temperatures of about $T_\perp \simeq 250\,\mathrm{K}$ for the case of dispersive cooling are comparable to the values measured with the bunched cooling technique. During data analysis the relative detuning of $\approx 200$ MHz turned out not to be the optimum value for longitudinal cooling (see figure 4.14). Therefore, higher cooling rate for the longitudinal and thus the transverse degrees of freedom are surely achievable.

A further improvement of transverse cooling would possibly be the horizontal displacement of the counterpropagating laser beam to also achieve dispersive cooling with this laser system. In this case, one has to consider that the sign of the horizontal displacement (inwards or outwards) in order to attain cooling or heating are reversed with respect to the argon ion laser. Since the counterpropagating laser decelerates the ions, the betatron oscillation is damped if the laser is displaced inwards with respect to the ion beam (compare this with figure 2.11) and vice versa. However, the small beam waist only allows rather tiny displacements of less than 300 $\mu$m since larger displacements would strongly reduce the longitudinal cooling rate.

## 4.3 Conclusion

The presented experiments demonstrate first cooling of a coasting Beryllium beam by a one-dimensional optical molasses. Up to now the phase-space densities are comparable to the densities achieved with the bunched cooling method. In addition we presented first true 3D cooling of a coasting beam employing the dispersive coupling. While the longtudinal cooling parameters were the optimum values, transverse cooling will be further optimized in the next beam time. Furthermore the computer model modified for coasting beam cooling will give more insight into the dynamics of coasting beam cooling.

All coasting beam cooling experiments have been carried out with total ion numbers of $10^7$. According the molecular dynamics simulations Coulomb ordering is expected for particle numbers lower than $10^6$. Therefore ordering effects are not expected. However, next beam time we will reduce the particle number and try to reproduce the observation of a sudden dissappearance of intra beam scattering.

# Chapter 5

# Outlook

The goal of all presented laser cooling experiments is still to answer the question whether it is possible to achieve a beam crystallization and to find out the ultimate limits of the phase-space density. The sudden disappearance of Coulomb collisions during laser cooling of bunched beams (section 3.3) already shows the signature of an ordering process. However due to the ambiguity of the results require further experiments to get a clear proof of a crystallization. In order to improve the cooling rates and to investigate that the observations are not connected to the bunched cooling scheme itself, a new series of coasting beam cooling experiments have been carried out (chapter 4). These experiments have been done with ion numbers of about $10^7$ in order to examine the new cooling dynamics with signal rates easy to handle. The transition in bunched beams however took place at $10^6$ ions in agreement with the theoretical predictions for the formation of a linear chain. The next step to reproduce the anomalous behavior in a coasting beam would therefore be cooling of much more dilute beams with ion numbers below $10^6$.

In particular for coasting beam cooling du to the limited capture range of the cooling force and the fact that scattered ions cannot be cooled back, the use of a capture range extension could be very interesting. As shown in figure 2.9 a rapid adiabatic passage can extend the force profile to a velocity range to about 1000 m/s. This is sufficient to completely suppress any losses for the cooling process due to IBS. Unfortunately a rapid adiabatic passage realized by a set of drift tubes in the cooling section of the storage ring (section 2.3.1) would modify the force profiles of the co- and the counterpropagating laser in the same manner as schematically depicted in figure 5.1a. Both profiles would be extended in the same direction in velocity space. One possible solution to this problem could be a further relative laser detuning of roughly 2 GHz (figure 5.1b). In this case the stable point would be produced by the main peak of one laser and the “wing” of the capture range extension of the other laser. This experiment will be done next

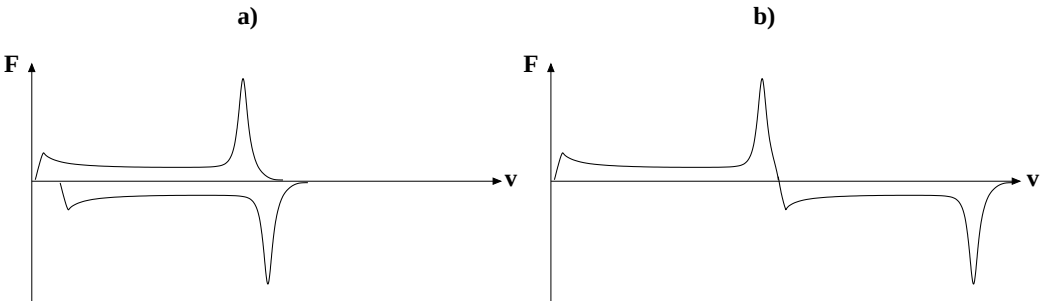


**Figure 5.1:** *The capture range extension through rapid adiabatic passage leads to an extension of both co- and counterpropagating molasses lasers towards the same direction in velocity space (a). A solution could be a further relative laser detuning (b).*

beam time.

Another possible extension of the experiment would possibly be sympathetic cooling of $^{18}O^{2+}$ by the laser-cooled Beryllium beam. Besides tiny isotopic shifts, the oxygen beam has the same magnetic rigidity as $^{9}Be^{+}$. It could therefore in principle be stored simultaneously with the Beryllium beam in the ring at the same velocity. While the Beryllium beam is efficiently laser cooled, collisions between both ion species lead to a heat exchange, so that the oxygen beam could be cooled as well. This is similar to the situation of electron cooling where a cold electron beam is merged with an ion beam. This experiment would give some important insight on the cooling process through collisions which is also interesting for the further understanding of electron cooling.

A completely different regime would be laser cooling of very dense beams with particle numbers of more than $10^9$. In the near future, the production of these dense beams will be possible with the recently installed high current injector (HCI). The investigation of laser cooling in a strong IBS regime could lead to a furthergoing understanding of the influence of collisions to the cooling process. Furthermore high current beams of extreme phase-space densities represent a unique tool to observe effects such as tune-shifts, self bunching and storage ring instabilities.

# Appendix A

# Electron cooling force measurements using barrier buckets

## A.1 Introduction

Over the years, electron cooling has become a standard cooling technique used in storage rings[Poth, 1990]. In contrast to other techniques such as laser cooling [Petrich et al., 1993], electron cooling is a universal method with no limitation to a certain ion species. However, it is surprising that only a few systematic measurements exist which quantitatively determine the influence of various cooler parameters (electron density, guiding fields, expansion factors etc.) on the cooling process. In particular, one is interested in the cooling rates that can be achieved, since this determines the cooling times and equilibrium temperatures of the ion beams. The major reason for this situation is the lack of simple methods to measure the cooling force profile. Up to now, there are only two known techniques to measure the force profile: One can perform a controlled heat-up of the ions by applying a white-noise source of defined power to the ion beam [Winkler et al., 1997, Beutelspacher, 2000]. The velocity dependency of the cooling force can then be calculated by solving a Fokker-Planck equation with the measured thermodynamic ion distribution and the applied heating power as input values. On the other hand, the cooling force can be measured by applying a counter force to the ions using an induction accelerator [Ellert et al., 1992]. The measurement of the revolution frequency of the electron-cooled ions in force equilibrium with respect to the strength of the counter force directly delivers the force profile. While the heating method allows the measurement of the force profile over a large velocity range including the non-linear part of it, the accuracy of this technique strongly depends on the underlying model being used. The second method measures the cooling force directly but requires an induction accelerator

as a dedicated device only present in a few storage rings.

We present a novel method to measure the linear part of the longitudinal force profile of an electron cooler using radio frequency beam bunching. The confining bunch potential generates a counter force acting against the electron cooler. Since this method has only very small experimental requirements it can be easily applied to all existing storage rings without the need of major technical modifications. This way it should be possible to perform systematic cooling force measurements which allow a further insight into the physics of electron cooling in storage rings.

## A.2 Description of the method

For electron cooling, a cold electron beam is merged with the hot ion beam over a distance of typically some meters. Coulomb collisions allow a transfer of thermal energy between ion and electron beam. Hence, thermal equilibration leads to a temperature reduction of the ion beam [Poth, 1990]. The cooling process can be described in terms of a velocity-dependent cooling force shown in Fig. A.1. At

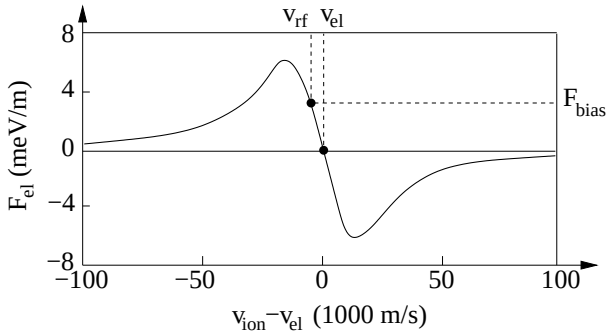


**Figure A.1:** *Longitudinal electron cooling force profile in velocity space. The plot shows the typical values for $Be^+$ ions at $v/c$=4%. A mismatch between the stable velocity $v_{\mathrm{el}}$ of the ECOOL and the velocity of a confining bunching potential $v_{\mathrm{rf}}$ leads to an additional force $F_{\mathrm{bias}}$ acting on the ions.*

the velocity $v_{\mathrm{el}}$ of the electron beam the cooling force vanishes forming the stable point in velocity space where the ions are drawn to. Within a broad velocity range of typically $10^4$ m/s around the stable point the cooling force is proportional to the ion velocity. Outside the linear regime, the cooling force goes down to zero due to the decreasing cross-section of electron-ion collisions with growing relative velocities. The cooling force near the stable point can be written as $F(v) = -\alpha v$ with the friction coefficient $\alpha$. In this case, the cooling rate, which determines the time needed to reach temperature equilibrium, is written as $\Lambda = 2\alpha/m$ ($m$: ion

mass). The beam bunching method can be used to measure this linear part of the force profile and therefore the cooling rate.

The measurement of the velocity dependency can be done by applying a well-known velocity-independent probe force acting on the ion beam which counteracts the cooling force to be measured. Then, one has to determine the velocity of the ions being in force equilibrium with the cooling force and the probe force. This way, by changing the probe force, the force profile of the cooler in velocity space can be measured.

One way to produce a constant force for a limited time is the use of an induction accelerator [Ellert et al., 1992]. The induction accelerator applies a force on the coasting ion beam exploiting the transformer principle. A current ramp in a coil enclosing the beam pipe induces a voltage in the ion beam representing the second coil. This way, a longitudinal force can be applied for a limited time. For a measurement of the electron cooling force one uses different current ramps and measures the corresponding change of velocity by monitoring the ion revolution frequency via Schottky analysis.

Beam bunching offers a way to generate a counter force without any time limitations. In this case, a pseudo potential confines the ions in the longitudinal direction. The potential shape can be adjusted to generate a counter force. For radio frequency beam bunching, the ion beam passes a radio frequency field tuned at a harmonic of the revolution frequency. While passing through, the ions are accelerated or decelerated depending on their particular phase with respect to the electrical field. The ions are therefore confined in the longitudinal degree of freedom.

The confinement can be described in terms of a pseudo potential ("bucket") moving with the ions. The velocity of this bucket is determined by the bunching frequency $\nu_{\mathrm{rf}}$: $v_{\mathrm{rf}} = L\nu_{\mathrm{rf}}/h$ with the ring circumference $L$ and the harmonic number $h$. In the comoving frame, the ions perform an oscillatory motion (synchrotron oscillation) in this potential. A detailed description of beam bunching with non-sinusoidal potential shapes can be found in [Eisenbarth et al., 2000a]. The presented experiments measuring the cooling force make use of a special potential shape called *barrier buckets* sketched in Fig. A.2. This potential consists of a square-well potential with a bottom of constant slope. The ions oscillating in the bucket are reflected at the steep potential walls resulting in a well-defined bunch length which is independent from the relative kinetic energy of the ions. Inside the bucket, ions experience a constant force due to the potential slope. The spatial time-averaged distribution of the thermal ion ensemble in the longitudinal degree of freedom is given by Boltzmann's distribution:

$$n(s) = n_0 e^{-(V_{\mathrm{rf}}(s))/(k_{\mathrm{B}}T)} \quad ,$$

$s$: longitudinal position, $T$: longitudinal ion temperature, $V_{\mathrm{rf}}$: pseudo potential,

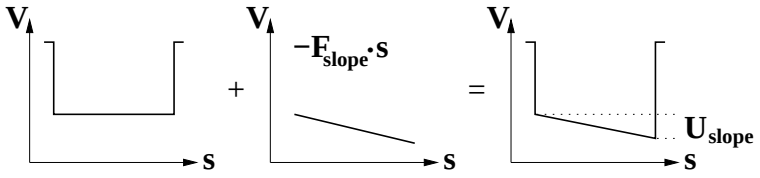


**Figure A.2:** *The barrier-bucket potential used for beam bunching consists of a square-well potential with a bottom of constant slope. The slope defines the strength of the probe force* $F_{\mathrm{slope}}$.

$k_{\mathrm{B}}$: Boltzmann's constant.

A constant potential bottom (pure square-well potential) leads to a constant density distribution. The shape of the distribution is independent of the beam temperature. A potential slope pushes the ions either towards the rear or front wall dependent on the sign of the slope. In this case, the ion ensemble is exponentially distributed along the longitudinal axis within the bucket. In addition, the distribution is strongly dependent on the beam temperature. For measuring the cooling force, the derivative of this potential slope provides the force counteracting the electron cooler.

For a bunched electron-cooled beam two velocities are defined: On the one hand the velocity of the electron beam $v_{\mathrm{el}}$ and on the other hand the ion velocity determined by the bunch frequency $v_{\mathrm{rf}}$. If $v_{\mathrm{rf}}$ is not equal to $v_{\mathrm{el}}$ ions still experience a velocity-dependent cooling force. However, the cooling force now has an offset described by $F_{\mathrm{bias}} = \alpha(v_{\mathrm{el}} - v_{\mathrm{rf}})$ (see Fig. A.1). Hence, ions experience an accelerating or decelerating force inside the bunch respectively. The calculated motion of one particle in a pure square-well potential in longitudinal phase-space for both mismatched cases $v_{\mathrm{rf}} < v_{\mathrm{el}}$, $v_{\mathrm{rf}} > v_{\mathrm{el}}$ and in case of perfect match $v_{\mathrm{rf}} = v_{\mathrm{el}}$ is shown in Fig. A.3 (left column). One observes a damped an-harmonic oscillation which is drawn to one side of the bunch potential in both mismatched cases. In the matched case the ion movement ends somewhere in the potential depending on the starting point of the simulation.

In a barrier-bunched beam, the offset $F_{\mathrm{bias}}$ can be exactly compensated by adjusting the potential slope counteracting the offset. In this case, ions oscillating in the bucket do no longer experience any net force inside of it, leading to a constant longitudinal ion density distribution. Since the potential slope of the bucket and therefore the counterforce is precisely known, one can measure the cooling force for a certain ion velocity by adjusting the slope until the ion distribution becomes constant. The ion velocity is then determined by the bunching frequency.

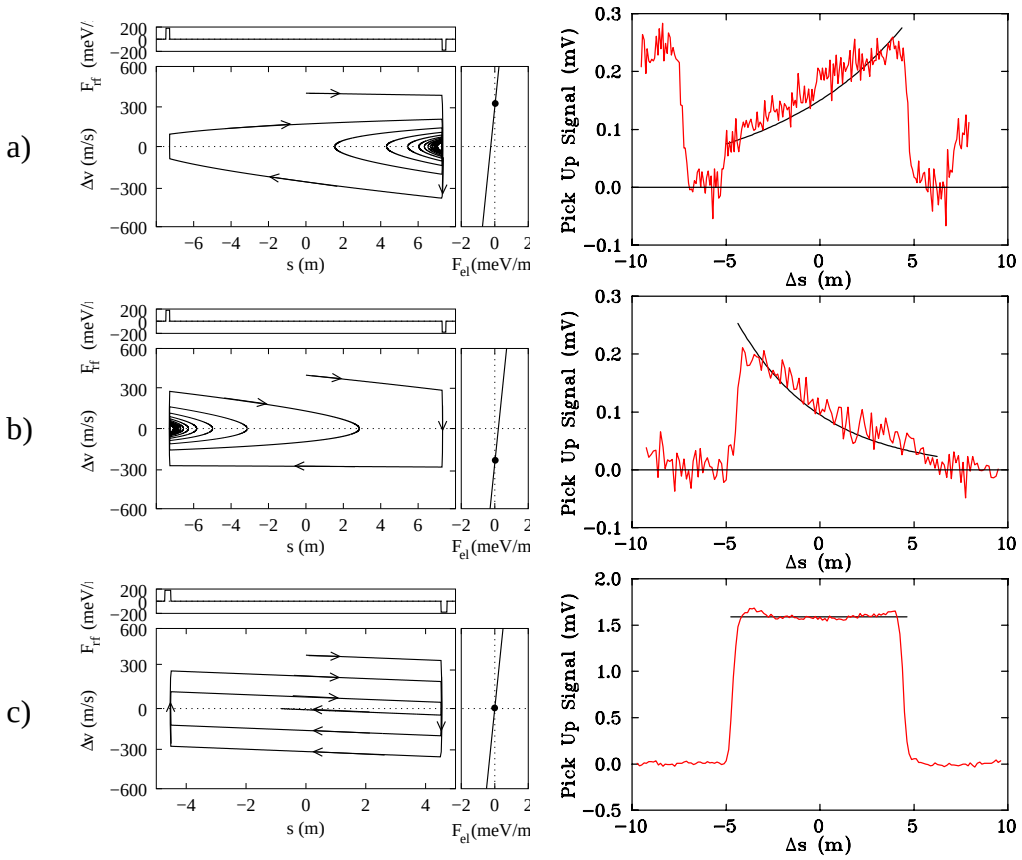


**Figure A.3:** *Calculated phase-space diagrams of an electron-cooled bunched beam for two bunching frequencies: lower (a), higher (b) and equal (c) with respect to the corresponding electron beam velocity. The right column shows the longitudinal ion distribution measured with an electrostatic pickup. The fitted theoretical Boltzmann distributions are shown as solid lines.*

## A.3 Experimental Realization

The experiments are performed at the Heidelberg Test Storage Ring (TSR) with $^{9}Be^{+}$ ions at 7.3 MeV corresponding to 4% of the speed of light. The typical beam current is 3 $\mu$A corresponding to $5 \cdot 10^{6}$ stored ions in total. A rest gas pressure of $3 \cdot 10^{-11}$ mbar leads to a $1/e$ lifetime of 35 s.

The electron cooler superimposes a cold electron beam over a distance of 1.2 m with the ion beam. The electron beam current of typically 12 mA is guided through a toroid field of 400 Gauss resulting in a beam of 3 cm in diameter and a number density of $8.7 \cdot 10^{6}$ cm$^{-3}$. The acceleration voltage of 480 V in combination with an adiabatic expansion (factor 9.8) of the transverse degree of freedom leads to an electron beam temperature of about 2 K. The resulting equilibrium

temperature of the $Be^+$-beam after typically ten seconds cooling time is about 300 K.

Beam bunching is performed using a pair of non-resonant horizontal kicker plates set on the same potential. The radio frequency was produced with an arbitrary function generator (Hewlett Packard 33120A). This device gives us a great flexibility in modeling our potential shapes. A 10 W broadband rf amplifier feeds the signal to the metal plates terminated by 50 Ohm dummy loads. An important point is the precise knowledge of the bunching potential as seen by the ion beam. Since two kicker plates with the same potential are used, bunching forces act on the ions only while entering or leaving the plates. The effective bunch potential is therefore calculated as:

$$V_{\mathrm{rf}} = \frac{l_{\mathrm{eff}} e h}{\gamma^2 \eta L} U$$

($V_{\mathrm{rf}}$: potential amplitude seen by the ions, $l_{\mathrm{eff}}$: effective length of the kicker plates, $h$: harmonic number, $\gamma$: relativistic factor, $\eta$: machine-specific slip factor [Hofmann and Kalisch, 1996] ($\eta_{\mathrm{TSR}}$=0.895), $L$:ring circumference, $U$:voltage amplitude applied to the kicker plates)

The effective length of the kicker plates takes stray fields into account. The actual shape of the bunching device does not play any role for the measurement since this length can be exactly determined by measuring the ion oscillation frequency in a harmonic bunching potential (*synchrotron frequency* $\nu_{\mathrm{snyc}}$) via Schottky analysis. For this purpose, a sinusoidal waveform is applied to the kicker plates. The oscillating ions produce motional sidebands apart from the carrier frequency in the Schottky spectrum. The difference of sideband and carrier frequency directly corresponds to the ion oscillation frequency. This frequency depends on the strength of the bunching potential seen by the ions. For a given bunching amplitude applied to the kicker plates, the effective length $l_{\mathrm{eff}}$ is calculated as

$$l_{\mathrm{eff}} = \frac{2\pi m \gamma^2 L^3}{h^2 e U} \nu_{\mathrm{sync}}^2 \quad .$$

With the slope of the barrier bucket, the counter force acting against the electron cooler is calculated as

$$F_{\mathrm{rf}} = \frac{l_{\mathrm{eff}} e h^2}{\gamma^2 \eta L^2} \cdot \frac{U_{\mathrm{slope}}}{d} \quad ,$$

where $U_{\mathrm{slope}}$ is the voltage slope of the bucket (see Fig. A.2) and $d$ the on-off ratio (duty cycle) of the square-well potential.

The longitudinal ion distribution inside a bunch is observed with an electrostatic pickup device [Albrecht, 1993]. The changing current of the bunched ion beam induces mirror charge fluctuations on a metal ring enclosing the beam. These charge fluctuations can be measured over a large resistor as a voltage signal.

The amplified signal is displayed with an oscilloscope giving us a realtime picture of the longitudinal ion distribution.

## A.4 Force measurement

We first measured the synchrotron frequency with our setup to determine the effective length of our kicker plates. A sinusoidal rf voltage with an amplitude of 30 Volts at the 15th harmonic gave a synchrotron frequency of 200 Hz. Hence, the effective length of our kicker plates is 60 cm. For the force measurement with barrier buckets we used a bunching frequency of 676 kHz corresponding to the third harmonic of the revolution frequency. The duty cycle was 50% ($d$=0.5). The rf amplitude of 30 $V_{pp}$ allows a maximum ion velocity spread that can be hold in the bucket (bucket acceptance) of 1500 m/s.

For the ECOOL force measurement, the injected ion beam is cooled until equilibrium temperature is reached. Then, the barrier bucket potential with a given slope $U_{\mathrm{slope}}$ is switched on. The resulting ion distribution inside the bunch is monitored online with the pickup device. The bunching frequency is adjusted until the ions are evenly distributed. Even a slight frequency mismatch is clearly visible in the pickup signal as an ion distribution pushed to one side of the bucket walls (see Fig. A.3,right) since the interplay of electron cooler and bunching potential forms an unstable equilibrium. If the bunching frequency $\nu_{\mathrm{rf}}$ for the balanced distribution is found,the ion velocity is calculated as $v_{\mathrm{ion}} = \nu_{\mathrm{rf}} L/h$. At this point in velocity space the cooling force is exactly equal to the counter force being calculated from $U_{\mathrm{slope}}$ as described above. The force profile is measured by applying different potential slopes and adjusting the bunch frequency until one attains a homogeneous ion distribution. The measured data points are depicted in fig. A.4 (filled circles). The plot shows the linear part of the cooling force profile around the stable point of the electron cooler.

A change of the bunching frequency by one Hertz corresponds to velocity change of 1.8 m/s. A frequency mismatch of 10 Hz (18 m/s) is clearly observable as an ion ensemble pushed to one of the potential walls. This value also defines the uncertainty of the velocity measurement which is negligibly small. The uncertainty of the applied counter force mainly depends on the uncertainty of the effective kicker length. From the measurement we estimate the accuracy to $\Delta F/F$=15%. The slope of the linear part determines the cooling rate of the electron cooler. For our case this rate amounts to $\Lambda_{\mathrm{rf}} = 16 \pm 2\, s^{-1}$. This stands in perfect agreement to the results using the induction accelerator method (Fig. A.4, open circles) performed right after. In addition, the results agrees very well with previous measurements [Pastuszka et al., 1996].

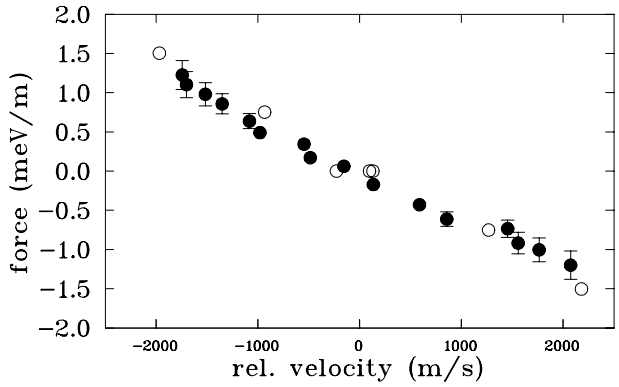


**Figure A.4:** *Measurement of the ECOOL force profiles in velocity space employing barrier buckets (filled circles) and the induction accelerator method (open circles).*

## A.5 Conclusion

We presented a new versatile method to measure the longitudinal force profile of an electron cooler using beam bunching. The results are in very good agreement with the measurements using the induction accelerator. The method is extremely simple to apply and can be done in very short time. In addition, this method is not limited to a specific ion species. It becomes even more effective for higher charged ions because the pickup signal in order to determine the equilibrium point of the longitudinal ion distribution is much stronger. In contrast to the use of an induction accelerator, the requirements for our measurements are comparably small. One only needs a pair of metal plates or a drift tube for beam bunching present in all storage rings. For monitoring the longitudinal distribution one needs an electrostatic pickup which can also be a simple drift tube since we do not need any position information. Our presented method should be directly applicable to all present heavy ion storage rings in order to perform systematic measurements of the cooling process with respect to changes of the various parameters of an electron cooler.

# Appendix B

# Measurement system

The various diagnostic tools presented in chapter 2 are located at different positions along the storage ring. For data acquisition we set up a decentralized architecture as depicted in figure B.1. Each diagnostic device has its own computer system that records the signals and performs a little data pre-analysis. All measurement systems are connected to a ethernet network based on the TCP/IP protocol. The measured data is transmitted over this network. In addition, the network is used to control all the measurement systems from a Linux-PC (denoted as User PC in the picture).

The pickup device is read out by a digitizing scope (Model Hewlett Packard 54510A) which also averages the tiny voltages over several scans. The data is readout by a Linux PC using a GPIB (IEEE 488) interface. The readout can be performed locally by a programm or is transmitted via network to the User PC, which also controls the acquisition parameters such as the number of averages, the time resolution etc.

For the readout of the photomultipliers and the control of the high voltage tubes one uses a CAMAC system which is controlled by a computer based on a VME-bus architecture. This computer works with a realtime Unix derivate called LynxOS. The photomultiplier pulses are amplified, shaped and converted to logical signals using conventional NIM devices. These logic pulses are fed to a multiscaler CAMAC module. This module contains an internal histogram memory where the photomultiplier pulses are summed up. The multiscaler module also allows the measurement of a time series by counting the pulses into a channel of the histogram memory for a given time and than stepping to the next channel. The module produces synchroneously a control voltage reflecting the current channel number. A time series measurement is therefore be connected to a voltage ramp which can be amplified with an high voltage amplifier and applied to the drift tubes of the storage ring. This way the HV-scan is realized. After a HV-scan or fluorescence scan is finished the whole time series is readout from the histogram

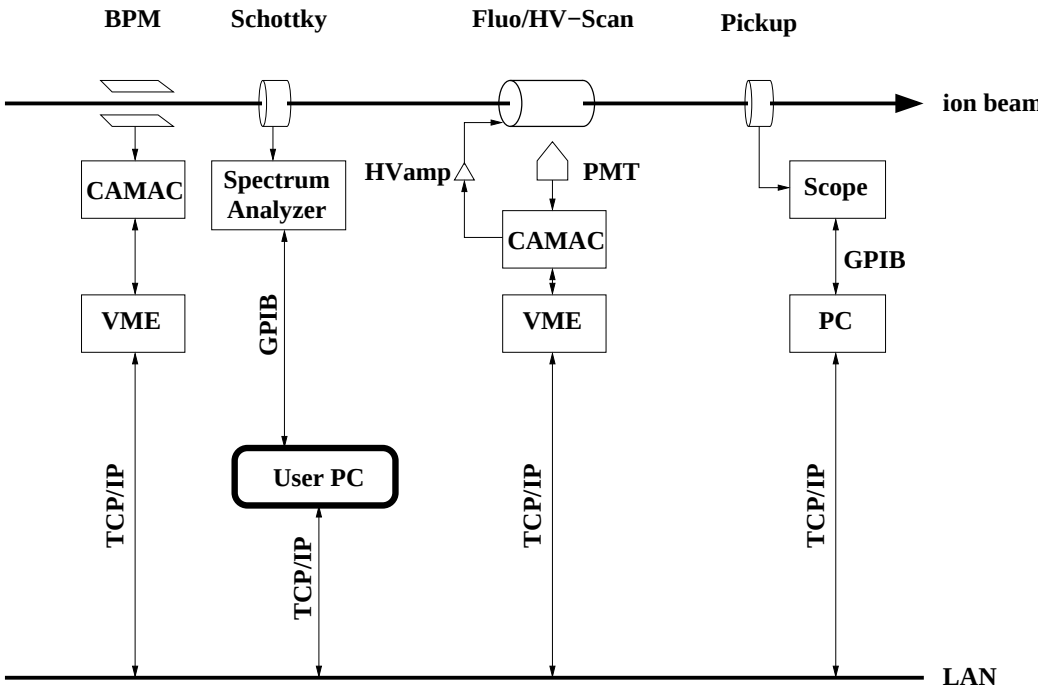


**Figure B.1:** *The data acquisition system for each measuring instrument consists of separate computers connected via a network.*

memory by the VME computer which further transmits the data to the network.

For Schottky analysis, the noise signal taken from an electrostatic pickup was fed into a spectrum analyzer (Hewlett Packard). The fast Fourier transform is internally performed using dedicated digital signal processors (DSPs). Under our conditions, this system produces up to 10 frequency spectra per second. This allows a realtime observation of the longitudinal cooling dynamics. However, the readout via GPIB to the PC (which is also the control PC in the setup) significantly limits the acquisition rate to one Schottky picture in three seconds. The multi-channel plates of the beam profile monitor are also readout by a VME computer which transmits the data to the network.

The used setup ensures the realtime capabilities of the particular diagnostic tools being read out by separate data acquisition subsystems. The decentralized structure also makes this system relatively robust against hardware failures. In addition, further measurement devices can be added without much effort.

# Bibliography

[Albrecht, 1993] Albrecht, F. (1993). Entwicklung eines Strahllagemeßsystems für den Heidelberger Testspeicherring TSR. Diplomarbeit Universität Heidelberg und Max-Planck-Institut für Kernphysik.

[Atutov et al., 1998] Atutov, S., Calabrese, R., Grimm, R., Guidi, V., Lauer, I., Lenisa, P., Luger, V., Mariotti, E., Moi, L., Peters, A., Schramm, U., and Stößel, M. (1998). "White-light" Laser cooling of a Fast Stored Ion Beams. *Phys. Rev. Lett.* **80**, 2129.

[Becker, 1992] Becker, C. (1992). Frequenzstabilisierung von Argon-Ionen-Lasern im Langzeitbereich für die Laserkühlung von $^{9}Be^{+}$-Ionen. Diplomarbeit Universität Heidelberg und Max-Planck-Institut für Kernphysik.

[Beutelspacher, 2000] Beutelspacher, M. (2000). *Systematische Untersuchungen zur ELektronenkühlung am Heidelberge Schwerionenspeicherring TSR*. Dissertation Universität Heidelberg und Max-Planck-Institut für Kernphysik, MPI H-V18-2000.

[Bisoffi et al., 1990] Bisoffi, G., Grieser, M., Jaeschke, E., Krämer, D., and Noda, A. (1990). Radiofrequency Stacking Experiments at the Heidelberg Test Storage Ring. *Nucl. Instr. Meth. A* **287**.

[Blum, 1989] Blum, M. (1989). *Entwicklung einer neuartigen Synchrotron-Beschleunigerkavität für den TSR*. Dissertation Universität Heidelberg und Max-Planck-Institut für Kernphysik.

[Bock, 1997] Bock, R. (1997). Ion Beam Inertial Fusion. In: Jungmann, K., Kowalski, J., Reinhard, I., and Träger, F. (Eds.), *Atomic Physics Methods in Modern Research* , pp. 211–229. Springer-Verlag.

[Bollen et al., 1996] Bollen, G. et al. (1996). ISOLTRAP: a tandem Penning trap system for accurate on-line mass determination of short-lived isotopes. *Nucl. Instr. Meth. A* **368**, 675.

[Boussard, 1995] Boussard, D. (1995). Schottky noise and beam transfer function diagnostics. In: Turner, S. (Ed.), *Cern Accelerator School, Fifth Advanced Accelerator Physics Course* Vol. 2 of *CERN 95-06* , pp. 794–782.

[Boyd and Kleinmann, 1968] Boyd, G. and Kleinmann, D. (1968). Parametric Interaction of focused Gaussian light beams. *J. Appl. Phys.* **39**, 3597.

[Brandau et al., 1999] Brandau, C., Bartsch, T., Böhme, C., Bosch, F., Dunn, G., Franzke, B., Hoffknecht, A., Knopp, H., Kozhuharov, C., Krämer, A., Mokler, P., Müller, A., Nolden, F., Schippers, S., Stachura, Z., Steck, M., Stöhlker, T., Winkler, T., and Wolf, A. (1999). Recombination Measurements of the Heaviest Ions. *Physica Scripta* **T80**, 318.

[Bryant, 1994] Bryant, P. (1994). Simple theory for weak betatron coupling. In: Turner, S. (Ed.), *Proc. CERN Accelerator School, University of Jyväskylä, 1992* Vol. 1 , p. 207. Genf.

[Courant and Snyder, 1958] Courant, E. and Snyder, H. (1958). Theory of the Alternating Gradient Synchrotron. *Annals of Physics* **3**.

[Eike, 1999] Eike, B. (1999). Aufbau eine magnetooptischen Falle zur transversalen Strahldiagnose am Heidelberger Testspeicherring TSR. Diplomarbeit Universität Heidelberg und Max-Planck-Institut für Kernphysik.

[Eike et al., 2000] Eike, B., Luger, V., Manek-Hönninger, I., Grimm, R., and Schwalm, D. (2000). Laser-trapped atoms as a precision target for the storage ring TSR. *Nucl. Instr. and Meth. A* **441**, 81.

[Eisenbarth, 1998] Eisenbarth, U. (1998). Kühlung hochenergetischer Ionenstrahlen am TSR: neue Bunchformen und Raumladungseffekte. Diplomarbeit Universität Heidelberg und Max-Planck-Institut für Kernphysik.

[Eisenbarth et al., 2000a] Eisenbarth, U., Eike, B., Grieser, M., Grimm, R., Lauer, I., Lenisa, P., Luger, V., Mudrich, M., Schätz, T., Schramm, U., Schwalm, D., and Weidemüller, M. (2000a). Laser cooling of fast stored ions in barrier buckets. *Nucl. Instr. and Meth. A* **441**, 209.

[Eisenbarth et al., 2000b] Eisenbarth, U., Mudrich, M., Eike, B., Grieser, M., Grimm, R., Luger, V., Schätz, T., Schramm, U., Schwalm, D., and Weidemüller, M. (2000b). Anomalous behaviour of laser-cooled fast ion beams. *Hyp. Int.* **127**, 223.

[Ellert et al., 1992] Ellert, C. et al. (1992). An Induction Accelerator for the Heidelberg Test Storage Ring TSR. *Nucl. Instr. Meth. A* **314**, 399.

[Ellison et al., 1993] Ellison, T. J. P., Nagaitsev, S. S., Ball, M. S., Caussyn, D. D., Ellison, M. J., and Hamilton, B. J. (1993). Attainment of Space-Charge Dominated Beams in a Synchrotron. *Phys. Rev. Lett.* **70**, 790.

[Ertmer et al., 1985] Ertmer, W., Blatt, R., Hall, J., and Zhu, M. (1985). Laser manipulation of atomic beam velocities:Demonstration of stopped atoms and velocity reversal. *Phys. Rev. Lett.* **54**, 996.

[Fowler and Guggenheim, 1956] Fowler, R. and Guggenheim, E. (1956). *Statistical Thermodynamics*. Cambridge Univ. Press. London and New York.

[Franken et al., 1961] Franken, P., Hill, A., Peters, C., and G., W. (1961). Generation of Optical Harmonics. *Phys. Rev. Lett.* **7**, 118.

[Friedmann, 2001] Friedmann, P. (2001). Frequenzverdoppeltes Lasersystem bei 326 nm für die Laserkühlung hochenergetischer Ionenstrahlen. Diplomarbeit Universität Heidelberg und Max-Planck-Institut für Kernphysik.

[Grieser et al., 1994] Grieser, R., Klein, R., Huber, G., Dickopf, S., Klaft, I., Knobloch, P., Merz, P., Albrecht, F., Grieser, M., Habs, D., Schwalm, D., and Kühl, T. (1994). A test of special relativity with stored lithium ions. *Appl. Phys. B* **59**, 127.

[Grimm et al., 1998] Grimm, R., Eisenbarth, U., Grieser, M., Lenisa, P., Lauer, I., Luger, V., Schätz, T., Schramm, U., Schwalm, D., and Weidemüller, M. (1998). Transverse Laser Cooling of fast ion beams at the Storage Ring TSR. In: Chen, P. (Ed.), *Proceedings of the workshop on quantum aspects of beam physics*. Monterey.

[Gruber, 1993] Gruber, A. (1993). Verbesserung des Laserfrequenz-Stabilisierungssystems zur Kühlung von $^{9}Be^{+}$-Ionen am TSR. Diplomarbeit Universität Heidelberg und Max-Planck-Institut für Kernphysik.

[Habs and Grimm, 1995] Habs, D. and Grimm, R. (1995). Crystalline Ion Beams. *Annu. Rev. Nucl. Part. Sci.* **45**, 391.

[Hangst et al., 1991] Hangst, J., Kristensen, M., Nielsen, J., Poulsen, O., Schiffer, J., and Shi, P. (1991). Laser Cooling of a fast Stored Ion Beam to 1 mK. *Phys. Rev. Lett.* **67**, 1238.

[Hangst et al., 1995a] Hangst, J., Labrador, A., Lebedev, V., Madsen, N., Nielsen, J., Poulsen, O., and Shi, P. (1995a). Anomalous Schottky Signals from a Laser-Cooled Ion Beam. *Phys. Rev. Lett.* **74**, 86.

[Hangst et al., 1995b] Hangst, J., Nielsen, J., Poulsen, O., Shi, P., and Schiffer, J. (1995b). Laser Cooling of a Bunched Beam in a Synchrotron Storage Ring. *Phys. Rev. Lett.* **74**, 4432.

[Hänsch and Couillaud, 1980] Hänsch, T. and Couillaud, B. (1980). Laser Frequency Stabilisation by Polarization Spectroscopy of a Reflecting Reference Cavity. *Opt. Comm.* **35**.

[Hasse, 1999] Hasse, R. (1999). Theoretical Verification of Coulomb Order of Ions in a Storage Ring. *Phys. Rev. Lett.* **83**, 3430.

[Hasse and Schiffer, 1990] Hasse, R. and Schiffer, J. (1990). The Structure of the Cylindrically Confined Coulomb Lattice. *Annals of Physics* **203**, 419.

[Hochadel, 1994a] Hochadel, B. (1994a). Residual-gas ionization beam profile monitor for the Heidelberg test storage ring TSR. *Nucl. Inst. and Meth. A* **343**, 401.

[Hochadel, 1994b] Hochadel, B. (1994b). *Untersuchungen zum Intrabeam Scattering am TSR*. Dissertation Universität Heidelberg und Max-Planck-Institut für Kernphysik.

[Hofmann and Kalisch, 1996] Hofmann, I. and Kalisch, G. (1996). Space-charge-dominated bunched beams in the frequency domain. *Phys. Rev. E* **53**, 2807.

[Horvath, 1994] Horvath, C. (1994). Aufbau eines durchstimmbaren optischen Verdopplungsresonators für Laserkühlexperimente am $^9Be^+$-Ionenstrahl im Heidelberger Speicherring TSR. Diplomarbeit Universität Heidelberg und Max-Planck-Insitut für Kernphysik.

[Kjærgaard et al., 2000] Kjærgaard, N., Aggerholm, S., Bowe, P., Hornekær, L., Madsen, N., Nielsen, J., Schiffer, J., Siegfried, L., and Hangst, J. (2000). Recent results from laser cooling experiments in ASTRID-real-time imaging of ion beams. *Nucl. Instr. Meth. A* **441**, 196.

[Kogelnik, 1966] Kogelnik, L. anf Li, T. (1966). Laser Beams and Resonators. *Appl. Opt.* **5**.

[Lange, 1994] Lange, W. (1994). *Einführung in die Laserphysik*. Wissenschaftliche Buchgesellschaft. Darmstadt.

[Lauer, 1999] Lauer, I. (1999). *Transversale Dynamik lasergekühlter $^9Be^+$-Ionenstrahlen im Speicherring TSR*. Dissertation Max-Planck-Institut für Kernphysik, MPI H-V15-1999.

[Lauer et al., 1998] Lauer, I., Eisenbarth, U., Grieser, M., Grimm, R., Lenisa, P., Luger, V., Schätz, T., Schramm, U., Schwalm, D., and Weidemüller, M. (1998). Transverse laser cooling of a fast stored ion beam through dispersive coupling. *Phys. Rev. Lett.* **81**, 2052.

[Lebedev et al., 1995] Lebedev, V., Hangst, J., and Nielsen, J. (1995). Schottky noise in a laser-cooled ion beam. *Phys. Rev. E* **52**, 4345.

[Luger, 1996] Luger, V. (1996). Untersuchungen zur Struktur gekühlter Bunche. Diplomarbeit Universität Heidelberg und Max-Planck-Institut für Kernphysik, MPI H-V15-1996.

[Luger, 1999] Luger, V. (1999). *Ein Speicherringtarget für hochpräzise Strahlprofil-Diagnose auf Basis einer Magneto-optischen Atomfalle*. Dissertation Universität Heidelberg und Max-Planck-Institut für Kernphysik.

[Madert, 1995] Madert, M. (1995). Laserkühlen gebunchter Ionenstrahlen. Diplomarbeit Universität Heidelberg und Max-Planck-Institut für Kernphysik, MPI H-V9-1995.

[Madsen et al., 1999] Madsen, N., Bowe, P., Drewsen, M., Hornekær, L., Kijærgaard, N., Labrador, A., Nielsen, J., Schiffer, J., Shi, P., and Hangst, J. (1999). Density Limitations in a Stored Laser-cooled Ion Beam. *Phys. Rev. Lett.* **83**, 4301.

[Metcalf and van der Straten, 1994] Metcalf, H. and van der Straten, P. (1994). Cooling and Trapping of Neutral Atoms. *Physics Reports* **244**, 205.

[Metcalf and van der Straten, 1999] Metcalf, H. and van der Straten, P. (1999). *Laser Cooling and Trapping*. Springer-Verlag. New York, Berlin, Heidelberg.

[Miesner, 1995] Miesner, H.-J. (1995). *Laserkühlung dichter Ionenstrahlen*. Dissertation Max-Planck-Institut für Kernphysik, MPI H-V23-1995.

[Miesner et al., 1996a] Miesner, H.-J., Grimm, R., et al. (1996a). Transverse laser cooling of a radio-frequency bunched ion beam in the storage ring TSR. *Nucl. Instr. Meth. A* **383**, 634.

[Miesner et al., 1996b] Miesner, H.-J., Grimm, R., Habs, D., Schwalm, D., Wanner, B., and Wolf, A. (1996b). Efficient, Indirect Transverse Laser Cooling of a fast Stored Ion Beam. *Phys. Rev. Lett.* **77**, 623.

[Møller, 1994] Møller, S. (1994). Cooling Techniques. In: Turner, S. (Ed.), *Cern Accelerator School CERN 94-01* Vol. 2 , p. 601. University of Jyväskylä, Finnland.

[Mudrich, 1999] Mudrich, M. (1999). Langzeitdynamik lasergekühlter Ionenstrahlen am Speicherring TSR. Diplomarbeit Universität Heidelberg und Max-Planck-Insitut für Kernphysik.

[Nagaitsev et al., 1994] Nagaitsev, S. S., Ellison, T. J., Ellison, M. J., and Anderson, D. (1994). The investigation of space charge dominated cooled bunched beams in a synchrotron. In: Bosser, J. (Ed.), *Proc. Workshop on Beam Cooling and Related Topics, Montreux* , pp. 405–410. Report CERN 94-03. Genf.

[Pastuszka et al., 1996] Pastuszka, S., Schramm, U., Grieser, M., Broude, C., Grimm, R., Habs, D., Kenntner, J., Miesner, H.-J., Schüßler, T., Schwalm, D., and Wolf, A. (1996). Electron cooling and recombination experiments with an adiabatically expanded electron beam. *Nucl. Inst. Meth. A* **396**, 11.

[Petrich et al., 1993] Petrich, W. et al. (1993). Laser cooling of stored high-velocity ions by means of the spontaneous force. *Phys. Rev. A* **48**.

[Poth, 1990] Poth, H. (1990). Electron cooling: theory, experiment, application. *Phys. Rep.* **196**.

[Press et al., 1992] Press, W. H., Teukolsky, S. A., Vetterling, W. T., and Flannery, B. P. (1992). *Numerical Recipes in C, The Art of Scientific Computing*. Cambridge University Press. 2 edition.

[Radon et al., 1997] Radon, T., Kerscher, T., Schlitt, B., Beckert, K., Beha, T., Bosch, F., Eickhoff, H., Franzke, B., Fujita, Y., Geissel, H., Hausmann, M., Irnich, H., Jung, H. C., Klepper, O., Kluge, H.-J., Kozhuharov, C., Kraus, G., Löbner, K. E. G., Münzenberg, G., Novikov, Y., Nickel, F., Nolden, F., Patyk, Z., Reich, H., Scheidenberger, C., Schwab, W., Steck, M., Sümmerer, K., and Wollnik, H. (1997). Schottky Mass Measurements of Cooled Proton-Rich Nuclei at the GSI Experimental Storage Ring. *Phys. Rev. Lett.* **78**, 4701.

[Risken, 1989] Risken, H. (1989). *The Fokker-Planck Equation*. Springer-Verlag. Berlin, Heidelberg, New York, London, Paris, Tokyo 2. edition.

[Schätz et al., 2001] Schätz, T., Schramm, U., and Habs, D. (2001). Crystalline ion beams. *Nature* **412**, 717.

[Schröder et al., 1990] Schröder, S., Klein, R., Boos, N., Gerhard, M., Grieser, R., Huber, G., Karafillidis, A., Krieg, M., Schmidt, N., Kühl, T., Neumann, R., Balykin, V., Grieser, M., Habs, D., Jaeschke, E., Krämer, D., Kristensen, M., Music, M., Petrich, W., Schwalm, D., Sigray, P., Steck, M., Wanner, B., and Wolf, A. (1990). First Laser Cooling of Relativistic Ions in a Storage Ring. *Phys. Rev. Lett.* **64**, 2901.

[Schünemann et al., 1999] Schünemann, U., Engler, H., Grimm, R., Weidemüller, M., and Zielonkow ski, M. (1999). Simple scheme for tunable frequency offset locking of two lasers. *Rev. Sci. Inst.* **70**, 242.

[Sørensen, 1987] Sørensen, A. H. (1987). Introduction to Intrabeam Scattering. In: Turner, S. (Ed.), *CERN Accelerator School*. Report CERN 87-10.

[Steck et al., 1996] Steck, M., Beckert, K., Eickhoff, H., Franzke, B., Nolden, F., Reich, H., Schlitt, B., and Winkler, T. (1996). Anomalous Temperature Reduction of Electron-cooled Heavy Ion Beams in the Storage Ring ESR. *Phys. Rev. Lett.* **77**, 3803.

[Stoessel, 1997] Stoessel, M. (1997). Logitudinale Diagnose gekühlter $^{9}Be^{+}$-Ionenstrahlen mit einem frequenzverdoppelten Lasersystem. Diplomarbeit Universität Heidelberg und Max-Planck-Institut für Kernhpysik, MPI H-V15-1996.

[Walther, 1993] Walther, H. (1993). Phase transitions of stored laser-cooled ions. In: *Advances in atomic, molecular, and optical physics* Vol. 42 , pp. 137–182. Academic Press.

[Wanner et al., 1998] Wanner, B., Grimm, R., Gruber, A., Habs, D., Miesner, H.-J., Nielsen, J. S., and Schwalm, D. (1998). Rapid adiabatic passage in laser cooling of fast stored ion beams. *Phys. Rev. A* **58**, 2242.

[Wei et al., 1995] Wei, J., Li, X.-P., and Sessler, A. (1995). Crystalline Beam Properties As Predicted For The Storage Rings ASTRID and TSR. In: *Proc. of the Particle Accelerator Conference and International Conference on High-Energy Accelerators, Dallas, Texas* , p. 2946.

[Wernøe, 1993] Wernøe, H. (1993). Laserstrahlpositionierung und -lagestabilisierung am TSR. Diplomarbeit Universität Heidelberg und Max-Planck-Institut für Kernphysik, MPIH-V8-1993.

[Wille, 1996] Wille, K. (1996). *Physik der Teilchenbeschleuniger und Synchrotronstrahlungsquellen*. Teubner Studienbücher. Stuttgart 2. edition.

[Winkler et al., 1997] Winkler, T., Beckert, T., Bosch, F., Eickhoff, H., Franzke, B., Nolden, F., Reich, H., Schlitt, B., and Steck, M. (1997). Electron cooling for highly charged ions in the ESR. *Nucl. Instr. and Meth. A* **391**, 12.

[Wolf et al., 2000] Wolf, A., Gwinner, G., Linkemann, J., Saghiri, A., Schmitt, M., Schwalm, D., Grieser, M., Beutelspacher, M., Bartsch, T., Brandau, C., Hoffknecht, A., Müller, A., Schippers, S., Uwira, O., and Savin, D. (2000). Recombination in electron coolers. *Nucl. Inst. Meth. A* **441**, 183.

# Dankeschön

Nach einigen Wochen des Zusammenschreibens dieser Arbeit ist nun der Zeitpunkt gekommen, alle diejenigen lobend zu erwähnen, die entschiedenen Anteil am Gelingen dieser Arbeit hatten. Natürlich ist das Experimentieren an einer solch großen Anlage wie dem Speicherring nicht alleine zu bewerkstelligen, was im Text oft mit einem einfachen “Wir” zum Ausdruck gebracht wurde. Bekanntermaßen bietet eine Danksagung ein weites Feld für diverse “Fettnäpfchen” in die man treten kann, wenn man eine Person zuwenig, an der falschen Stelle oder durch eine ungeschickte Wortwahl honoriert. Ich gebe daher mein Bestes und hoffe, dass sich niemand auf den Schlips getreten fühlt ;-)

Neben Rudi Grimm, der mich vor seinem Wechsel nach Innsbruck im ersten Jahr betreute, geht mein Dank and Dirk Schwalm und Matthias Weidemüller, die mir diese Arbeit ermöglicht und immer wieder durch wertvolle Diskussionen in die richtigen Bahnen gelenkt haben. Vor allem Matthias hat mehrere Versionen dieser Arbeit gelesen und und durch konstruktive Kritik entscheidend aufgewertet. Ebenso möchte ich mich bei Wolfgang Quint bedanken, der sich bereit erklärt hat, die Zweitbegutachtung zu übernehmen.

Desweiteren gilt mein besonderer Dank Marcel Mudrich, Patrick Friedmann und Sandro Hannemann, die während meiner Zeit als Diplomanden an dem Projekt gearbeitet haben. Viele Ergebnisse, die in meiner Arbeit auftauchen, sind zu einem großen Anteil auch “auf deren Mist gewachsen”.

Die vielen Strahlzeiten wären nicht zu bewältigen gewesen ohne die tatkräftige Unterstützung von Björn Eike (“Yesyesyes”), Jan Kleinert, Guido Saathoff und Sergei Karpuk sowie die Münchner Delegation Tobias Schätz und Uli Schramm. Die vielen Stunden am Speicherring im Kampf gegen die Lasersysteme und anderem technischen Equipment machten uns zu einem eingeschworenen Team. Gleichwohl werde ich den zum Ende einer Strahlzeit hin immer seltsamer werdenden Humor (“Stuhl!!!”) nicht vergessen. Mein ganz spezieller Dank geht auch an Helga Krieger, die sich in aufopferungsvoller Hingabe vor allem stets um ein reibungsloses Funktionieren der Lasersysteme gekümmert hat. Viel zu oft wurde ihre Arbeiten fast als selbstverständlich angenommen. Der Kampf gegen die Tücken des TSR wurde vom “Herr der Ringe” Manfred Grieser sowie Kurt Horn bestrit-

ten. Für die vielen unverzichtbaren elektronischen Schaltungen möchte ich mich vor allem bei Oliver Koschorrek bedanken.

Nicht zu unterschätzen sind die vielen Gespräche und Diskussionen mit anderen aktuellen und ehemaligen Mitgliedern unserer Gruppe: Hans Engler, Markus Hammes, Selim Jochim, Stephan Kraft, Allard Mosk, Henning Moritz, David Rychtarik und Kilian Singer. Sie haben entscheidend zum sehr guten Gruppenklima beigetragen.

Mein Dank geht natürlich nicht zuletzt auch an meine Eltern, die mich immer wieder unterstützten und ermutigten, wenn auch ab und zu “mal ’was schief gegangen ist”.